Universidade Federal de São Carlos

CENTER OF EXACT SCIENCES AND TECHNOLOGY

PROGRAM OF POST-GRADUATION IN PHYSICS

Doctoral Tessis

Optimal Quantum Control Applied to Quantum Dots[1]

Carlos Mario Rivera Ruiz

São Carlos

2019

[1]Study supported by the "Coordenação de Aperfeiçoamento de Pessoal de Nível Superior (CAPES) and by the Universidade Federal de São Carlos" (UFSCAR)

CENTER OF EXACT SCIENCES AND TECHNOLOGY

PROGRAM OF POST-GRADUATION IN PHYSICS

Optimal Quantum Control Applied to Quantum Dots

Carlos Mario Rivera Ruiz

Thesis presented to the physics department
of Federal University of São Carlos -
DF/UFSCar as part of the requirements for
the PhD title in Physics, under the
supervision of:

Prof. Dr. Leonardo Kleber Castelano.

São Carlos

2019

UNIVERSIDADE FEDERAL DE SÃO CARLOS

Centro de Ciências Exatas e de Tecnologia
Programa de Pós-Graduação em Física

Folha de Aprovação

Assinaturas dos membros da comissão examinadora que avaliou e aprovou a Defesa de Tese de Doutorado do candidato Carlos Mario Rivera Ruiz, realizada em 03/10/2019:

Prof. Dr. Leonardo Kleber Castelano
UFSCar

Prof. Dr. Vivaldo Leiria Campo Junior
UFSCar

Prof. Dr. Reginaldo de Jesus Napolitano
USP

Prof. Dr. Emanuel Fernandes de Lima
UFSCar

Prof. Dr. Marcelo Zoega Maialle
UNICAMP

To Alice... in chains.

Acknowledgements

First of all I would like to thank my supervisor Prof. Leonardo Kleber Castelano for guiding me along my research projects with valuable advice, patience and encouragement. Also special thanks to the other professors that contributed with the development of this research Emanuel Lima, Marcelo Maialle, Victor, and Gilmar Eugenio Marques.

Also thanks to all the friends with whom I spent great time and shared wonderful experiences during my stay in São Carlos: Cabral, Murilo, Jean, Ian, Gomes da Costa, Robinson, Carlos e Luciana. Finally, thanks to my family, that always supports me and believes in me.

"The sciences do not try to explain, they hardly even try to interpret, they mainly make models. By a model, is meant a mathematical construct which, with the addition of certain verbal interpretation describes observed phenomena. The justification of such a mathematical construct is solely and precisely that it is expected to work."

John von Neumann

Resumo

Neste trabalho, revisamos a dinâmica de um-qubit e oferecemos uma interpretação unificadora das dinâmicas de Landau-Zener e de Rabi, indicando os elementos físicos responsáveis pela manifestação de um fenômeno ou de outro, sem a necessidade de defini-los como fenômenos separados. Além disso, demonstramos a possibilidade de implementar portas quânticas de alta fidelidade em duas plataformas diferentes de pontos quânticos, com a assistência do método numérico da teoria de controle ótimo quântico "two-point boundary-value quantum control paradigm" (TBQCP) [126]. Na primeira plataforma que consiste de um ponto quântico duplo (DQD) incorporado em um nanofio, otimizamos pulsos elétricos correspondentes a três portas quânticas de um-qubit com fidelidade maior que 0,99. Também comparamos a eficiência da dinâmica com o pulso otimizado obtida através do TBQCP em relação aos outros mecanismos dinâmicos (Rabi e Landau-Zener); e descobrimos que o TBQCP pode fornecer pulsos capazes de executar tarefas em tempos mais curtos. Para a segunda plataforma que consiste de um DQD eletrostático, implementamos o algoritmo de permutação quântica (QPA) [121], o que requer a superposição quântica de estados com fases relativas bem definidas. Devido à necessidade de usar pelo menos um sistema de três níveis nesse algoritmo, usamos qubits híbridos em vez de spin qubits. Para encontrar os campos elétricos AC ideais que implementam as portas quânticas necessárias, aplicamos o método TBQCP. Empregando esse método, fomos capazes de determinar pulsos elétricos ideais que executam as portas quânticas com uma alta fidelidade e em tempos mais rápidos do que os tempos de decoerência e relaxamento. Os nossos resultados demonstram a possibilidade de realizar portas quânticas universais totalmente elétricas em DQDs por meio do controle ótimo quântico.

Palavras chaves: Controle quântico ótimo, Informação quântica, pontos quânticos.

Abstract

In the present study, we review the one-qubit dynamics and we offer a new unifying interpretation of the Landau-Zenner and the Rabi dynamics, by indicating the physical elements responsible for the manifestation of one phenomenon or the other, without the need to define them as separate phenomena. Furthermore, we demonstrate the possibility of electrically implementing quantum gates with high fidelity in two different platforms of quantum dots, with the assistance of the two-point boundary-value quantum control paradigm (TBQCP) [126]. In the first platform consisting of a double quantum dot (DQD) embedded in a nanowire, we optimized single qubit pulses corresponding to three quantum gates assuring a fidelity for every gate higher than 0,99. Also we compare the dynamical efficiency of the optimized pulses via the TBQCP method, respect to the other dynamical mechanisms (Rabi and Landau-Zener); and we found that TBQCP can provide pulses that can perform tasks in shorter times. For the second platform consisting of an electrostatical DQD, we implement the quantum permutation algorithm (QPA) [121], which requires the quantum superposition of states with well-defined relative phases. Because of the necessity of using at least a three level system in this algorithm, we use hybrid qubits instead of spin qubits. In order to find the optimal AC electric fields that implement the required quantum gates, we apply the TBQCP method. By employing such method, we were able to determine optimal electric pulses that perform the quantum gates with high fidelity and in times faster than decoherence and relaxation time. Our results demonstrate the possibility of achieving all-electrical universal quantum gates in DQDs by means of optimal quantum control.

Keywords: Optimal quantum control, Quantum information, Quantum dots.

Contents

Chapter 1

Introduction

The potential of quantum computation was envisaged for the first time by Feynman in 1982 [1], when he recognized that the complexity of a quantum system yields a remarkable difficulty, in order to simulate its temporal evolution via a classical computer. With this challenge in mind, Feynman proposed that an hypothetical quantum computer could simulate the evolution of a quantum system efficiently. A decade later, the Grover [2] and Shor [3] algorithms, showed that quantum algorithms can outperform the efficiency of classical algorithms in various tasks. Quantum protocols employ resources like the entanglement or the quantum superposition, (phenomena with no equivalents in classical physics), e.g. the quantum cryptography protocol BB84 in [4]. In order to harness the advantages of these new resources, new areas emerged like quantum information and quantum computation. Currently, the BB84 protocol constitutes the first commercial application in quantum information, and there are other few commercial applications in quantum information [5]. The first experimental implementations of a quantum algorithm (in the year of 1998, for the algorithm of Deutsch-Jozsa and in 2001 for the algorithm of Shor) were made in the platform of Nuclear Magnetic Resonance (NMR) [6, 7], materializing the quantum information processing in a physical system corresponding to a quantum computer with two qubits.

Despite the fact that currently, the interest to materialize this practical applications of quantum phenomena is higher than ever, there is a disparity between most of the theoretical advances of quantum information and computation and their experimental realizations. This situation represents a technological void that needs to be filled, given that only some basic protocols or algorithms have been implemented. At the moment, the power of the existing quantum devices to process information falls short compared to those that do not exploit quantum phenomena.

Most of the disparity between the progress in theory and experiments comes from technical difficulties involved in the development of quantum devices. For this reason, the scientific community as well as the technological industries are in an active exploration for

the best physical systems that could materialize the theoretical quantum information applications into experimental devices. A significant incentive rise from the higher efficiency in the computation time provided by quantum algorithms, compared to the classical ones, when we try to perform the same task. With the purpose to reduce this void between theory and experiment, different platforms are being explored. Let us review briefly some of the most relevant.

1.1 Physical platforms for the qubit

The first quantum systems to be studied and manipulated were physical systems offering two possible states, which offer **natural qubits**. These platforms were proposed mainly from the fields of atomic physics and quantum optics [8, 9], with natural qubits like the electronic or the nuclear spin e.g. Rydberg atoms [10], trapped ions in ultra-cold atoms [17], the nitrogen-vacancy centers [11], where the first controlled-NOT (CNOT) quantum gate was experimentally implemented in 1995 [12], or the nuclear magnetic resonance (NMR), where the Shor algorithm was experimentally realized for the first time [7]. Also the polarization degrees of freedom in light (e.g. quantum electrodynamic cavities [13]), or an interplay of both (light and spins) in atomic ensembles [14]. Given that light and atoms are being studied since the very foundations of quantum mechanics, there was a vast knowledge acquiered for these systems, and it was precisely these platforms that became the first testbeds for developing quantum control methods and experimental applications of quantum information processing.

A common feature of these platforms is the fact that they are relatively more isolated from the surrounding environment than other platforms and therefore have better protection from decoherence. For example, atomic hyperfine ground states or metastable states serve as quantum memories to store quantum information because of their long decoherence time. But such isolation is also the origin of a serious deficiency, since it limits the coupling and thus its interaction with other systems, difficulting its scalability.

On the other hand there are platforms that offer **artificial qubits**, like the superconducting circuits [15], the phosphorus donors in silicon [16, 23], or the different platforms used to host quantum dots. These platforms offer faster mechanisms for their manipulation, offering higher speeds for information processing compared to the natural qubit platforms. Also they have the promising possibility of miniaturization and large-scale integration by applying the knowledge in techniques and production acquired in the semiconductor industry. A shortcoming from this platforms is that they are usually more susceptible to decoherence, but fortunately the information processing is not required to be perfect [18], (not even the current classical computation is), and some strategies can compensate the trade off between speed processing and errors, with the schemes of error detection and correction [20], or the fault-tolerant computation, for which a threshold

value in the error below 3% is acceptable [21].

Currently there are a lot of proposals of physical platforms for a quantum processor, with different strengths and limitations; which are actively used for experimental implementations. A possible way to consider the most feasibles in the short and long term, was thought in the year 2000, by DiVincenzo, who stated the characteristics required in a physical system to be a candidate for a real quantum information platform [18].

DiVincenzo criteria for quantum processors

1. A scalable physical system with well-characterized qubits.
2. The ability to initialize the qubits to a reference state such as $|00...0\rangle$.
3. Long relevant decoherence times that are much longer than gate operation times.
4. A "universal" set of quantum gates.
5. The ability to measure specific qubits.
6. Interconversion between stationary and "flying" qubits.
7. Faithful transmission of flying qubits.

From these requirements, the first five are related with the information processing, while the last two refers to the reliable transmission of such information. The first, the scalability is a particularly important requirement which means that a linear increase in the capacity of processing must not imply a corresponding exponential increase in the physical resources. Such requisite curbs the practical limit in the capacity that a quantum processor based in a determined platform can achieve. Most of the proposed platforms for quantum information processing satisfies the other conditions related to the information processing (conditions 2 to 5), and have advantages and limitations respect to each other. But in the long term, the first requirement determines the practical viability of a platform in the future, as implementations will require the processing of higher volumes of information, these platforms will also require a greater number of coupled qubits to perform efficiently the required tasks, and at the end the most efficient platform will dominate the production of such devices, as occurred in the past with the technologies of vacuum tubes and the transistor in the classical computer.

Currently, the research in the platforms that offer natural qubits is still active as they have served as trial platforms and have already made possible the implementation of some quantum information protocols and some quantum algorithms. The study of such platforms fosters the development of new experimental techniques and devices to manipulate quantum physical systems; also provides a feedback to the models implemented in quantum control theories specially in problems with many degrees of freedom, like the mutual

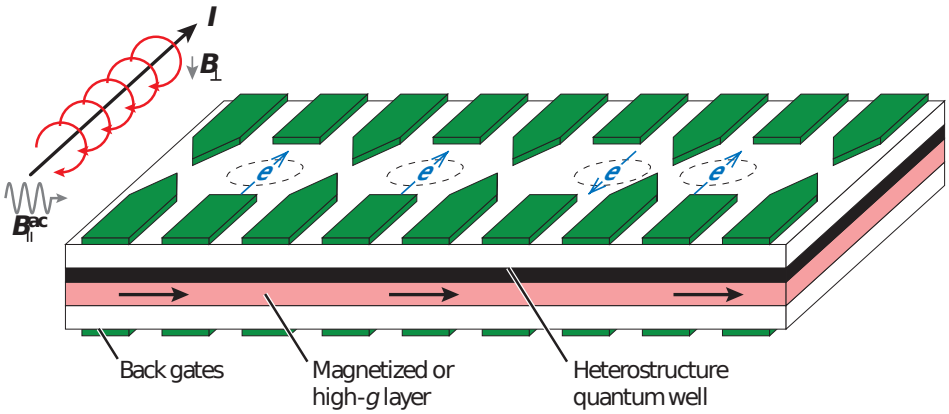

Figure 1.1: As more and more qubits are required to process higher volumes of information, the addressability of individual qubits becomes primordial for its scalability. Some platforms like the electrostatic quantum dots, allow the addressing of every electron individually, enabling its control and scalability for various qubits. An example can be seen in the figure representing an array of lateral QDs, where the electrons and their spin can be manipulated in every quantum dot of the device via electrical gates. (image from C. Kloeffel, D. Loss, [27]).

interacting nuclear spins of complex molecules in the NMR platform [69], or to test the schemes that deals with decoherence, that is still present. Thus these platforms constitute an ideal testbed for the models that attempt to describe the interaction of the system with the environment and of course for quantum information realizations. However, as more and more qubits are required to process higher volumes of information, the addressability of individual qubits becomes primordial for its scalability, to name an example, in the case of NMR the qubit is encoded in the nuclear spin of ensembles of various molecules, and they are manipulated via radio-frequency pulse techniques, also the equipment used for cooling and trapping these ensembles limit their scalability [19]. On the other hand semiconductor based platforms offer the possibility to address one by one the physical elements where the qubits are encoded, e.g. in an array of electrostatic quantum dots like the one in figure 1.1, where the electrons and their spin can be manipulated in every quantum dot of the device via electrical gates (a kind of electrical contacts with high precision). Also the superconducting circuit qubits represent a promising system for quantum computing realizations [22], where the von Neumann architecture (the structure design of a computer), has already been experimentally implemented. Also with the improvement of technology and quantum control, it is expected to suppress or mitigate the adverse effects of decoherence in these platforms, as has been shown in the last decades [23, 24]. In our study we will focus in the platform of quantum dots, thus let us review the types of quantum dots that exist.

1.2 Quantum Dots

Quantum dots QDs were theorized in the 1970s and initially created in the early 1980s, they are semiconductor devices able to confine electrons in space, allowing the manipulation of the electrons, and have had a long trajectory since its first proposal as a platform for a quantum gate in 1998 by Loss-DiVincenzo in [30]. Also QDs are among the platforms with promising scalability [29], supported by the fact that some of their platforms allow to address every electron individually [27]. Thus it is in principle a platform that satisfies the DiVicenzo requirements. Furthermore, the realization of a controlled-NOT (CNOT) gate has been experimentally realized for an optical quantum dot [25], and numerically found to be feasible in a nanowire quantum dot [91]. Also, a numerical exploration shows the enhancing of entanglement of two electrons in a double quantum dot, via electric fields and spin-orbit coupling [92]. Being entanglement a useful resource used in various quantum information protocols like quantum teleporting and dense coding [59].

In QDs, the information can be encoded in the electron spin degree of freedom and are known as *spin qubits*, but also in the discrete spectra of the electronic levels known as *charge qubits*. Currently, the quantum dot spin qubits is the most developed option and the implementation of single and two qubit gates in this platform allows to perform universal quantum computing [31]. The main strength of this platform comes from the fact that spins are relatively isolated from the environment, which provides longer lifetimes and lower decoherence influence. But this isolation also makes it difficult to control such system, requiring long manipulation times. On the other hand, devices based on charge qubits have short manipulation times of the order of picoseconds, providing fast information processing but shorter decoherence times [32, 31]. A new platform called *hybrid qubit* emerged in recent years [33], which combine both spin and charge qubits in double quantum dots (DQDs) to achieve fast manipulation and long decoherence time [33]-[39].

1.2.1 Physical platforms for the quantum dots

Physically there are various types of quantum dots, each with different mechanism of control, decoherence and relaxation times. Here we briefly present their characteristics.

Electrostatically defined quantum dots : Also called lateral quantum dots, they are implemented in semiconductor heterostructures (an intercalation of various semiconductor layers) that offer confinement in one direction. Reducing the free space of the electrons to a plane, where they effectively behave like a two-dimensional electron gas (2DEG). Then Ohmic contacts are soldered on the top of the heterostructure, these contacts are used to apply electrical potentials that depletes the electrons in the 2DEG, except in some regions of interest where the electrons remain confined and ready to be manipulated by

electrical gates. The whole device can be seen in figure 1.2 a), where it is also indicated the confinement region corresponding to two QDs. Manipulation of the spin and the electronic states can be applied via magnetic resonance or a combination of electric fields and a position-dependent effective magnetic field with the methods of electric spin resonance (ESR) or electric dipole spin resonance (EDSR) [112], treated with more detail in chapter 4. They operate at temperatures of $\lesssim 1$ K, and offer encoding of the qubits in the states of one electron (in the individual spin $|\uparrow\rangle, |\downarrow\rangle$), two electron states (offering 4 possible states in the singlet and triplet states), or three electron states (in a direct product of the first two, offering 8 different states) [27, 39]. The proposal of Loss-DiVincenzo in ref. [30], to use quantum dots as a platform for quantum computing was done for this kind of QDs, which can also be set in an array as shown in figure 1.1, representing an scalable proposal to couple as many qubits as possible by the state of the art technology. The decoherence time for this platform in the case of singlet-triplet states is 276 μs , and the relaxation time is up to 5 ms, as reported in [116].

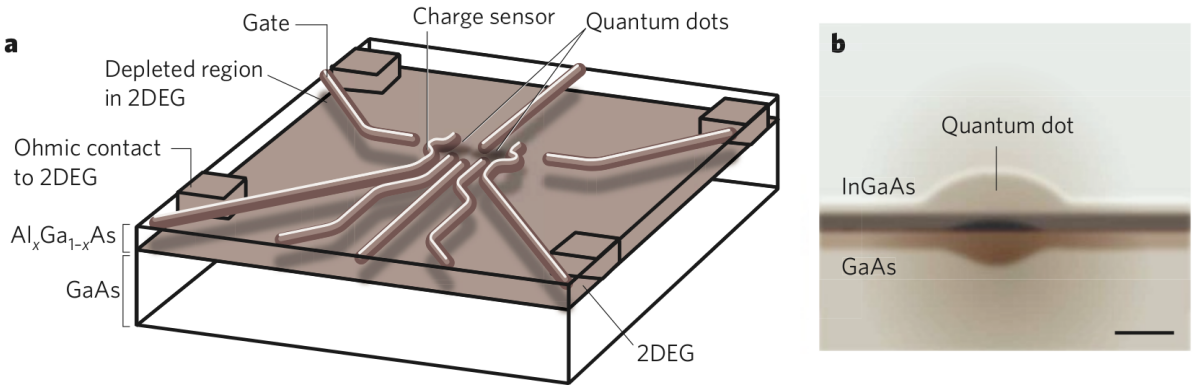

Figure 1.2: a) Electrostatically defined quantum dots, the size of this device is of the order of a few μm. b) Self-assembled quantum dot, the scale bar is ~ 5 nm. (image from T. D. Ladd, *et. al.*, [19]).

Self-assembled quantum dots: They are constructed through precise semiconductor deposition techniques as molecular beam epitaxy (MBE), where the layers of semiconductors are growth by vaporized materials over a larger film of a different semiconductor. In the picture of figure 1.2 b), we can see an small islands of semiconductor material such as indium gallium arsenide (InGaAs) grown within a matrix of a semiconductor with a larger bandgap, such as GaAs. This difference of bandgap confine charge carriers in the island, which due to its geometry and dimensions, provides confinement in the 3 dimensions. Electrical gates can be added to regulate the number of carriers in this QD. The spin of the carriers are manipulated optically through lasers. They operate at temperatures of ~ 4 K. The decoherence time for this platform is 3 μs , and the relaxation time 20 ms, as reported in ref. [116].

Gated nanowire quantum dots: Consisting of a thin semiconductor wire, whose cylindrical geometry offers confinement in the transversal direction of the nanowire, while electrical potentials confine the electrons in the axial direction. Thus offering the characteristic 3 dimensional confinement of a quantum dot. The electrical potentials are provided by an static electric field applied through electric gates soldered at the extremes of the nanowire as shown in picture 1.3, such that the effective potential of the static field in the axial direction correspond to a one-dimensional quantum well. It is possible to create multiple QDs by soldering more electrical gates in the middle of the nanowire, and these additional gates provide effective potentials, in the axial direction of e.g. a double or triple (or more) quantum wells depending on the configuration. The quantity of electrons inside every QD is also regulate by the electrical gates. The qubit can be encoded in the electronic levels of the quantum wells and the electronic spin (for materials with spin-orbit coupling). The manipulation of these states is realized via time dependent electrical pulses applied through the electrical gates and ESR or EDSR. For quantum computation purposes, they operate at temperatures of$\sim$ 4 K. The decoherence time for this platform is 0.16 μs , and the relaxation time is up to 1 μs, as reported in ref. [116].

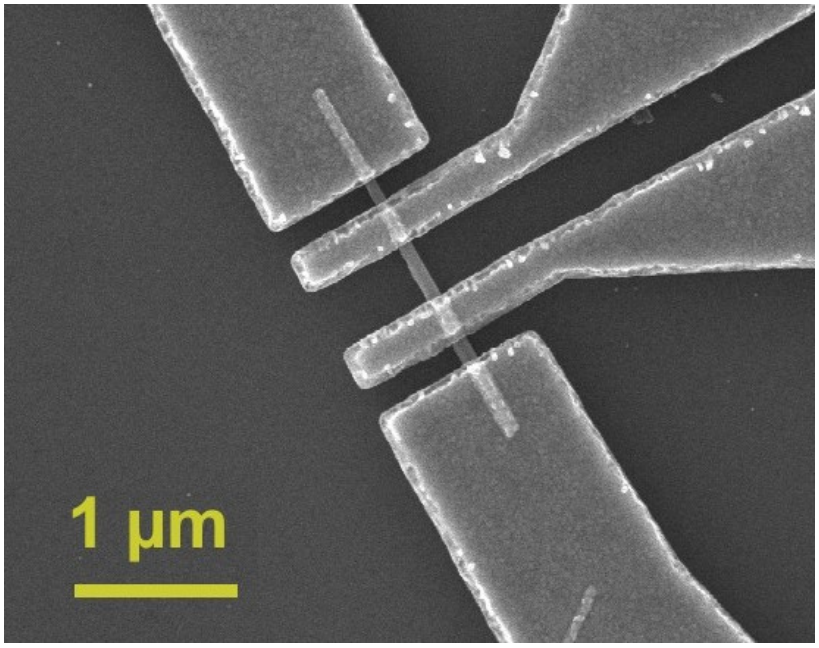

Figure 1.3: Gated Nanowire quantum dot. (image from Peter Grünberg Institute, Germany).

1.3 Quantum control theory

The precise control of quantum phenomena is a long-standing dream, specially when it is related to the implementation of quantum information protocols. Quantum control theory offers a set of tools, that allows to control the physical systems as quantum devices, and

has succeeded in various platforms, where due to the use of optimal control pulses, it is noticeable the improvement in the performance of these devices at their respective tasks. For example, in spin qubits of nitrogen-vacancy centers in ref. [117], there is a remarkable difference in the fidelities of the output states when optimal pulses are used, compared to the standard pulses. There are also other examples in the superconducting circuits platform like the ref. [120] where a CNOT gate was experimentally realized with the assistance of an experimental approach of quantum control theory.

The bridge between quantum information theory and their real applications in the physical platforms requires the assistance of the quantum control theory, which involves the manipulation of physical and chemical processes at the atomic and molecular scale. From the numerical quantum control approaches, the most versatile is QOCT (Quantum optimal control theory). Since most of the interactions in quantum mechanics are mediated via electromagnetic fields, thus the tailoring of optimal fields through optimization methods is one of the main goals of QOCT.

The optimization methods of QOCT represent a powerful tool which offers shortcuts in the dynamical evolutions and allow us to perform any transformation from an initial state to a desired final target state by tailoring an optimal driving field that induce the right evolution that connects the initial and final states. The QOCT methods recursively propagate the dynamical equations, and modulate the driving field in every iteration, avoiding undesired paths in the evolution, until the method identifies an optimized field able to reach the target state with a required precision.

The other numerical approach of quantum control theory is coherent control, which mainly exploits interferometry of a physical parameter (e.g. the phase between two lasers), and make use of harmonic non-modulated pulses. However this approach is still suitable and enough for processes involving few degrees of freedom like molecular photodissociation. Usually the optimized pulses perform the same task in shorter time than coherent control. However the versatility of QOCT comes at the trade off of complex profiles in the optimized pulses, since these methods usually yield non-harmonic and modulated pulses, which require a more sophisticated experimental equipment to be precisely generated.

Quantum control theory has prove to be a useful tool for

- Control of chemical reactions [71, 74, 77].
- Quantum computing in various physical platforms [91, 119].
- Transport in semiconductors [94, 95].
- Quantum dynamics [61, 64].

In this study we explore numerically the feasibility of quantum gates in two different platforms of quantum dots, with the assistance of a QOCT method, and we also compare

its dynamical efficiency with respect to other dynamical mechanisms (Rabi and Landau-Zener).

1.4 Thesis Outline

In chapter 2, we examine the dynamical evolution of a qubit (a two-level system) under the action of an oscillating and linear driving field for different parameter regimes. For low amplitudes (weak regime), the temporal evolution manifest Rabi oscillations, and for high amplitudes (strong regime) the Landau-Zener effect takes place. But the shifting from one dynamics to the other it is not as simple as to apply a more or less intense driving field. Thus, we also discuss what are the determinant factors that allow the observation of one dynamics or the other. In chapter 3 we present a brief review of the theory of quantum optimal control theory (QOCT), its origins and state of the art, we also discuss its strength and limitations compared with the other quantum control theory strategies. Then we present the quantum optimal control method, the two-point boundary-value quantum control paradigm (TBQCP), that we applied to identify the optimal fields that induce a temporal evolution from an initial state to an specific target state. Such optimization method is an alternative and powerful tool which offers shortcuts in the dynamical evolutions, and allow us to perform any transformation of a pure state. Also we explain how to apply this method for the implementation of quantum gates. In chapter 4, we begin by introducing the physics of the nanowire quantum dot platform, and the interactions that can be exploited for its manipulation. Then we characterize the level structure and the presence of the different dynamics (Rabi and Landau-Zener) in the setups for an electron in a single and a double quantum dot systems. Later, we implement the TBQCP method to tailor optimal fields corresponding to three different one-qubit quantum gates, and we compare its efficiency with the dynamical mechanisms previously analyzed. At the end we decompose the optimized fields and reconstruct them with Fourier analysis in order to determine how many Fourier coefficients are enough to reconstruct a pulse that perform the same task of the optimal fields with a satisfactory precision. A problem relevant for the experimental generation of optimal fields and for quantum metrology. In chapter 5, we use the TBQCP method, but this time to assess the physical implementation of a quantum algorithm in the platform of gated lithographic double quantum dots. We describe the quantum algorithm and the quantum gates involved in its execution. Although such quantum algorithm requires the optimization of eight electrical pulses corresponding to the different quantum gates, its execution requires the application of three of these quantum gates in sequential order. The electric pulses are optimized with the aid of the TBQCP method in the quantum speed limit, guaranteeing successful transformations (with high fidelity) for any of the implemented quantum gates. At the end of the chapter we compare the total time required by an hypothetical execution

of this algorithm with the decoherence and relaxation times of the physical platform, and we also evaluate the performance of such execution under a noisy environment. Finally in chapter 6, we discuss the results and conclusions offered by this thesis, and give some future perspectives to be explored in the problems here studied.

Chapter 2

One qubit dynamic

In this chapter, first we review the definition and mathematical formulation of the qubit, then we examine the dynamical evolution of a two-level system under the action of an oscillating and linear driving field for different parameter regimes, which give rise to different temporal evolutions, depending on the amplitude of the field compared to the separation of the levels. For low amplitudes (weak regime), the temporal evolution manifest Rabi oscillations, and for high amplitudes (strong regime) the Landau-Zener phenomenon leads the temporal evolution of the states. But to go from one dynamics to the other it is not a mere matter of the field strength, therefore we explain the specific elements required to observe one dynamics or the other.

2.1 The quantum bit

A bit is an information unit of two possible states and the qubit is its quantum version. Novel physical resources that allow new ways to process and communicate information appear in the quantum case because the possibility of superposition of the two states and entanglement between different qubits. The qubit is mathematically represented as an unitary vector in the complex bidimensional vectorial space, for which it is defined the two dimensional basis in the Hilbert space:

$$|0\rangle = \begin{pmatrix} 1 \\ 0 \end{pmatrix}, \quad |1\rangle = \begin{pmatrix} 0 \\ 1 \end{pmatrix}, \tag{2.1}$$

known as the computational basis, in analogy to the classical computation, which only allows the states of 0 or 1. On the other hand, due to the quantum superposition, a general state can be written as

$$|\psi\rangle = a|0\rangle + b|1\rangle, \tag{2.2}$$

with a and b complex numbers, satisfying $|a|^2 + |b|^2 = 1$. Hence it is possible to establish a geometrical representation where the state $|\psi\rangle$ corresponds to a point on the surface of unitary sphere for pure states, called the Bloch sphere. The equation (2.2) can be rewritten up to a global phase factor as [48]

$$|\psi\rangle = \cos\frac{\theta}{2}|0\rangle + e^{i\phi}\sin\frac{\theta}{2}|1\rangle,$$

where the values between $0 \leq \theta \leq \pi$ and $0 \leq \phi < 2\pi$ define the point in the Bloch sphere corresponding to the state vector $|\psi\rangle$ (see figure 2.1).

Ideally, the qubit is realized in two-level quantum systems and, in this chapter, we review some relevant features of their dynamics.

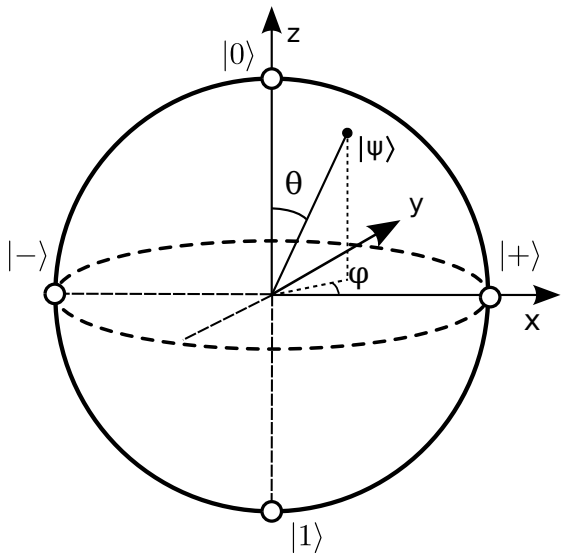

Figure 2.1: Bloch sphere representation of a qubit in the state $|\psi\rangle$.

2.2 Rabi Model

One of the simplest quantum dynamics can be seen in the two-level quantum system interacting with an oscillating driving field. Despite its simplicity, this problem does not always have an analytical solution. In Ref. [49] it is studied the case of a rotating magnetic field, which has an exact solution for the probability occupation of the two levels. The system consist of a spin 1/2 particle precessing under the action of a rotating field, described by the Hamiltonian:

$$H(t) = \omega_L \hbar S_z + \omega_1 \hbar \left[S_x \cos\omega t + S_y \sin\omega t\right], \tag{2.3}$$

with ω_L, the Larmor precession frequency associated to a constant magnetic field along $\hat{z}$ direction, ω_1 the amplitude of a second time-dependent magnetic field rotating in the xy plane, and ω the angular frequency of this rotating magnetic field.

By solving the time dependent Schrödinger equation for this Hamiltonian, represented in the basis of $\hat{S}_z$ (usually associated to the same states of the computational basis $|0\rangle$ and $|1\rangle$), the probability occupation of $|1\rangle$ is given by:

$$P_1 = |\langle 1|\psi(t)\rangle|^2 = \frac{\omega_1^2}{\omega_1^2 + (\delta\omega)^2} \sin^2\left[\sqrt{\omega_1^2 + (\delta\omega)^2}\frac{t}{2}\right], \tag{2.4}$$

with $\delta\omega = \omega - \omega_L$, a detuning between the rotating driving field and the Larmor precession frequency of the constant magnetic field.

The physics of the Rabi model exhibits a characteristic dynamics where the probability occupation oscillates between both states as the numerical solution[1] shown in the orange plot of figure 2.2), this phenomenon is known as "Rabi oscillations".

On the other hand, for the non-analytic two-level quantum systems, it is possible to approximate its time dependent Schrödinger equations, to a Rabi like problem with an analytical solution. This method, is known as the Rotating Wave Approximation method (RWA), in which the driving field is rewritten as a rotating field, by neglecting high frequency terms, allowing the exact resolution of the problem.

As an illustrative example, we study a two-level system under the action of a sinusoidal driving field described by the Hamiltonian (we take $\hbar = 1$ for this example)

$$H_R = \frac{\Delta}{2}\sigma_z + \frac{\epsilon(t)}{2}\sigma_x, \tag{2.5}$$

with system energies $E_1 = -\Delta/2$ and $E_2 = \Delta/2$, associated to the $|0\rangle$ and $|1\rangle$ states respectively, and Δ a parameter that determines the energy separation of both levels. The time-dependent field is defined as

$$\epsilon(t) = A\sin(\omega_0 t). \tag{2.6}$$

We start by appliying the RWA in our Hamiltonian of eq. (2.5), under the action of the oscillating pulse in eq. (2.6). But first, let us define the time-dependent state $|\psi(t)\rangle$ at any time. Expressed in terms of the computational basis in eq. (2.1)

$$|\psi(t)\rangle = c_1(t)|0\rangle + c_2(t)|1\rangle. \tag{2.7}$$

With such state in the time dependent Schrödinger equation we have,

$$i\frac{\partial}{\partial t}c_1(t) = E_1 c_1(t) + \frac{A}{2}\sin(\omega_0 t)c_2(t), \tag{2.8}$$

$$i\frac{\partial}{\partial t}c_2(t) = E_2 c_2(t) + \frac{A}{2}\sin(\omega_0 t)c_1(t). \tag{2.9}$$

This differential equation system has no analytical solution, but an approximate solu-

[1] All the numerical solutions in this chapter were implemented with an exponential propagator.

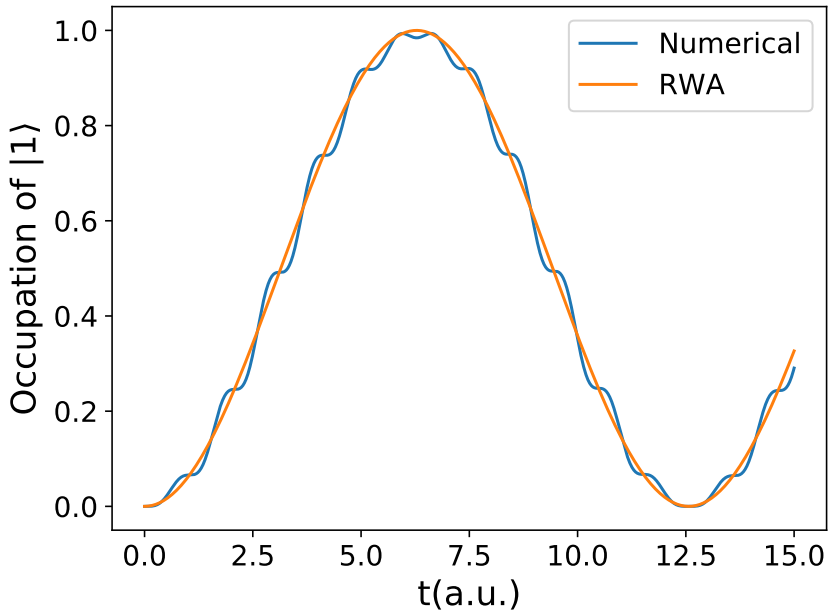

Figure 2.2: The temporal evolution for weak driving fields is characterized by Rabi oscillations. Here the parameters are $\Delta = 3$, $\omega_0 = 3$, $A = 1$ and $\epsilon_0 = 0$ for our Hamiltonian with a sinusoidal field (blue) and for the Hamiltonian with exact solution (orange). Rabi oscillations are characteristic of a regime of parameters that satisfies $A/\Delta \lesssim 1$ and $\omega_0 \approx \Delta$. Temporal evolution represented in the Sz basis.

tion can be found as shown in appendix A, by applying the RWA method, which yields the following equation system

$$i\frac{\partial}{\partial t}b_1(t) = \omega_u b_1(t) - \frac{iA}{4}b_2(t), \tag{2.10}$$

$$i\frac{\partial}{\partial t}b_2(t) = (\omega_d - \omega_0)\, b_2(t) + \frac{iA}{4}b_1(t), \tag{2.11}$$

with $b_1(t) = c_1(t)$, and $b_2(t) = c_2(t)\exp(i\omega_0 t)$. If we solve this equation system with an initial condition of $|\psi(0)\rangle = |0\rangle$, then the probability $P_1(t)$ of finding the state $|1\rangle$ is (see appendix A):

$$P_1(t) = |\langle 1|\psi(t)\rangle|^2 = \frac{A^2}{A^2 + 4(\omega_0 - \Delta)^2}\sin^2\left[\sqrt{A^2 + 4(\omega_0 - \Delta)^2}\frac{t}{4}\right], \tag{2.12}$$

which share a similar form with eq. (2.4).

For the particular case of weak driving fields (i.e. with amplitude $A \lesssim \Delta$) and close to resonance ($\omega_0 \approx \Delta$), the problem of eq. (2.5) (with the sinusoidal field) and the exact solution (obtained via RWA) are pretty similar as we can see in figure 2.2, where the dynamics of the system is characterized by Rabi oscillations, with the RWA solution as an envelope function of the numerical simulation. In general, the RWA can be used for

driving fields close to resonance, satisfying $|\omega_0 - \Delta| \ll |\omega_0 + \Delta|$ [46], since the net input of high frequency terms like $\omega_0 + \Delta$ are null in average, therefore they can be neglected.

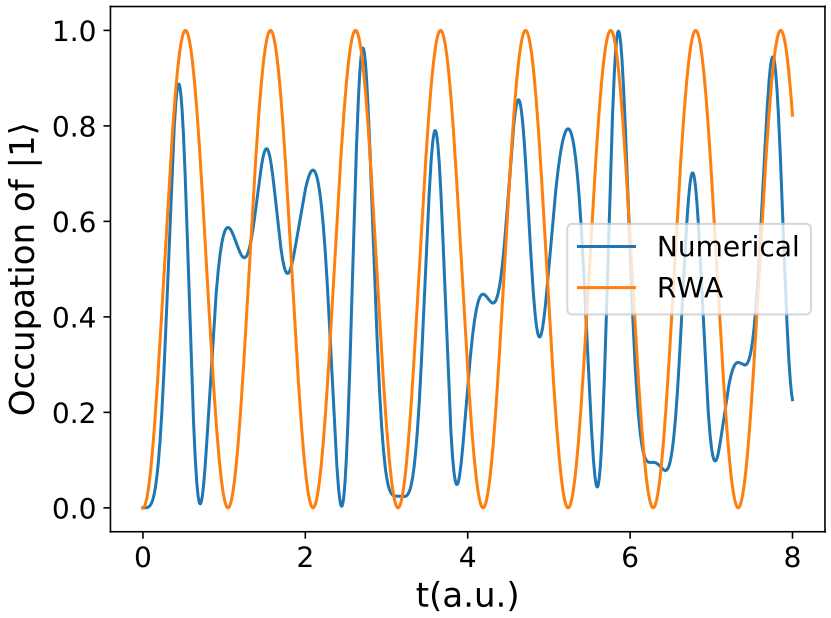

Figure 2.3: For an intermediate driving field, in this case with $\Delta = 3$, $\omega_0 = 3$, $A = 12$ and $\epsilon_0 = 0$, the temporal evolution departs notably from the dynamics of Rabi oscillations, as we compare the numerical solution (in blue) to the RWA (in orange).

On the other hand, for intermediate or strong driving fields (i.e. of the amplitude $A > \Delta$), the RWA does not give a good resemblance of the numerical solution (even in the resonance) for the sinusoidal field (see figure 2.3), as other phenomena could come to play a significant role, e.g. adiabatic transitions, or in atomic physics, the multiphoton phenomenon to name some examples [47].

2.3 Landau-Zener

Let us think, without loss of generality, in the simplest case of a two-level system with two non-degenerate energy states coupled by an interaction. When an external parameter associated with the coupling variates the system energy (e.g. by an external field) in a rapid way (diabatic) by multiple passages (or even a single one) through the anticrossing region, the field induce a transition in the probability occupation, known as Landau-Zener transition. This transition is dynamically different and, depending on the parameters, can be faster than Rabi's population inversion. Thus, it constitutes an alternative mechanism to manipulate the state occupation of a physical system.

This problem was first studied in 1932 by Landau [51] and Zener [50]. They arrived independently to an approximated model with the exact solution of a one-dimensional

semi-classical model for nonadiabatic transitions. It was also studied at that time by Majorana [52] and Stückelberg [53] with different approaches [54], but since the exact solution of the first two authors applies approximately for many cases, the Landau-Zener model is the one better known. Our revision of the Landau-Zener physics is based on the review of Ref. [55].

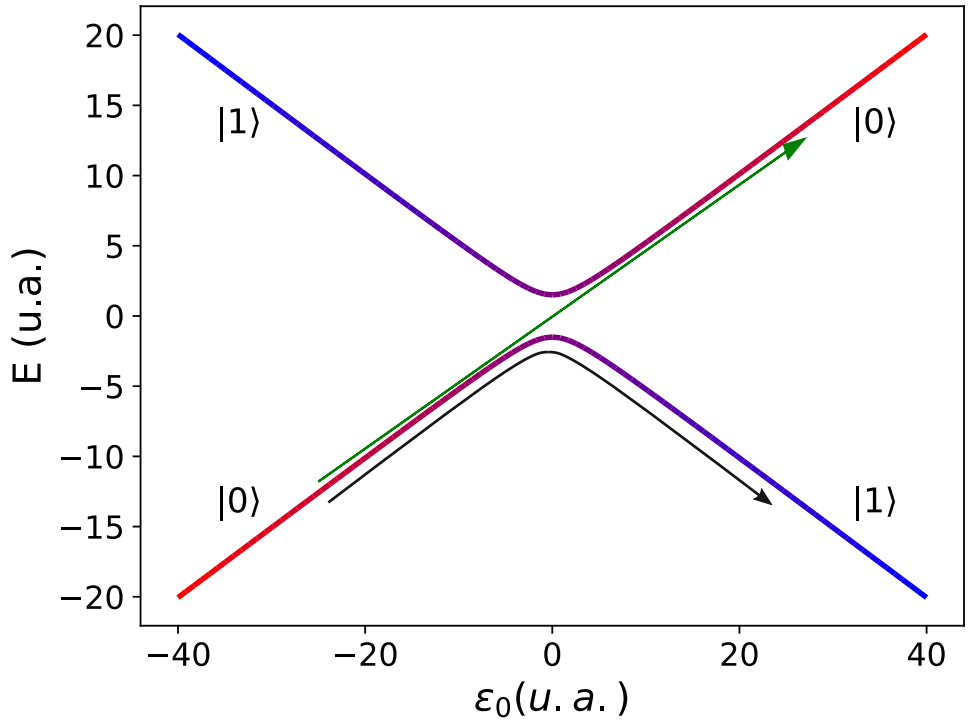

Figure 2.4: Energy level structure for the Hamiltonian in (2.13) with $\Delta = 3$, and $\epsilon(t) = \epsilon_0$. This energy structure presents two energy curves and an anticrossing, and there is a swapping in the state configurations in every energy curve of the system. This is represented by the different colors that change from one into the other from the beginning to the end of both branch of energy. In green, we depict a linear pulse applied to pass once through the anticrossing and generate a Landau-Zener transition.

We want to study the probability transitions of a two-level system under the action of a constant field in the $\hat{x}$ direction and a time-dependent field in the $\hat{z}$ direction, described by the Hamiltonian

$$H_{LZ} = -\frac{\epsilon(t)}{2}\sigma_z + \frac{\Delta}{2}\sigma_x, \tag{2.13}$$

with a time-dependent field $\epsilon(t)$ defined as the oscillating pulse

$$\epsilon(t) = \epsilon_0 + A\sin(\omega_0 t), \tag{2.14}$$

where ϵ_0 is an static field added to the driving force.

This apparently simple problem has no analytical solution, however for some regime

of parameters it is valid to do a linearization of the driving field in eq. (2.14),

$$\epsilon(t) = \epsilon_0 + A\omega_0 t, \tag{2.15}$$

where the factor $\kappa = A\omega_0$, corresponds to a velocity in this linear pulse. Such linearization turns the Hamiltonian of eq. (2.13) into a new solvable system with solutions that are consistent with numerical simulations and experimental realizations.

The dynamics of this system depends of the regime of operation, the amplitude must be $A > \Delta$ (strong regime). Differently from the Rabi regime, the static field ϵ_0 is not restricted to zero, and it is important that the pulse (whether oscillating or linear) must pass through the anticrossing, thus the amplitude must be always greater than the static field, i.e. $A \geq \epsilon_0$.

The passages through the anticrossing can be slow or fast depending on the frequency of the pulse. The Landau-Zener effect occurs when the pulse is fast. But in order to better understand it, let us first analize what occurs when the pulse is slow.

Slow passage

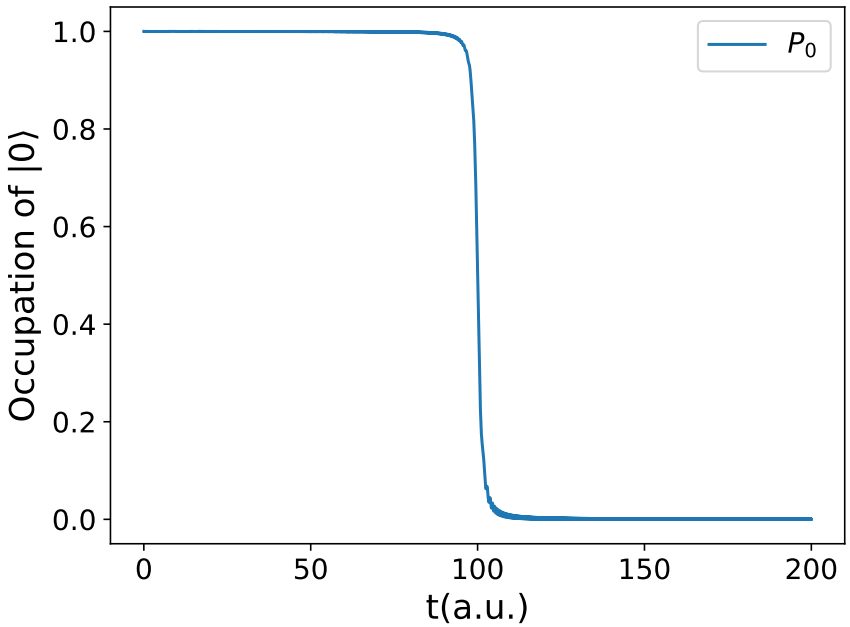

Figure 2.5: Adiabatic evolution due to the slow passage of a linear pulse which pass once trough the anticrossing region with an initial condition of $|\psi(0)\rangle = |0\rangle$ (represented in the Sz basis). For a level separation of $\Delta = 3$ and a linear pulse with $A = 50$, $\omega_0 = 0.04$, $\epsilon_0 = -200$ (all parameters are adimensional). In this case the evolution never gets out of the inferior energy curve in figure 2.4.

For a slow passage of the the linear pulse in eq. (2.15) (which physically corresponds to $\omega_0 \ll \Delta$), the action of the pulse is weak and the state occupation will tend to match with

the instantaneous eigenstates determined by the static field ϵ_0. Thus the state evolution will follow the energy curve, where the initial state was set, whether the top or the inferior energy curve in the level structure of figure 2.4. Hence after passing the anticrossing under the action of an slow driving field as illustrated by the black arrow in figure 2.4, there will be a transition in the state configuration between $|0\rangle$ and $|1\rangle$ in order to keep the system in the initial state. This swap in the state configuration is illustrated by the different colors that change gradually from state $|0\rangle$ (in red) to $|1\rangle$ (in blue). This dynamics is expected according to the Adiabatic theorem [56], and its respective temporal evolution can be seen in figure 2.5, for the parameters $A = 50$, $\omega_0 = 0.04$, $\epsilon_0 = -200$.

Fast passage

For a fast $\omega_0 > \Delta$ or intermediate $\omega_0 \geq 0.1\Delta$ passage of the field, and the intermediate field regime of the amplitude, i.e. $A > \Delta$, the relevant quantities in the Hamiltonian of eq. (2.13) will be the terms A and ω_0 of the pulse. First, let us review the analytical solution of the problem by applying the linearized pulse in eq. (2.15) and considering a single swept in the intensity of the pulse from $-\infty$ to ∞, as Zener did in his paper [50]. The time-dependent Schrödinger equation is[2]

$$i\frac{\partial}{\partial t}\begin{pmatrix} C_0 \\ C_1 \end{pmatrix} = \begin{pmatrix} -\frac{A\omega_0 t}{2} & \frac{\Delta}{2} \\ \frac{\Delta}{2} & \frac{A\omega_0 t}{2} \end{pmatrix}\begin{pmatrix} C_0 \\ C_1 \end{pmatrix}. \tag{2.16}$$

This differential equation system can be decoupled by derivating the first equation and then replacing the first and second equation on itself. This let us with the equation (remembering that $v = A\omega_0$)

$$\ddot{C}_0(t) + \left[\frac{(A\omega_0)^2}{4}t^2 - i\frac{v}{2} + \frac{\Delta^2}{4}\right]C_0(t) = 0. \tag{2.17}$$

The solution to this second-order differential equation can be found in [57], corresponding to the parabolic cylinder functions, which resolve the Weber equation. Taking this solution and the second equation of (2.16), it is possible to find $C_1(t)$ from

$$C_1(t) = i\dot{C}_0(t) + \frac{v}{2}C_0(t).$$

It is also neccesary to apply asymptotic expansions on the solutions of the parabolic cylinder functions for the limit when $t \longrightarrow \infty$, which can be found in [50]. If our initial condition is $C_0(0) = 1$, by following the mentioned steps, we arrive at the Landau–Zener probability:

$$P_{LZ} = \exp\left(-2\pi\frac{\Delta^2}{4v}\right), \tag{2.18}$$

[2]For the analitical solution with a pulse starting at $-\infty$, the constant ϵ_0 can be neglected.

which predicts the final occupation $P_0 = |C_0|^2$ of the system after the linear swept.

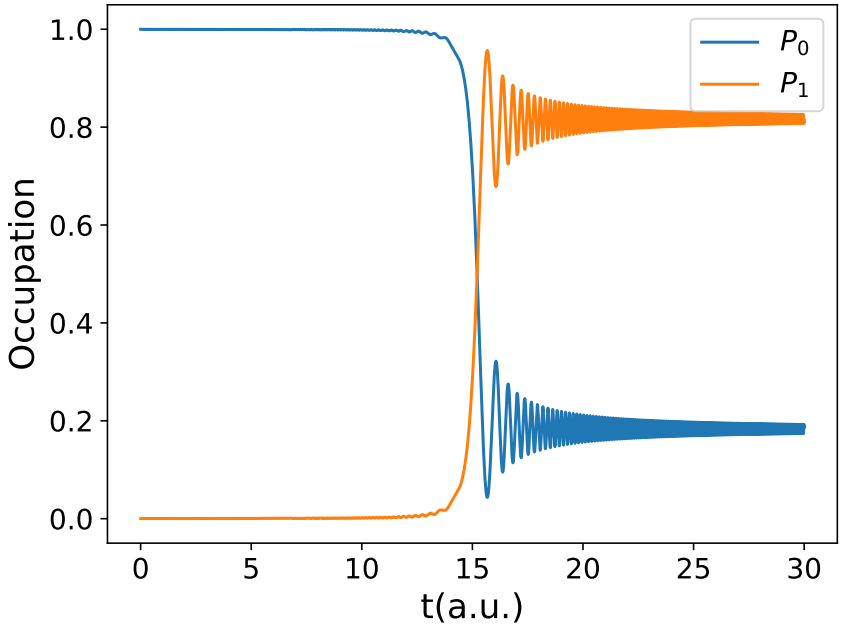

Figure 2.6: Landau-Zener effect for a linear pulse which pass once trough the anticrossing region and an initial condition of $|\psi(0)\rangle = |0\rangle$ (represented in the Sz basis). For a level separation of $\Delta = 3$ and a linear pulse with $A = 55$, $\omega_0 = 0.15$, $\epsilon_0 = -123.75$ (all parameters are adimensional).

As an illustrative example, we solve numerically the time dependent Schrödinger equation with the Hamiltonian of eq. (2.13). If we start with an initial condition of $|\psi(0)\rangle = |0\rangle$, i.e. $C_0(0) = 1$, by considering one swept through the anticrossing region under the action of the linear pulse in eq. (2.15) (with ϵ_0 finite but large for practical purposes like the green arrow in figure 2.4). We obtain the numerical simulation in figure 2.6, with parameters in the linear pulse of $A = 55$, $\omega_0 = 0.15$, $\epsilon_0 = -123.75$, and a level separation of $\Delta = 3$. The occupation of the state $|0\rangle$ is correctly predicted by the Landau–Zener formula (2.18) with an occupation of $P_{LZ} = 0.18$ from the initial occupation $P_0(0) = 1$, to the final occupation of $P_0(30) = 0.18$ as can be seen in the blue plot of figure 2.6. For these parameters, the Landau–Zener formula predicts a superposed state where both energy curves of the level structure in figure 2.4 are populated. This is confirmed by our numerical results, where the occupation for the state $|0\rangle$ (in blue) at the final time $T = 30$ a.u. is not completely zero (as occurred in the adiabatic case of figure 2.5, where the state remained in one energy curve). This happens because the fast pulse induce a transition to a mixed state $a|0\rangle + b|1\rangle$, involving both energy curves in the level structure depicted in figure 2.4. If we look carefully at the temporal evolution in figure 2.6, we see that before passing the anticrossing, before $T = 14$ a.u., the state $|0\rangle$ (in blue) was fully populated. But once the anticrossing is passed, the population of the state $|0\rangle$ is not fully transferred to the other state (as happened in the adiabatic case figure 2.5 for the slow

pulse). Instead both states end up partially populated, implying a partial occupation of both energy curves shown in figure 2.4.

2.3.1 Multiple passage

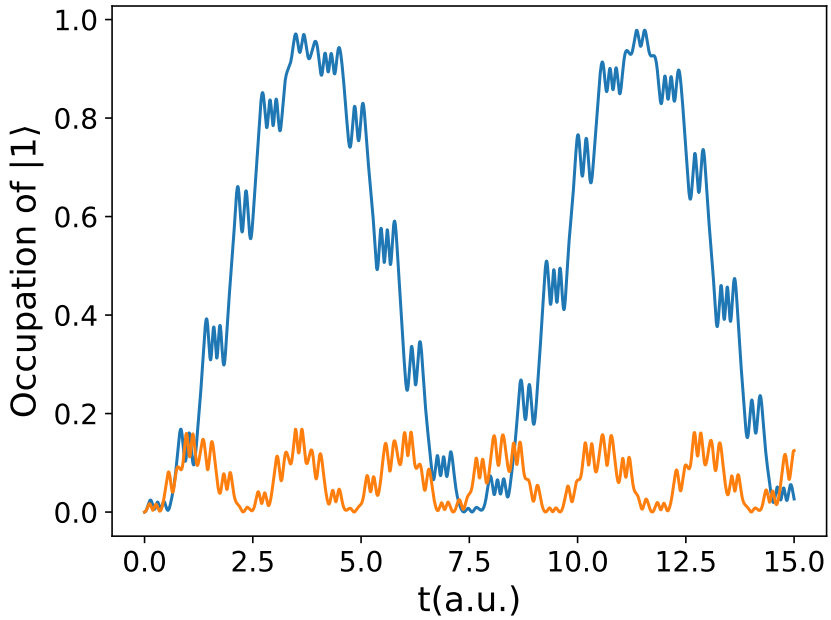

Figure 2.7: Constructive (blue) and destructive (orange) interference of the Landau-Zener transitions after multiple passage through the anticrossing region with a sinusoidal pulse defined as $\epsilon(t) = \epsilon_0 + A\sin(\omega_0 t)$, and an initial condition of $|\psi(0)\rangle = |0\rangle$. Parameters: $\Delta = 3$ and a pulse with $A = 40$, $\epsilon_0 = 5$, for both plots and $\omega_0 = 4.8$ for constructive and $\omega_0 = 7.5$ for destructive interference. Temporal evolutions represented in the Sz basis.

The temporal evolution dynamics becomes more interesting by repeatedly driving the system through the avoided crossing with a sinusoidal pulse, which leads the temporal evolution under the influence of multiple passages through the anticrossing, back and forward. Repeating several times the transition described in the previous section, introduces additional effects in the dynamics since the multiple passage can generate constructive or destructive interference, depending on the parameters of the pulse. Particularly relevant is the case of constructive interference, since the multiple transitions can achieve an inversion population faster than a Rabi oscillation. Therefore, if a physical system has an anticrossing (and its regime parameters are experimentally feasible), the Landau-Zener transition can constitute a more versatile process to control the state occupation of a physical system than Rabi oscillations.

There are analytical methods, like the Stückelberg interferometry [55], that allow to identify the parameters of A, ϵ_0 and ω_0 for a fixed value of the energy separation Δ leading to a constructive or destructive interference, but they are out of the scope of this

study. Nevertheless with the assistance of numerical methods, like the grid search, we are able to identify such parameters, as can be seen in figure 2.7, where we have constructive interference (blue plot) for $\Delta = 3$ and a pulse with $A = 40$, $\epsilon_0 = 5$ and $\omega_0 = 4.8$; and destructive interference (orange plot) for $\Delta = 3$ and a pulse with $A = 40$, $\epsilon_0 = 5$ and $\omega_0 = 7.5$. These parameter sets were found with the mentioned grid search method on the amplitude and frequency of the harmonic pulse; where a grid with these two parameters is created, and then with the values of such grid, the temporal evolution is evaluated for a fixed time. For every temporal evolution, the area below the curve for the occupation of state $|1\rangle$ is calculated. In the case of constructive interference, we selected the set of parameters where such area is maximum, while for destructive interference, we selected the set of parameters where such area is minimum.

2.4 Rabi and Landau-Zener, two sides of the same coin

The main difference between the Hamiltonians of equations (2.5) and (2.13) is that the first has the time-dependent matrix elements out of the diagonal, while the second has them in the diagonal. Also, the temporal evolutions (for Rabi and Landau-Zener with multiple passages), when a sinusoidal pulse is applied, as illustrated in figures 2.2 and 2.7, are pretty different. But despite these differences there are connections between the Hamiltonians of both phenomena. A common feature for both Hamiltonians (2.5) and (2.13) is that the level structure is exactly the same, and they are separated at the anticrossing by an energy of Δ as in figure 2.4. Both Hamiltonians can be transformed into each other by means of a rotation in the two dimensional Hilbert space of the qubit.

Any rotation along the Cartesian axes of the Bloch sphere can be performed by the unitary operator

$$R_j(\theta) = \exp(-i\theta/2\sigma_j), \qquad j = x,\, y,\, z, \tag{2.19}$$

with σ_j as one of the Pauli's Matrices and θ the rotation angle [59].

The Rabi Hamiltonian H_R and the Landau-Zener Hamiltonian H_{LZ} are connected by a rotation of $R_y(\pi/2)$ around the y-axis of the Bloch sphere[3], such that

$$H_{LZ} = R_y(\pi/2) H_R R_y^\dagger(\pi/2). \tag{2.20}$$

However, an uinitary transformation does not change the dynamics of the system.

One could be tempted to think that the main link between both phenomena lies in such transformation, which can interchanges the position of the time-dependent matrix elements out or into the diagonal of the Hamiltonians. However, this is not the case. The

[3]Must be an angle of $-\pi/2$ or $\pi/2$, (in our simulations we choose the latter) otherwise the matrix elements will be a mixture of the $\epsilon(t)$ and Δ terms.

physics of both phenomena lies in the regime parameter and the chosing of the correct measurement basis, which is indispensable to observe them. In order to arrive to such conclusion, let us analyse the implications of every regime for the evolution of the systems described by the Hamiltonians (2.5) and (2.13). For the seek of simplicity, let us restrain (without loss of generality) to initial conditions which correspond to enigenstates of either S_z and S_x. Being the eigenstates of S_z

$$|0\rangle = \begin{pmatrix} 1 \\ 0 \end{pmatrix}, \quad |1\rangle = \begin{pmatrix} 0 \\ 1 \end{pmatrix},$$

and the eigenstates of S_x

$$|+\rangle = \frac{1}{\sqrt{2}} \begin{pmatrix} 1 \\ 1 \end{pmatrix}, \quad |-\rangle = \frac{1}{\sqrt{2}} \begin{pmatrix} 1 \\ -1 \end{pmatrix}.$$

From a mathematical perspective, the main difference between both Hamiltonians are the time-independent (let us denote by H_0 the matrix defined by these elements) and time-dependent elements (let us denote by H_i the matrix defined by these elements) in them. For the case of Rabi,

$$H_0 = \frac{\Delta}{2}\sigma_z, \quad H_i = \frac{\epsilon(t)}{2}\sigma_x, \tag{2.21}$$

and in the case of Landau-Zener,

$$H_0 = \frac{\Delta}{2}\sigma_x, \quad H_i = -\frac{\epsilon(t)}{2}\sigma_z. \tag{2.22}$$

As we saw in the first two sections, the Rabi dynamics is pretty susceptible and it only manifest clearly for a weak driving field with specific characteristics; on the other hand the pulse in the Landau-Zener has less restrictions, but must be an strong (or intermediate) driving field. In the following table, we summarize the features of the parameters for a pulse like the one of eq. 2.14

	A	ω_0	ϵ_0
Rabi	$A \lesssim \Delta$	$\omega_0 \approx \Delta$	$\epsilon_0 \approx 0$
Landau-Zener	$A > \Delta$	$\omega_0 \gtrsim \Delta$	$-A \leq \epsilon_0 \leq A$

Table 2.1: Parameter regimes for both dynamics Rabi and Landau-Zener. (Initial conditions supposing we are transforming Rabi into Landau-Zener).

From table 2.1, we see that the pulse required to observe the Rabi dynamics (at the center of the anticrossing) is basically a weak sinusoidal pulse in the resonance and no static field. Thus, in a graph of energy vs static field (with the system level structure), it would look like the blue pulse in figure 2.8. For this reason, this is known as the *weak regime* and, in this case, the time-independent part (the H_0) of both Hamiltonians

(2.5) and (2.13) is more relevant, since at any time, the influence of the parameter Δ will be higher or at least equal to the effect of the pulse amplitude A. The only detail to take in account is to pick the right basis to observe the Rabi dynamics. To get a hint of what measurement basis to use for every Hamiltonian, we can look at equations (2.21) and (2.22), and observe which matrix goes with the relevant factor in this regime (being Δ in this case) which suggest what eigenstates to use. Therefore, for the Rabi Hamiltonian we have the σ_z matrix, which has the associated eigenstates $|0\rangle$ and $|1\rangle$ for the eq in (2.21), and for the Landau Zener Hamiltonian the matrix σ_x, which has the associated eigenstates $|+\rangle$ and $|-\rangle$ for the Hamiltonian of eq. (2.22). These states constitute the best choice to clearly observe a temporal evolution similar to the Rabi dynamics, the initial condition could be any of the respective eigenstates of H_0 indicated for every Hamiltonian. But the initial condition is not really that relevant, it only changes the starting point of the evolution but not the shape of the temporal evolution i.e. its dynamics. The aforementioned implies that it is possible to reproduce the figure 2.2 (obtained with Rabi), but with the Landau-Zener Hamiltonian, by preserving the same parameters (which guaranties the weak regime), and changing the initial condition and the measurement basis to the corresponding eigenstates of σ_x.

The shift from the weak to the strong regime is gradual (represented in figure 2.8 by the evanescent green area). Thus, it is not easy to perceive as a transition from one phenomenon to the other, in part due to the different basis where both phenomena can be observed. What actually can be perceived for an oscillating field (even in the resonance) is that, for an amplitude of $A = 4\Delta$, there is a departure of the temporal evolution from the RWA model as illustrated in figure 2.3. Thus, probably contributions from both Rabi and Landau-Zener are manifested in this regime.

For the *strong regime* $A > \Delta$, where the Landau-Zener is observed, the pulse (2.14), has less restrictions for the parameters (e.g. ω_0 can take any value below or over the resonance frequency), and if we consider a pulse with any arbitrary static field (in the interval $\epsilon_0 \leq |A|$ to guarantee the passage of the pulse through the anticrossing), the closest extreme of the pulse to the center of the anticrossing is $A - |\epsilon_0|$. If this extreme is far away from the influence area of H_0, then the driving field leads the system to stay longer outside this area, where H_i dominates (since the parameters of the pulse A, and ϵ_0 are larger than Δ), as we can get an idea by looking at the red pulse in figure 2.8. In this case, we can look at the matrix H_i of the Hamiltonians in equations (2.21) and (2.22) to get a hint of the best measurement to observe the Landau-Zener dynamics. Hence for the Rabi Hamiltonian we have the matrix σ_x, which has the corresponding eigenstates $|+\rangle$ and $|-\rangle$ and for the Landau Zener Hamiltonian the matrix σ_z, whit their corresponding eigenstates $|0\rangle$ and $|1\rangle$.

The previous statements suggest that it is possible to observe the Landau-Zener phenomenon but using the Rabi Hamiltonian, by preserving the same parameters (which

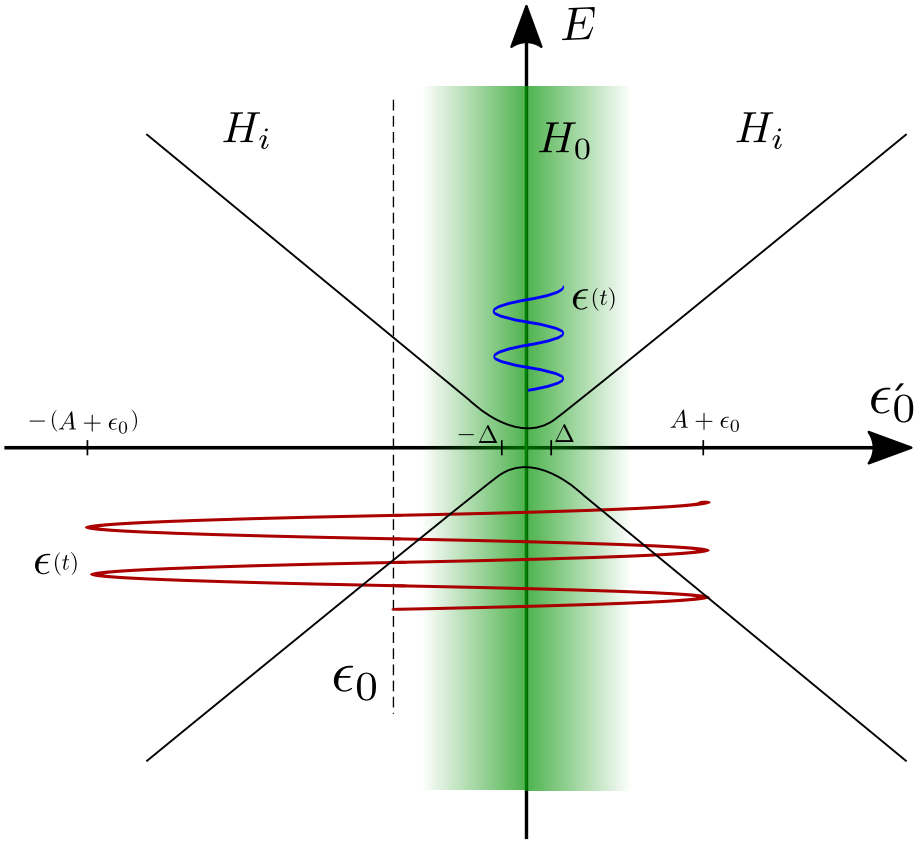

Figure 2.8: Regimes of the driving fields weak for Rabi (blue), and strong for Landau-Zener (red). The green shadow corresponds to an estimation of the interval in the static field where the weak regime leads the temporal evolution and a pulse (in the resonance) inside this region will give rise to a Rabi dynamics similarr to the RWA model inasmuch as the colored region is intense. This region is approximately not much wider than the interval $(-2\Delta, 2\Delta)$.

guarantees the strong regime), and changing the initial condition and the measurement basis to the corresponding eigenstates of σ_x. This is feasible, as we explored various simulations that supports our hypothesis, e.g. for the strong regime, the Rabi Hamiltonian in eq. (2.5), and measuring in an orthogonal basis different from the eigenstates of the time independent Hamiltonian H_0 (i.e. using instead the eigenstates of H_i or σ_x in this case), it is possible to observe the Landau-Zener phenomenon, therefore it is possible to obtain exactly the same temporal evolution as the one in figure 2.6, or even to realize constructive and destructive interference as shown in figure 2.9, where we have constructive interference (blue plot) for $\Delta = 3$ and a pulse with $A = 40$, $\epsilon_0 = 11$ and $\omega_0 = 5.4$; and destructive interference (orange plot) for $\Delta = 3$ and a pulse with $A = 40$, $\epsilon_0 = 11$ and $\omega_0 = 8.1$. In the case of constructive interference we can observe an inversion population faster than Rabi. It is important to remark that, if the parameters were the same as the ones used in figure 2.7, the temporal evolution would have beeen an exact replica of such figure but this time using the Hamiltonian in (2.5) (usually associated with Rabi), not the Hamiltonian in eq. (2.13). The association of one kind of temporal evolution (Rabi or

Landau-Zener) with one Hamiltonian or the other is a misconception, since it is possible to obtain both kinds of temporal evolutions with any of both Hamiltonians, as long as we pick the right parameter regime and the right measurement basis.

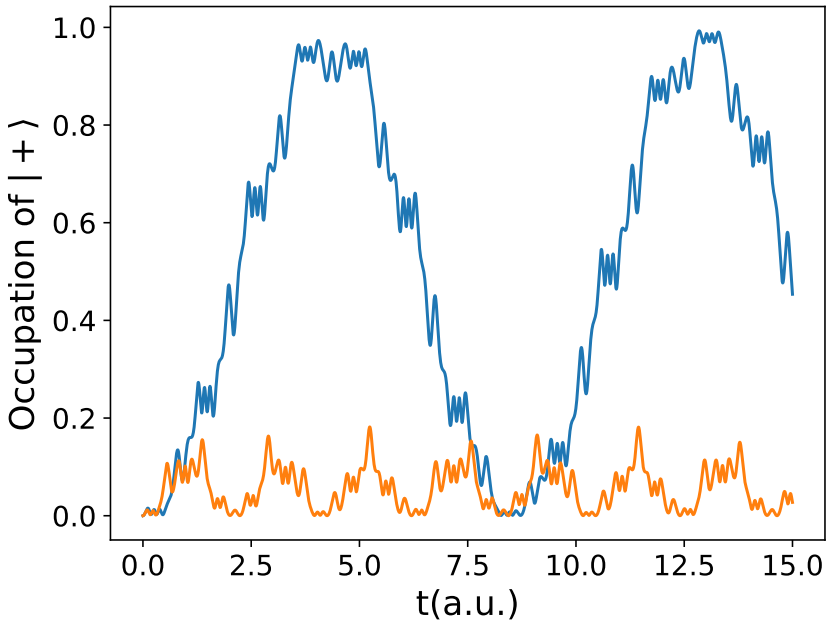

Figure 2.9: Even for the Rabi Hamiltonian in eq. (2.5), with the right parameter regime, and meassuring in a basis different from the eigenstates of the time independent Hamiltonian H_0, it is possible to observe the Landau-Zener phenomenon. In this plot we can observe constructive (blue) and destructive (orange) interference of the Landau-Zener transitions after multiple passage trough the anticrossing region with a sinusoidal pulse defined as $\epsilon(t) = \epsilon_0 + A\sin(\omega_0 t)$, and an initial condition of $|\psi(0)\rangle = |-\rangle$. Parameters: $\Delta = 3$ and a pulse with $A = 40$, $\epsilon_0 = 11$, for both plots and $\omega_0 = 5.4$ for constructive and $\omega_0 = 8.1$ for destructive interference. Temporal evolutions represented in the Sx basis (all parameters are adimensional).

In order to emphasize the importance of choosing the right measurement basis, let us see what happens e.g. for two temporal evolutions with the same parameters in the strong regime, using the Rabi Hamiltonian of eq. (2.5) and the same initial condition $|\psi(0)\rangle = |0\rangle$, but with different measurement basis. These temporal evolutions are plotted in figure 2.10. We can see that the choosing of different measurement basis can lead to temporal evolutions, which according to our analysis is in the right regime to observe the Landau-Zener phenomenon, only the figure 2.10 a) resemblance such dynamics looking like the composition of various individual passages (like the one in 2.6) throuhg the anticrossing. On the other hand, for the evolution in figure 2.10 b), although numerically correct, it is not clear what is the physics behind such strong oscillations and its familiarity with the Landau-Zener dynamics.

Another point to remark comes from the fact that the initial condition does not determine the observation of one phenomenon or the other. Since, as mentioned before, it

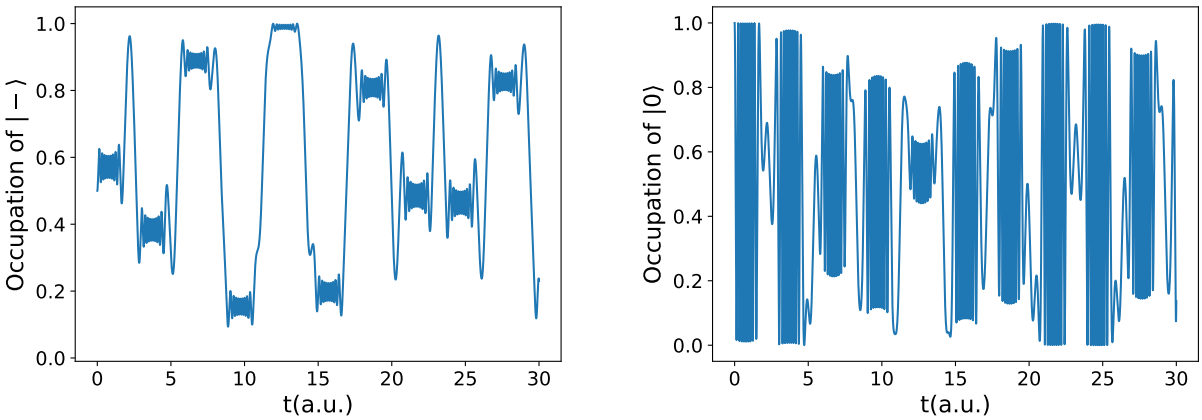

(a) Using the eigenstates of σ_x as the measuring basis. (b) With the eigenstates of σ_z as the measuring basis.

Figure 2.10: Temporal evolutions with the same parameters in the strong regime (where Landau-Zener is manifested), using the Rabi Hamiltonian of eq. 2.5 and the same initial condition $|\psi(0)\rangle = |0\rangle$, but with different measurement basis provided by a rotation of the Rabi Hamiltonian. Both with the same parameters corresponding to a LZ dynamics: $\Delta = 3$, $\omega = 2.1$, $\epsilon_0 = 20$ and $A = 25$ (all parameters are adimensional).

only changes the starting point. This can be seen in figure 2.10 a), where the initial condition is $|\psi(0)\rangle = |0\rangle$, which does not belong to the eigenstates of the measuring basis σ_x. Thus whether starting with an initial condition in its eigenstates $|+\rangle$ and $|-\rangle$ or in a superposed stated, is not primordial to observe Landau-Zener nor Rabi.

In summary, we can conclude that for the two-level system we can have two really different dynamics, but such difference in both phenomena does not come from the distinct Hamiltonians, but rather from the regime of parameters which is really a physical (not mathematical) factor. And the observation of both phenomena depends on the choice of the measuring basis related to the time independent (for Rabi oscillations) or time-dependent (for Landau-Zener) matrix factors of both Hamiltonians.

2.5 One qubit quantum gates

If we consider an arbitrary qubit represented e.g. in the eigenstates of S_z, with components a and b as the state $|\psi\rangle$ of equation (2.2), then, as mentioned in the first section, it is possible represent any such state in the surface of the Bloch sphere. In quantum computing, a unitary operator acting on a single qubit is called 1-qubit quantum gate. A 1-qubit quantum gate can be thought as a rotation in the Bloch sphere, from the initial state $|\psi\rangle$ to a final state $U|\psi\rangle$. A general unitary matrix is given by

$$U = \begin{bmatrix} \alpha & \beta \\ -e^{i\phi}\beta^* & e^{i\phi}\alpha^* \end{bmatrix}, \quad \text{with } |\alpha|^2 + |\beta|^2 = 1, \tag{2.23}$$

and its transformation is depicted in figure 2.11. Since unitary operators preserve the norm of the states, i.e. $||\psi\rangle|^2 = |U|\psi\rangle|^2 = 1$, this preservation and the definition of unitarity $UU^\dagger = \boldsymbol{I}$ implies that these operators are reversible. Physically, this is possible if the unitary transformation describes the evolution of the state in a closed system.

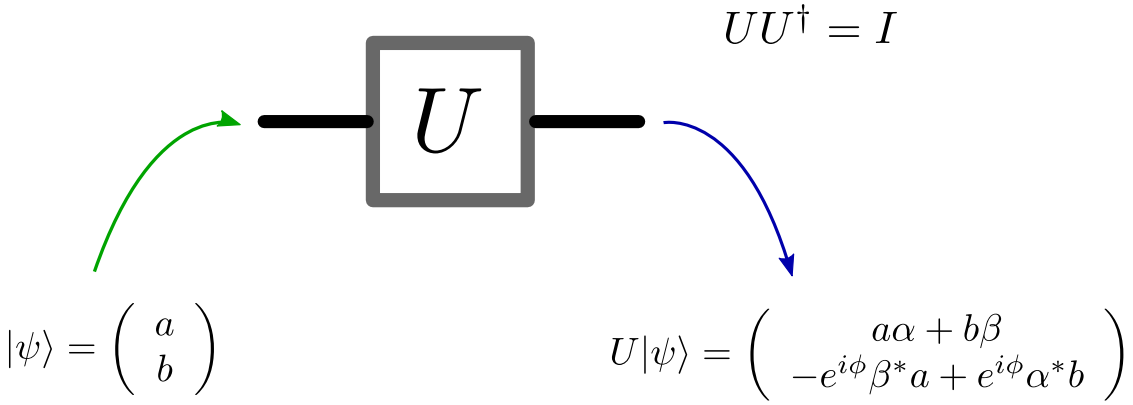

Figure 2.11: Transformation of an arbitrary state $|\psi\rangle$ by a general 1-qubit gate. The box corresponds to the representation of the one-qubit gate in the quantum circuit model.

One-qubit quantum gates are represented here in the graphical representation known as quantum circuit model, sketched by the box of figure 2.11. Attached to the box, we have a left line which leads the input state $|\psi\rangle$ to the gate (the time direction goes from left to right) and a right line which connect the gate with the new transformed output state $U|\psi\rangle$. Some important gates of this kind are illustrated in figure 2.12. The Hadamard gate that corresponds to a 180 degree rotation around the diagonal X+Z axis of the Bloch sphere, and also coincides with the Fourier transform on the group with two elements (binary bits). The Phase shift R_ϕ is a rotation around the Z-axis of the Bloch sphere by ϕ radians.

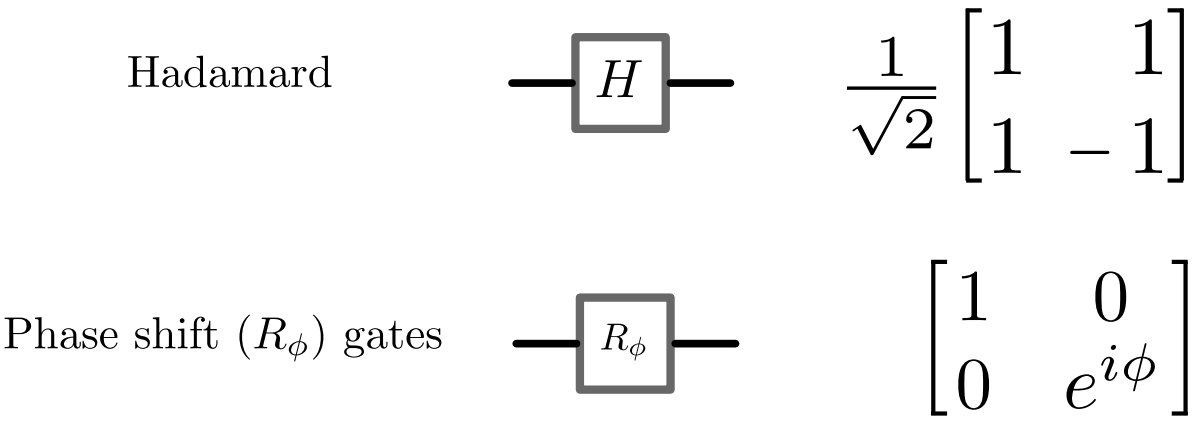

Figure 2.12: Hadamard and Phase shift gates.

Other relevant 1-qubit gates are the Pauli gates, depicted in figure 2.13, with transformations on an arbitrary qubit $|\psi\rangle = a|0\rangle + b|1\rangle$, such as:

$$X\begin{pmatrix} a \\ b \end{pmatrix} = \begin{pmatrix} b \\ a \end{pmatrix}, \quad Y\begin{pmatrix} a \\ b \end{pmatrix} = \begin{pmatrix} -ib \\ ia \end{pmatrix}, \quad Z\begin{pmatrix} a \\ b \end{pmatrix} = \begin{pmatrix} a \\ -b \end{pmatrix}. \tag{2.24}$$

The X gate swaps the canonical basis of S_z on the 1-qubit space; the Y gate also swaps the canonical basis but with a change of phase; and the Z gate changes the phase of the canonical vector basis.

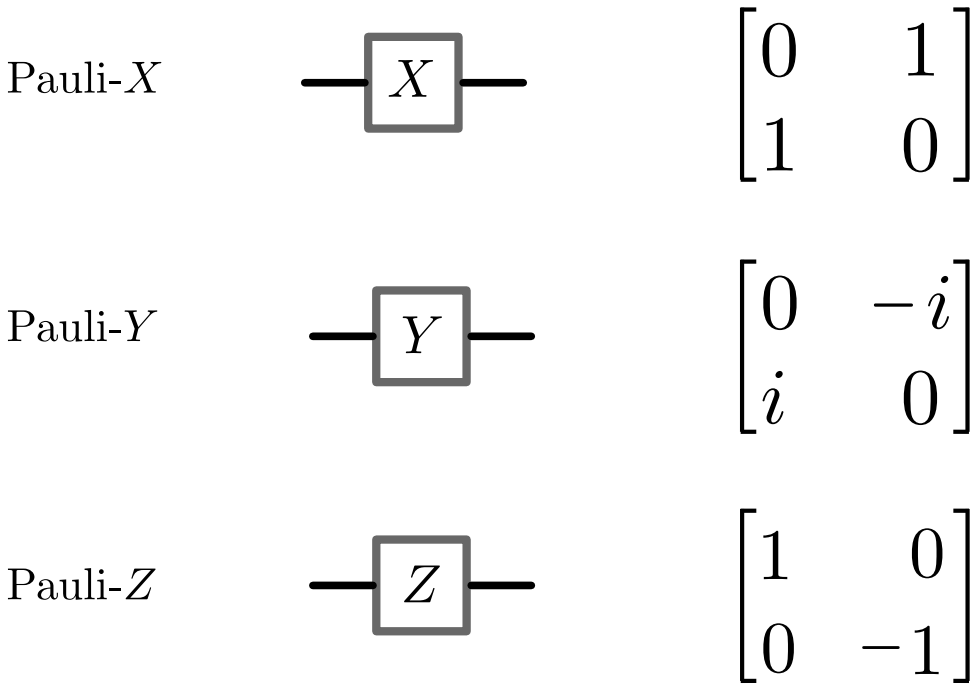

Figure 2.13: Pauli gates.

Quantum gates transform the components of a given input state into an output state, in practice this transformation is realized via a temporal evolutions. Rabi leads to population inversions (which it is equivalent to take an state from one pole to its opposite in the Bloch sphere), and Landau-Zener can lead to mixed state. On the other hand, as seen in this section, most quantum gates have complex outputs with phases, and a generic quantum gate must be able to take a determined initial state to any point in the surface of the Bloch sphere. How a temporal evolution can be designed in order to connect the input state with the output specified by a quantum gate is the topic of the next chapter.

Chapter 3

Optimal quantum control

A reliable control over physical systems is essential for science and engineering. Therefore, the efforts to find robust schemes that can achieve high precision at measurement and manipulation will be always relevant in a technological society. The principal objective of control theory is to find a method to transform a system in order to attain a desired behavior from it. This is usually done by interacting with the system in a controlled way and employing their internal mechanisms to manipulate externally their accessible physical variables.

The challenge to manipulate quantum systems is increasingly relevant to harness the advantage offered by quantum phenomena. The methods offered by quantum control theory have shown to be important tools to approach such challenge. In this chapter we review the theory of quantum control, its origins, their different approaches and current applications. In particular, we will focus on the strategies of quantum optimal control theory (QOCT) and we discuss its advantages and limitations with respect to other strategies of quantum control. Then, we focus on a particular method of QOCT that we used to optimize the driving fields to implement quantum gates with high fidelity. The steps necessary to create these quantum gates are also specified at the end of this chapter.

3.1 Control at the quantum level

Despite the control theory was originally thought to solve classical problems, the advances of molecular and atomic physics and the emerging field of quantum optics provided the first experimental situations where manipulation at the nanoscale was required. This was the case in the 1960s with the initial attempts to use the first lasers as a mean to induce chemical reactions like the selective breaking of bonds in molecules [69]. At first, it was though to be a simple task since the laser could excite an specific frequency mode and the transfer of enough energy could generate a selective bond breakage. However, if the energy is deposited in a single mode, then such energy is dissipated due to redistributions in the other intramolecular vibrational modes and often ends up in the breaking

of other weakest bonds. It was only until the late 1980s that this problem was solved by Brumer and Shapiro [70], who proposed a scheme involving the application of two simultaneous lasers, and the control over their relative phases and amplitudes. Later on, it was necessary additional advances, like femtosecond lasers and an improvement of the pulse shaping capabilities in lasers (since these optimized pulse were not possible to be generated experimentally at that time), so that it was not until the year of 1998 when the first experimental realization of molecular photodissociation was achieved [71]. About the same time when the solution to the photodissociation problem was proposed, other manipulation schemes emerged in different problems of atomic physics and quantum optics for the combined action of two lasers, which are used to induce population inversions between the states, such as the STIRAP (stimulated Raman adiabatic passage) [72], wave-packet interferometry [73], among others. Despite initially these techniques were thought to be fundamentally different, the mechanism underneath these control schemes is the quantum interference between the fields induced by the lasers. Currently these techniques are classified as schemes of coherent control. These are simple schemes that involve the control of a single parameter, like the phase (or the time delay between two lasers), which can be suitable for relatively simple systems (i.e. for physical dynamics with few degrees of freedom). They are still relevant in current studies or implementations of the dynamical evolution of molecular physics, like the opposite problem of breaking bonds in molecules i.e. the problem of ultracold molecular photoassociation with lasers [74, 75, 76, 77]. Other coherence control schemes are also important, like the STIRAP which is still used in quantum optics [78], solid state qubits [79], population transfer in Bose-Einstein condensates [80], or quantum gates [81, 82].

However, for more complex problems like some quantum information implementations in NMR, which requires the manipulation of spin ensembles (with tens or hundreds of nuclei), demanding the control over a higher number of parameters with a greater independence between them, it is required the implementation of more versatile methods.

3.1.1 Quantum optimal control theory

At the end of the 1980s, Rabitz and others [83]-[87] proposed the tailoring of control fields in order to induce the evolution from an initial predetermined state to a prescribed target state with a required accuracy. This idea constitutes the fundamental strategy of most of the quantum optimal control theory (QOCT) methods. The first simulations of this foundational papers used tailored fields via Lagrange multipliers, and such optimized fields [85] replicated the results obtained with the previous less complex control schemes [70]. Also, other optimized fields via QOCT were applied to manipulate molecular states for photodissociation, selective excitation of vibrational or rotational modes as can be seen in the early review of Ref. [88].

Strenghts and limitations

The strength of these kind of optimizing methods comes from the fact that in a physical system, for which the dynamics is lead by various phenomena and constrains, an optimized pulse offers the possibility to exploit dynamical shortcuts, providing faster and more precise temporal evolutions. These shortcuts are difficult or impossible to be forecasted by analytical methods, since the tailoring of the optimal field is realized by favoring, in every iteration, those temporal evolutions where the interplay between the pulse and the different interactions cooperate to lead the system to final states closer to the target state at the end of every iteration. For example, in a multivariable system, QOCT can help to obtain an interference pattern susceptible to multiple factors, for which the net contributions are challenging or impractical to be solved analytically in terms of the effects of the individual interactions. This was explored by the first time in Ref. [83], where the calculation of the optimal control fields shown that the amplitudes of the involved vibrational modes of a laser-driven molecule could interfere constructively in a given bond. Of course, the versatility offered by the optimized fields comes at the cost of pulses with more complex profiles in the power spectrum and amplitude modulations (for which Fourier series can help to reconstruct these numerical pulses). That can be challenging for experimental implementations and depends on the stage of ultrashort pulse technology.

Another positive feature is that the optimized pulses are not unique, i.e. there are different fields (like a different combination of shortcuts) that can lead the initial states to a desired result, and this allows to pick between different solutions that can be more suitable to the experimental implementations. This is useful for situations where physical constrains must be included to the control field.

On the other hand, there are some limitations for realistic applications of the optimized pulses via QOCT, since for most of the cases the mathematical representation is not exact, and it its difficult to describe all the interactions involved in the dynamics of a physical system. This is particularly problematic for open quantum systems where the physical system interacts with a high number of degrees of freedom due to the environment interaction; and the theoretical approach is based on approximated models of decoherence. Although there are QOCT formulations [89] and implementations [90] for problems dealing with decoherence, as mentioned in [69] "it is essential to know the details of the system-environment interaction". For this reason, it is more practical the use of QOCT as an approach to grasp an insight of new quantum phenomena in relatively simple models. For example, in situations where the controlled subsystem has characteristic frequencies far away from other energy levels that could generate undesired transitions, and thus the relevant physics happens in this rather isolated subset of levels. This situation can be found in atomic systems or in quantum dots, where the relative isolation of a subset of

discrete levels from the other levels has associated a low probability of any transition to levels outside the subset of interest. Thus, preventing any leakage of the state population and easing the precise manipulation with the control methods. Another situation where QOCT constitutes a reliable tool takes place when the decoherence time is larger than the manipulation and response times of a physical system. This is a relevant feature in quantum information processing, since it allows a robust control of the states where the information is encoded; such is the case of the platforms studied in chapters 4 and 5. Yet in the presence of decoherence, QOCT methods can be coupled to a bath to emulate the effects of the interaction with environment and still can be useful as a first step to evaluate the feasibility and to identify robust control mechanisms, since basic features of the dynamics can be manifested even in approximate models.

Nevertheless, most of the realistic physical experiments must deal with decoherence problems and, in such cases, other control strategies can be more suitable, like the adaptative feedback control (AFC) or the real-time feedback control (RTFC). Although, some of them can be more or less noisy and introduce more decoherence effects, e.g. in the RTFC strategy due to required measurements (inevitably needed to acquire a feedback and lead the temporal evolution of the system). Therefore, the implementation of one strategy or the other actually requires a careful pondering of the advantages and limitations that every strategy can offer for a determined physical problem. Since these strategies end up being complementary, it is important to think how they can contribute to achieve the ultimate goal which is, its experimental realization.

State of the art

Although QOCT was initially proposed for molecular manipulation, in the last decades numerical experiments on a variety of platforms and protocols have been simulated, and its application has proven to be a useful tool to assest the feasibility of experimental realizations in various platforms for quantum information processing for diverse platforms like quantum dots [91, 92], superconducting qubits [120], and electronic transport in semiconductors or in Bose-Einstein condensates [93, 94, 95, 96]. Also important are the contributions that QOCT has made to the theoretical study of quantum dynamics [61], for a relevant concept in both fields, that is the quantum speed limit (QSL) [62] (a quantity related with the minimum time required to achieve a transformation from an initial state to a final desired state). In Ref. [64], it was found that the minimum time to perform a transformation, for the Krotov algorithm (a QOCT method see ref. [65]) coincides with the QSL. Their tests were made in the Landau-Zener model and in the transfer of information along a chain of coupled spins with Heisenberg interactions; and these relation were also extended to open quantum systems in Ref. [66]. Proving that the QOCT methods can be reliable schemes to find optimal fields that could realize experimental implementations

with efficiencies close or equal to the QSL. Besides, such study established the QSL as an appropriated standard to define optimality in the proper theory of quantum control [61].

Furthermore, the QOCT has been used to simulate the efficient charge of a quantum battery [67], with a time close to the QSL bounds that were determined in Ref. [68]. Being the quantum battery a relevant element in the field of quantum thermodynamics, these studies open the possibility to approach other implementations via QOCT strategies in this field of research, where a figure of merit is the efficiency of cycles.

Currently, most of the studies of QOCT are numerical explorations, and there are many proposals for experimental realizations, but there is a delay in these experimental implementations. The main factor that have delayed the implementation of these proposals is the technological limitation in the generation of experimental ultrashort pulses, which duration must be comparable to the characteristic dynamical times of the manipulated physical systems (which are different, depending on what platform is used). This yields three shortcomings. First, in order to exploit the internal mechanisms that interact with the external pulse, the pulse duration must be at the same time scale of the physical response time of the system. Second, the bandwidth of the pulse depends of the pulse duration, the shorter its time, the wider the frequency bandwidth. Third, the technological pulse shaping capabilities must be able to operate at such scale time in order to effectively apply the amplitude modulations and the set of frequencies involved in an optimized pulse [97]. Also, platforms with decoherence can limitate even more the assistance of QOCT for experimental realizations, as an optimal pulse tailored from an imprecise model reduce its effectiveness in experimental implementations. Due in part to the aforementioned limitations, specially in open quantum systems, experimental realizations of the numerical explorations done via QOCT methods are (at the moment) not as diverse, even though there are a lot of proposals for different problems in various platforms.

However, as the ultrashort pulse technology and the shaping capabilities are improved, more physical platforms become available to test these numerical proposals. A good example can be seen in the platform of NMR, which has provided a lot of experimental implementations due to the fact that the characteristic time of this platform is of the order of nanoseconds, therefore the technology available to test the experimental implementations in this platform was available almost two decades ago. This explain why NMR became one of the first testbeds for developing control methods for applications in quantum information, where the first quantum algorithms were implemented [6, 7]. Currently, the use of optimized pulses via the GRAPE method [98] is common in the experimental realizations of quantum information in the NMR platform, like quantum logic gate implementations, generation of long life quantum states, fault-tolerant computation [99, 101, 102, 100], etc.

Even so, experimental realizations have been implemented in other platforms, like superconducting circuits or spin-based quantum computing in nitrogen vacancies, among

others [120, 104, 103, 105]. The level of experimental control achieved in the NMR platform, thanks to the QOCT and the coherent control schemes, and the present developments of ultrashort pulse technology[1] reinforce the promise of new improvements in the manipulation of other platforms worthy of study, e. g. semiconductor based platforms [106, 107, 108, 109, 110], in which the dynamics can be faster than atomic or molecular systems.

3.2 TBQCP method

As already mentioned, the basic goal of optimal control consists of finding time-dependent control fields that drives an initial state $|\psi(0)\rangle$ to maximize the average value of an observable at the end of the time evolution $\langle O(T)\rangle$. In this study, we implement the numerical method TBQCP [126], which is an iterative monotonic method able to find an optimal field $E_{opt}(t)$ that maximizes the expectation value of a physical observable $\langle O(t)\rangle$ at the final time T. This method starts with the definition of the boundary conditions, the initial state $|\psi(0)\rangle$ and the desired physical observable $\langle O(T)\rangle$, associated with $|\psi_i(0)\rangle$ and $|\psi_{target}\rangle$ respectively in figure 3.1. The physical observable is evolved backwards (from the final time T to the initial time $t = 0$) through the following equation

$$i\hbar\frac{\partial O^{(n)}(t)}{\partial t} = \left[O^{(n)}(t),\, H_0 - \mu E^{(n)}(t)\right],\; O(T) \to O(0), \tag{3.1}$$

where H_0 is the time-independent Hamiltonian of the system, μ is the dipole operator, and $E^{(n)}(t)$ is the field in the nth iteration. The initial state $|\psi(0)\rangle$ is evolved forward with the time-dependent Schrödinger equation

$$i\hbar\frac{\partial|\psi^{(n+1)}(t)\rangle}{\partial t} = \left(H_0 - \mu E^{(n+1)}(t)\right)|\psi^{(n+1)}(t)\rangle, \tag{3.2}$$

where $E^{(n+1)}(t)$ is the (n+1)th iteration field, which is calculated through the following expression

$$E^{(n+1)}(t) = E^{(n)}(t) + s(t)\eta f_{\mu}^{(n+1)}(t). \tag{3.3}$$

In Eq. (3.3), η is a positive constant (to be calibrated depending on the performance of the code), $s(t)$ is a positive enveloping function[2] and the field correction is written as

$$f_{\mu}^{(n+1)}(t) = -\frac{2}{\hbar}\mathrm{Im}\left\{\langle\psi^{(n+1)}(t)|O^{(n)}(t)\mu|\psi^{(n+1)}(t)\rangle\right\}. \tag{3.4}$$

Equations (3.1-3.2) are solved in a self-consistent way, starting with the trial field $E^{(0)}(t)$ and the control field is tailored in every iteration with equations (3.3-3.4), such

[1] At the moment the shortest pulse are of the order of femtoseconds.

[2] which is smooth and variates going to zero at the initial and final pulse time, in order to avoid any transient effects in the implementation.

that the expected value of the observable at the final time $\langle O(T)\rangle = \langle\psi(T)|O(T)|\psi(T)\rangle$ increases monotonically, see more details in Ref. [126]. Particularly, if one is interested in maximizing the evolution to an specific target state $|\psi_{target}\rangle$, the operator that descbribes the observable becomes the projector onto this state $O(T) = |\psi_{target}\rangle\langle\psi_{target}|$. A detailed deduction of this equations and the physics behind the TBQCP method can be seen in appendix B.

The effect of the TBQCP method on the temporal evolutions is depicted in figure 3.1, which starts at $|\psi_i(0)\rangle$ and $|\psi_{target}\rangle$ for the forward and backward evolutions, respectively. At the first iteration, the starting and final states of both trajectories are different. But with every iteration, corrections in the control field are implemented, such that these two evolutions (forward and backward) go from dissimilar evolution paths to a more common evolution, where the starting state of one trajectory is where the other trajectory ends and viceversa.

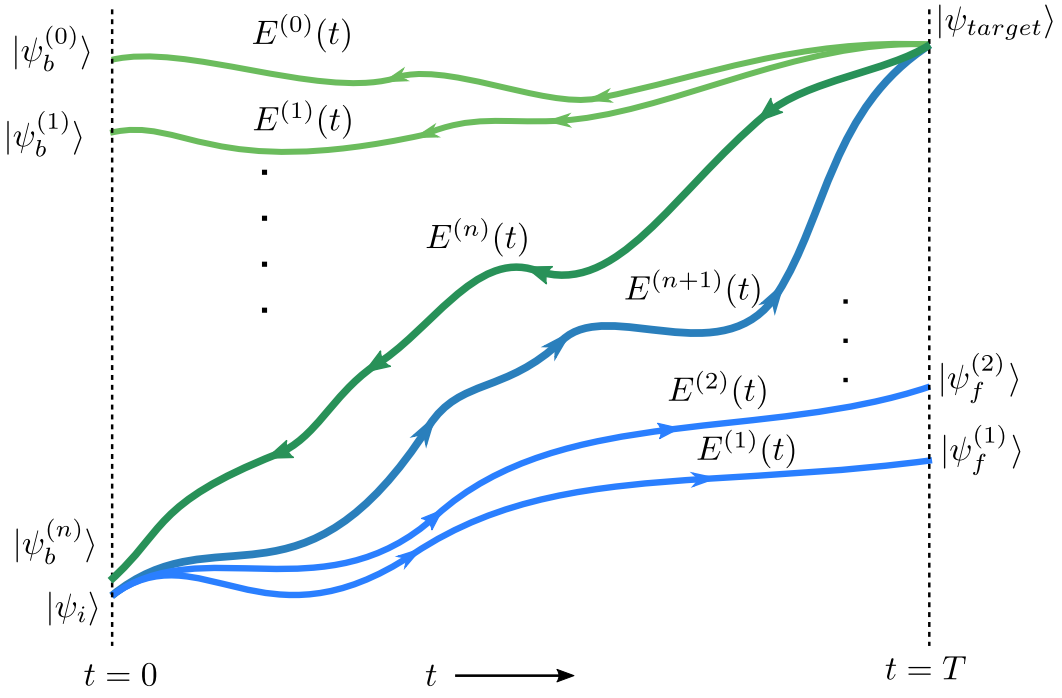

Figure 3.1: The successive improvements of the temporal evolutions via the TBQCP method, which tailors an optimal control field that leads from an initial state $|\psi_i(0)\rangle$ to a final one close or equal to a target state $|\psi_f^{n+1}(T)\rangle \approx |\psi_{target}\rangle$.

3.3 Implementation of Quantum Gates

Quantum gates are the quantum analogue of logic gates in classical computers. Such gates are reversible in time and are represented by unitary matrices $\mathcal{U}$. Since the implementation of a quantum gate implies a transformation on any state, as described in eq. (2.23), then it requires the optimization of a control field that induce the desired evolution of multiple

states. The optimal quantum control scheme can be employed to implement quantum gates [127, 128]. Such implementation can be performed by finding the optimal field that steers a set of initial k-states $|\psi_k(0)\rangle$ to a specific set of final target k-states $|\psi_k^{target}\rangle$. The set of initial k-states can be given by the basis eigenvectors of a chosen operator $\{|j\rangle\}$ where $j = 1, \ldots, k$ plus the initial superposed state $\sum_{j=1}^{k} |j\rangle/\sqrt{k}$, which avoids errors due to undesirable relative phases [127, 128]. The set of final target k-states $|\psi_k^{target}\rangle$ is given by $\{\mathcal{U}|j\rangle, \mathcal{U}\sum_{j=1}^{k} |j\rangle/\sqrt{k}\}$.

In this study, we define the mean fidelity to characterize the quantum gate efficiency. For a closed system, the fidelity is defined as $\mathcal{F} = |\langle\psi(T)|\psi_{target}\rangle|^2$, where $|\psi(T)\rangle$ is the time evolved state and $|\psi_{target}\rangle$ is the desired state under the action of the quantum gate. The mean fidelity is given by the following equation

$$\bar{\mathcal{F}} = \frac{1}{N+1} \sum_{j=1}^{N+1} |\langle\psi_k^{target}|\psi_k(T)\rangle|^2, \tag{3.5}$$

where $|\psi_k(T)\rangle$ are the time evolved k-states from the initial k-states $|\psi_k(0)\rangle$.

3.3.1 Quantum gates in the TBQCP method

The implementation of a quantum gate requires the optimization of a control field that induce the desired evolution of multiple states, which transform the set of initial conditions $|\psi_k(0)\rangle$, into the set of final target k-states $|\psi_k^{target}\rangle$, with a required precision. Thus, an small modification must be implemented in eq. 3.4, to correct the reference field in every iteration. In a multitarget gate, the correction term in eq. 3.4 is calculated separately in the evolution of every state (which is performed exactly the same, as explained before for a single target), and then the individual contributions are added to correct the field of the next iteration. Therefore eq. (3.3) must be modified and takes the new form

$$E^{(n+1)}(t) = E^{(n)}(t) + s(t)\eta \sum_{k} f_{\mu_k}^{(n+1)}(t), \tag{3.6}$$

where $f_{\mu_k}^{(n+1)}(t)$ corresponds to the correction of the k-state, and the new reference field $E^{(n+1)}(t)$, is effectively corrected with contributions of every propagated state, at every time t in the simulation.

Chapter 4

One-qubit in Nanowire Quantum Dots

After reviewing the dynamics of a qubit and the theory of quantum optimal control, we are ready to simulate its implementation in some physical platforms. In this chapter, we do that for the system of nanowire quantum dots. At the beginning of this chapter, we study the physics of this platform and the interactions with external electromagnetic fields. Then, we analyze the level structures and temporal evolutions for two setups of this system. The first, consisting of a single quantum dot and the second of two quantum dots in the nanowire. Then, we study the temporal evolutions present in each setup of this platform for different regime parameters under harmonic driving field. The evolution basis corresponds to the first four energy levels, and the qubit is encoded in the first two levels. In these temporal evolutions, we identify sets of parameters where the dynamics correspond to those discussed in chapter 2, Rabi or Landau-Zener. For the appropriated parameter sets, these two dynamics constitute a reliable mechanism to achieve population inversions for our qubit with negligible leak to the upper levels. But since we are interested in a higher degree of control, then in the final section we implement more complex task with the aid of the TBQCP method. We explore numerically the feasibility of three quantum gates, and we determine a setup where the efficiency increase in one order of magnitude, with respect to the temporal evolutions provided by the phenomena explored in the previous sections. At the end of the section, we address a problem relevant for the experimental generation of the optimized electrical pulses and quantum metrology. For this reason, we decompose the optimized fields with the Fourier transform and then we reconstruct them with Fourier series, in order to determine how many Fourier coefficients are enough to reconstruct a new pulse that perform the same task of the original optimized fields with a satisfactory precision.

4.1 Nanowire Quantum Dot

Quantum dots are structures that provide three dimensional confinement of few electrons or even a single one. Among various semiconductor devices that satisfy this property,

there are electrostatic quantum dots, where electrical potentials applied through electrical contacts are responsible for confining electrons. Among the different electrostatic quantum dots, a possible realization are the gated nanowires, whose cylindrical geometry offers confinement in the transversal direction of the nanowire, and the electrical potentials confine the electrons in the axial direction. This kind of quantum dots are described by the Hamiltonian

$$H_0 = -\frac{\hbar^2}{2m^*}\nabla^2 + V(y,\, z) + V_w(x), \tag{4.1}$$

where the confinement in the yz plane can be modeled as the harmonic oscillator potential

$$V(y,\, z) = \frac{1}{2}k(y^2 + z^2),$$

where $k = \omega_0^2 m^*$ is analogous to a restorative constant (isotropic in the yz plane), m^* is the electron effective mass and ω_0 is the oscillation frequency. The confinement along the $\hat{x}$ direction is represented by $V_w(x)$, usually described as the potential of one or multiple quantum wells; this confinement is provided by an static electric field applied through the gates of the nanowire, such that the effective potential of the static field corresponds to a one-dimensional square quantum well $V_w(x)$ in the $\hat{x}$ direction.

If we apply variable separation in the time-independent Schrödinger equation associated to the Hamiltonian in eq. (4.1), the solution can be expanded in the following way:

$$\Psi_{n_x,n_y,n_z}(x,\, y,\, z) = \sum_{n_x,n_y,n_z} \frac{X_{n_x}(x)}{\sqrt{\pi}R_0} \exp\left[-\left(\frac{y^2+z^2}{2R_0^2}\right)\right] H_{n_y}(y) H_{n_z}(z). \tag{4.2}$$

This solution is proportional to the Hermite polynomials, with $R_0 = \sqrt{\frac{\hbar}{m^*\omega_0}}$, related to the one of the diameter of the nanowire $R_0 \approx L_y,\, L_z$. Furthermore, for the particular case of $V_w(x)$ describing a one-dimensional quantum well, the solution in the $\hat{x}$ direction, $X_{n_x}(x)$, corresponds to the solution of a finite one-dimensional square quantum well; which has a transcendental solution and can be found in Ref. [49].

For quantum wells the separation between the energy levels is inversely proportional to the dimensions of the system. If we have a width of the quantum well L_x (or the total length of the quantum wells whenever more than one is considered) bigger than the nanowire diameter, see figure 4.1, then we will have a distribution of the energy levels like the one in figure 4.2. In such distribution, the energy levels variate faster for a change in the quantum number n_x associated to the $\hat{x}$ direction, than for changes in the other quantum numbers (n_y and n_Z associated to directions $\hat{y}$ and $\hat{z}$ respectively). If any further interactions to be considered only involve the first energy levels, then the quantum numbers n_y and n_Z can be considered to be frozen in their respective ground states in the temporal evolutions. Thus, the wave function in (4.2) takes the form

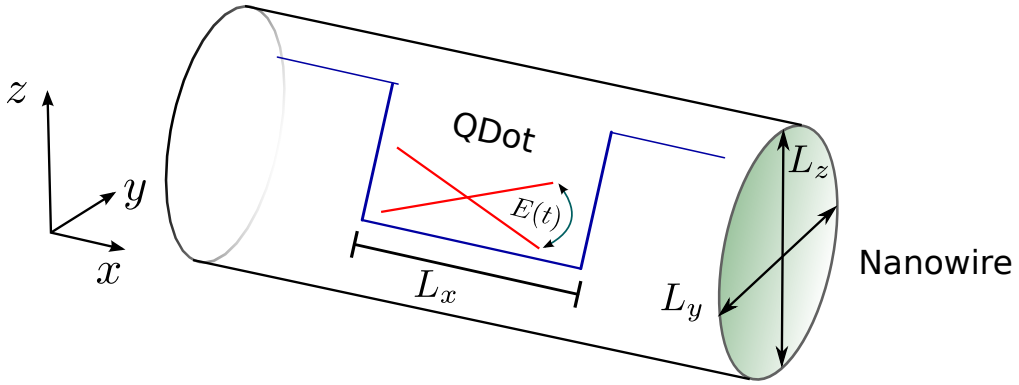

Figure 4.1: Pictorial figure describing a quantum dot in a gated nanowire with $L_x \gg L_y$, L_z. The electrons are confined in the $\hat{x}$ direction by an static electric field and their states are controlled by the action of a local time-dependent electric field (red). Both fields are applied to the quantum dot by electric gates on the nanowire .

$$\Psi_{n_x,1,1}(x,\, y,\, z) = \frac{X_{n_x}(x)}{\sqrt{\pi} R_0} \exp\left[-\left(\frac{y^2+z^2}{2R_0^2}\right)\right]. \tag{4.3}$$

If the physical parameters of the nanowire (strong lateral confinement due to the nanowire diameter) provide such situation, then the motion in the YZ plane is frozen with a Gaussian wavefunction and our energy levels only differ by n_x. In such case, we can simplify our Hamiltonian in (4.1) to a one-dimensional Hamiltonian in terms of the x coordinate. Therefore, the quantum dot can be represented like a one-dimensional finite quantum well as sketched in figure 4.1.

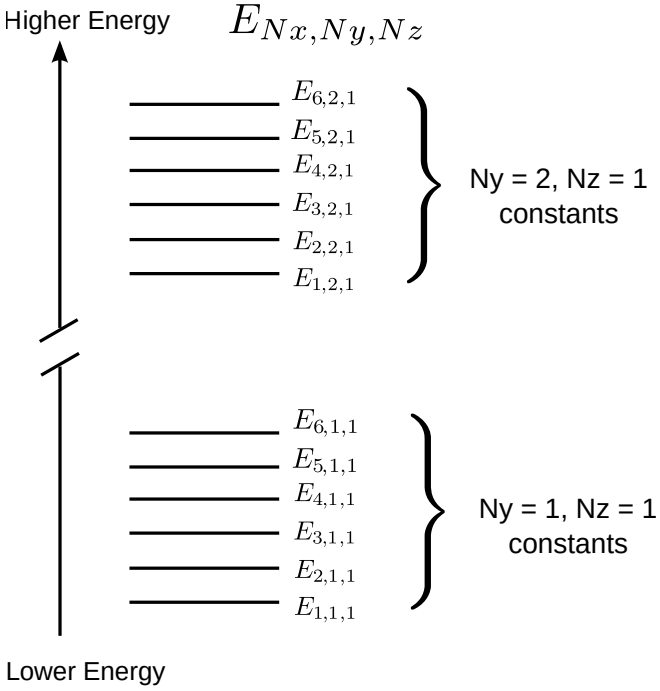

Figure 4.2: Level distribution for a quantum dot with $L_x \gg L_y$, L_z.

Taking in account the one-dimensional approximation, considering the presence of an

static magnetic field in the $\hat{x}$ direction (described by the Zeeman term), and the presence of a constant electric field ε_0 applied in the $\hat{x}$ direction (described by the dipole operator by the term $e\varepsilon_0 x$). Then, the time-independent Hamiltonian of our system is

$$H_0 = -\frac{\hbar^2}{2m^*}\frac{d^2}{dx^2} + V_w(x) + e\varepsilon_0 x + \frac{1}{2}g\mu_B B_x \sigma_x. \tag{4.4}$$

In order to manipulate the electronic states associated to the spin, we need to include interactions involving such states. With such objective, we can employ the results from [112], where it was found that the combined action of an static magnetic field, an electric oscillating field, and spin-orbit interaction allows the control of the electronic spin by an effective time dependent magnetic field $h(t)$. In our case, we will consider the Rashba interaction which is given by:

$$H_{SO} = \frac{\alpha}{\hbar}\left(p_y\sigma_x - p_x\sigma_y\right). \tag{4.5}$$

For small values of B_x and the strong confinement of the nanowire in the transversal direction, we can ignore any orbital effects of the magnetic field Ref. [113] and the canonical momentum $\vec{P}$ can be approximated as [112]

$$\vec{P} \sim -i\hbar\nabla.$$

In order to manipulate the system, we apply an external oscillating electric field described by

$$\varepsilon(t) = A\sin(\omega t), \tag{4.6}$$

where A is the amplitude. The interaction of this oscillating electric field with the system is mediated by the dipole operator, thus its contribution to the Hamiltonian of the system is described by the term $V(x,\, t) = e\varepsilon_p x + exA\sin(\omega t)$.

Considering the time-independent Hamiltonian H_0, the spin-orbit interaction of eq. (4.5), the action of an static field in the $\hat{x}$ direction as in eq. (4.4), and the oscillating electric field in eq. (4.6), the complete Hamiltonian is

$$H = -\frac{\hbar^2}{2m^*}\frac{d^2}{dx^2} + V_w(x) + \frac{1}{2}g\mu_B B_x\sigma_x + H_{SO} + e\varepsilon_0 x + V(x,\, t). \tag{4.7}$$

Thanks to the dipole, magnetic field, and spin orbit interactions we are now able to manipulate not only the electronic states associated to the quantum number n_x, but also the spin. It was shown in Ref. [112] that, an oscillating electric field induces periodic oscillations in the position of the charge distribution. This periodic movement of the charge distribution generates an oscillating effective magnetic field that interacs with the spin via the spin-orbit coupling H_{SO} [114]. In turn it produces spin oscillations driven with the effective field H_{eff} generated in our case by the electric-dipole spin resonance

(EDSR). This effective field can be estimated using perturbation theory [112], which yields the following formula for the effective time dependent magnetic field H_{eff}

$$H_{eff} = \frac{1}{2}\vec{h}(t).\vec{\sigma},$$

with our parameters:

$$\vec{h}(t) = 2g\mu_B B_x \frac{e\varepsilon(t)}{m\omega_{QD}^2}\frac{\alpha m}{\hbar}\hat{z}, \tag{4.8}$$

where ω_{QD} is the quantum dot frequency. From this expression we can see the linear dependence with the magnetic field B, the Rashba constant α and the amplitude of the pulse A. In the case of the well width L, the proportionality relation is $L^4 \backsim \frac{1}{\omega_{QD}^2}$.

As part of a systematic study to characterize this system, we simulated the Rabi oscillations for the different parameters involved in the Hamiltonian of eq. (4.7), variating the parameters corresponding to the magnetic field B, the Rashba constant α, the well width L, and the amplitude of the pulse A; which were plotted against the Rabi frequency of Ω_R respectively in figures 4.3, 4.4, 4.5, and 4.6. In these figures, the green dots correspond to the actual points that were simulated, while the discontinuous lines in black correspond to a linear interpolation over those points, except for figure 4.5, where the scale is logarithmic, and thus the interpolation is exponential.

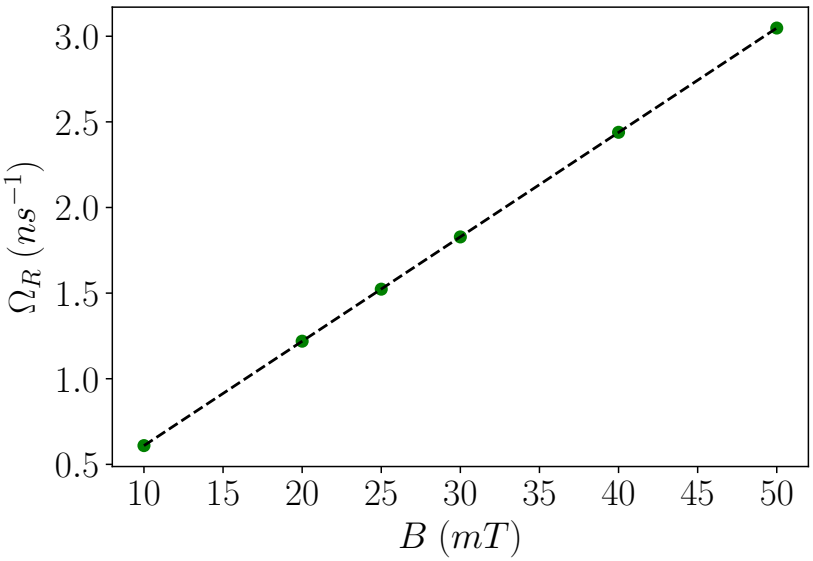

Figure 4.3: Rabi frequency vs the static magnetic field. Green dots represent the simulated temporal evolution and the black line correspond to its linear interpolation. With parameters $\alpha = 50$ meV.nm, $L = 200$ nm, and a pulse with $A = 100$ V/cm.

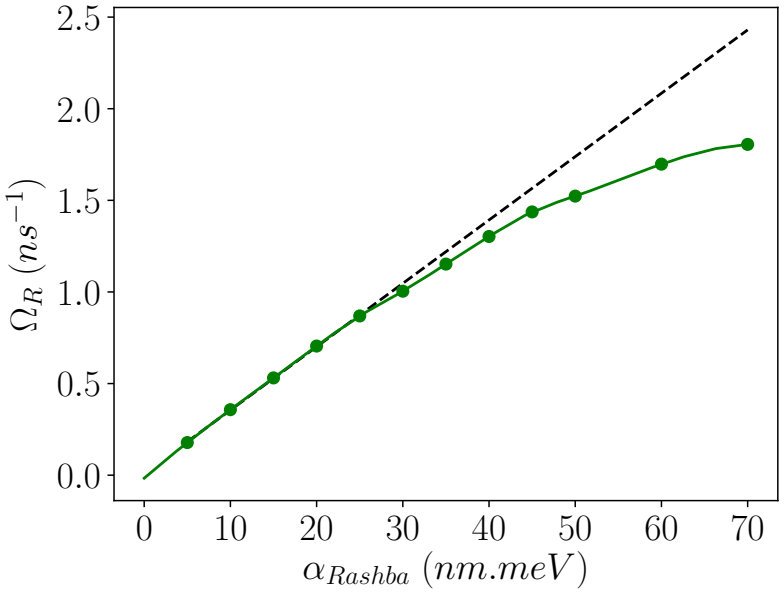

Figure 4.4: Rabi frequency vs the spin-orbit coupling factor. Green dots represent the simulated temporal evolution and the black line correspond to its linear interpolation. With parameters $B = 25$ mT, $L = 200$ nm, and a pulse with $A = 100$ V/cm. The simulated Rabi frequency begins to depart significantly from the simulated values at $\alpha = 50$ meV.nm.

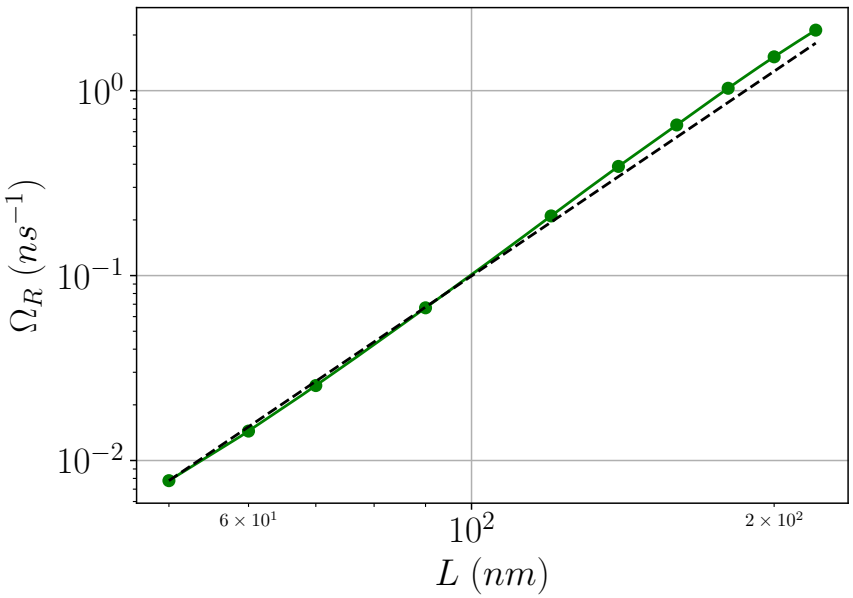

Figure 4.5: Rabi frequency vs the length of the square well. Green dots represent the simulated temporal evolution and the black line correspond to a exponential interpolation. With parameters $B = 25$ mT, $\alpha = 50$ meV.nm, and a pulse with $A = 100$ V/cm.

From the results in figures 4.3, 4.4, 4.5, and 4.6, we can conclude that at least for the values in (or close to) the interpolations (where the perturbation theory is valid), we can

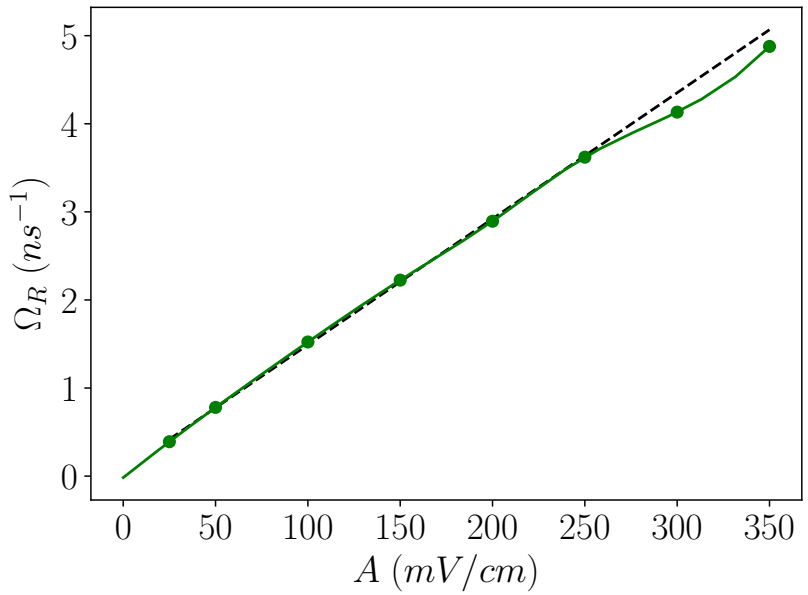

Figure 4.6: Rabi frequency vs the amplitud of the driving field. With parameters $B = 25$ mT, $\alpha = 50$ meV.nm and $L = 200$ nm.

expect a direct relation between the effective field in eq. (4.8) and the oscillations of the spin. Since the simulated points obey the same proportionality relations with the four variated parameters, then such effective field induce Rabi oscillations with a frequency given by

$$\Omega_R = \frac{H_{eff}}{\hbar} \propto BA\alpha L^4.$$

Of course, this relation can not be guaranteed for the values of A, α and L, where the simulated points deviate from the perturbation theory. This happen for the amplitude for values $A > 250$ mV/cm, for the Rashba constant if $\alpha > 40$ nm.meV and for the width of the quantum well when $L \gg 200$ nm.

A gated nanowire can be the host for one or multiple electrostatic quantum dots. Next, we inspect the platforms of one electron in a single and double quantum dots with the objective to test which configuration is more advantageous to be used as a qubit platform.

Both setups are simulated with a set of common parameters corresponding to a nanowire of InSb, which have an effective electron mass of $m^* = 0.014m_0$, magnetic moment of 0.05788 meV/T, and a gyromagnetic factor of $g = -51$. All the temporal evolutions were run and expanded with an evolution base corresponding to the first four eigenstates of the time independent Hamiltonian in equation (4.4). Energy levels superior to the fourth one are at least an order of magnitude higher in both setups, therefore the temporal evolutions are well approximated considering only four energy states.

4.2 One electron in a single QD

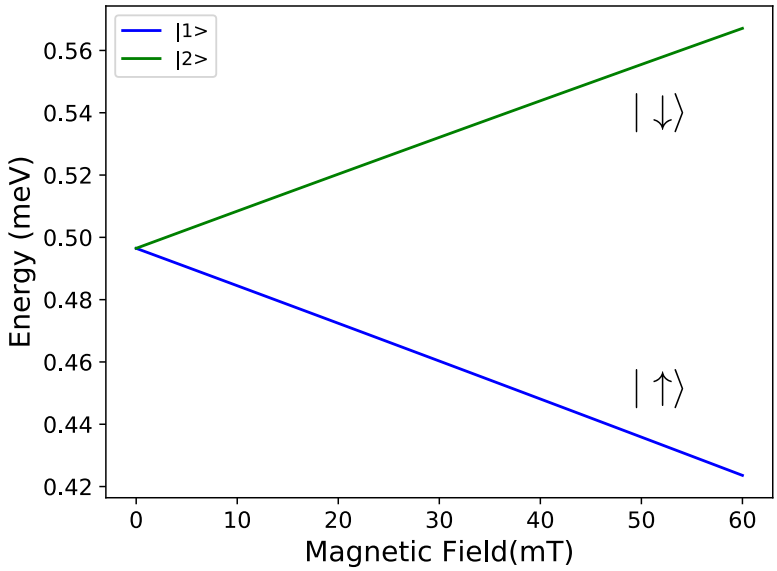

Figure 4.7: Level splitting for the ground state due to the interaction of the spin with an external static magnetic field.

This first setup corresponds to the Hamiltonian of eq. (4.7) with the term $V_w(x)$ describing a finite square well; which parameters were fixed for a wide of 200 nm and a height of 200 meV. To begin the study of this system, we set the electric field bias $\varepsilon_0 = 0$ and the oscillating pulse to $\varepsilon(t) = 0$ (which turns off the time-dependent interactions and the pulse bias ε_p)[1]. Then we discretize the space with the Chebyshev grid method [115] to rewrite the different terms of the Hamiltoninan in eq. (4.7). Furthermore, we numerically diagonalize these Hamiltonian matrix, to obtain the eigenstates and eigenvalues of the time independent Hamiltonian H_0 of the system composed by the eq. in (4.4) and the Spin-orbit interacion in eq. (4.5). This process is repeated for different values of the static magnetic field B_x to calculate the associated energies. Due to the interaction of the spin with this magnetic field, there is a break in the degeneracy of the energy levels, which is illustrated in figure 4.7. The ground state splits in two new energy levels with spin up and down, which separation is described by the Zeeman interaction in eq. (4.7).

Since we are interested in exploiting the spin degree of freedom (via the spin-orbit interaction), we need a non-zero value for the magnetic field in order to differentiate the energy levels associated to the states with spin up and down. For this reason, we set the magnetic field to $B = 25$ mT, and then proceed to study the level structure when variating the electric field bias ε_0 (in an interval for realizable experimental values of this bias). The corresponding level structure is shown in figure 4.8, where we can see

[1]The system bias ε_0 and the pulse bias ε_p can be varied, but they will be relevant in the next setup of two quantum dots in the nanowire.

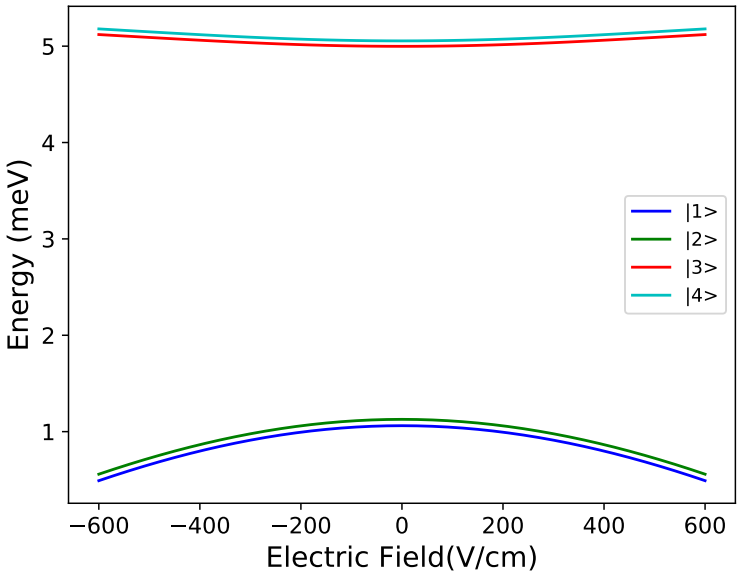

Figure 4.8: Level structure for a single quantum dot with a wide of 200 nm and an static magnetic field of $B = 25$ mT. In this interval that covers high experimental values of the electric field bias ε_0, there is no anticrossing between any energy levels.

that there is no anticrossing between the energy levels. Therefore, for a level structure like the one in figure 2.4, there is no Landau-Zener phenomenon for this setup. In this case, the interchanges of state populations are driven by the Rabi dynamics (which as seen in chapter 2, are usually slower), if we consider a regime of parameters accessible in the experiments. Moreover, it is pointless to apply optimal quantum control in this case, since we did it and the optimized pulses converge to pulses with a power spectrum showing peaks for the resonance frequencies of the system; indicating that the different transitions are only possible through Rabi oscillations, (or a combination of them i.e. via Rabi oscillations between various levels). This limits the possibility to tailor faster temporal evolutions with optimal quantum control.

The temporal evolutions in this setup is lead by the Rabi dynamics. We set the parameters to $A = 100$ V/cm and $\omega = 70.372$ GHz (frequency in the resonance of the first two levels). The temporal evolution under the action of such sinusoidal electric field is illustrated in figure 4.9. We can observe Rabi oscillations with a period of 0.63 ns between the first two levels, and a Rabi frequency of $\Omega_R = 1.59\,\mathrm{ns}^{-1}$. Since no dissipation is considered in this platform, all the temporal evolutions in this chapter were implemented numerically by solving the time dependent Schrödinger in eq. (4.7), with a exponential propagator.

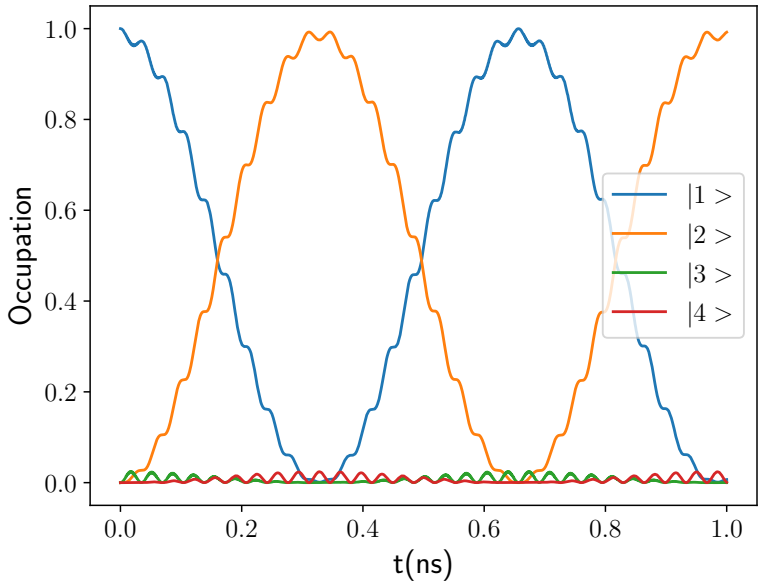

Figure 4.9: Rabi oscillations for the first two levels in a single quantum dot with a Rashba constant of $\alpha = 50$ meV.nm, and for a pulse with $A = 100$ V/cm and $\omega = 70.372$ GHz (in the resonance).

4.3 One electron in a double QD

The second setup corresponds to the Hamiltonian of eq. (4.7) with the term $V_w(x)$ describing a quantum double finite symmetric square well, separated with a barrier; whose parameters are illustrated in figure 4.10, being W_w the width of both quantum wells, W_H the height of the well (characterized by the height of the lateral barriers), B_w the width of both quantum wells, and B_H the height of the inner barrier. For this setup, we did a systematic study where we variated these parameters to see their effects. The heights of the wells W_H only shift the energy levels. For such reason, this parameter was fixed to $W_H = 50$ meV. The width of the quantum wells has the same effect in the energy levels. Nonetheless it was variated. The observed variation of the energy levels with these two parameters is expected, since they modify the confinement of the electron in space. The parameters that changes the level structure more drastically (with changes in the distribution of the anticrossings) are the width of the separation barrier B_w and the height of the barrier B_H, which modifies the coupling and thus the tunneling between the quantum dots. We focused on variations of the barrier width B_w, therefore the height of the barrier was fixed to the values of $B_H = 35$ meV. Similar effects were observed by variating this parameter as well.

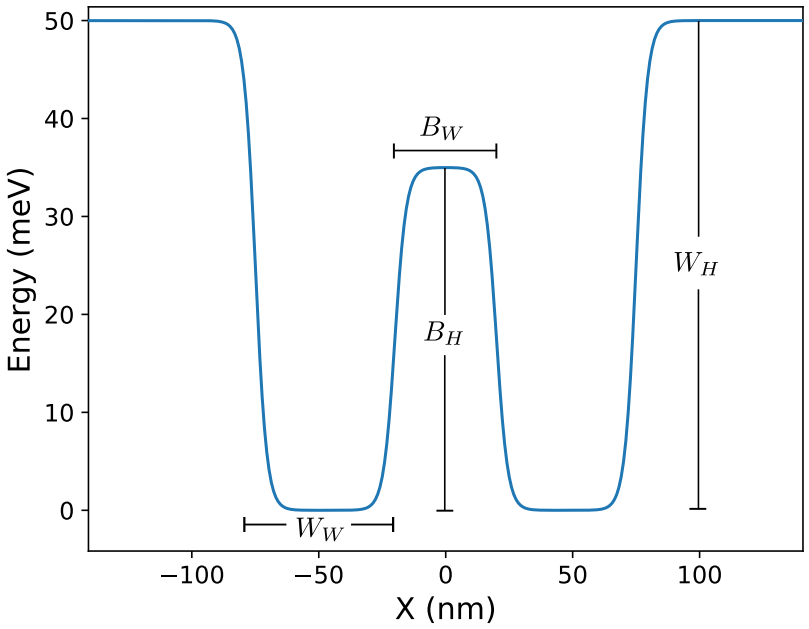

Figure 4.10: Our double quantum dot setup is described by a quantum double finite symmetric square well. In order to simulate a more reallistic potential, the mathematical function that represents it allows soft corners (as depicted in this figure).

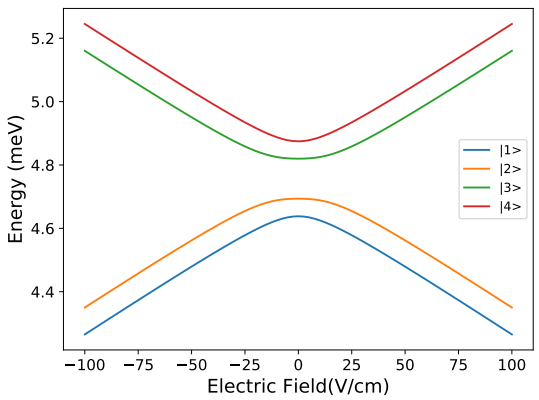

(a) With a barrier width of $B_w = 30$ nm, and quantum finite square wells of width $W_w = 60$ nm each.

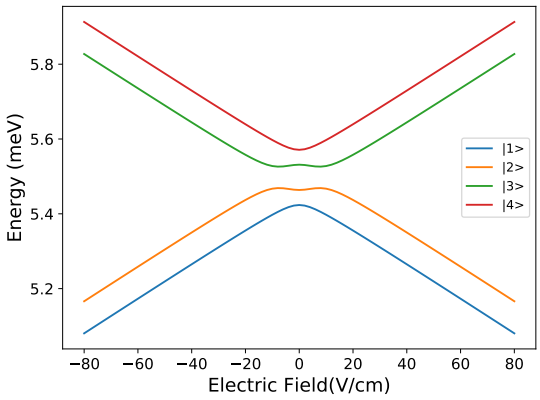

(b) With a barrier width of $B_w = 40$ nm, and quantum finite square wells of width $W_w = 55$ nm each.

Figure 4.11: Level structure for a double quantum dot for different potential barriers separating two finite quantum square wells of width W_w. The level structure suffers a reshaping in the location of the anticrossings. Shifting from one anticrossing as observed in these two figures to the anticrossing distribution depicted in figure 4.12, where four anticrossings involve different pairs of levels independently.

Changes on the distribution of the anticrossings due to the barrier width B_w are illustrated in figures 4.11 and 4.12; where we considered a fixed total width of the system of 150 nm in every arrangement (i.e. summing up the width of both quantum dots and

the barrier $2W_w + B_w = 150$ nm), and varied the width of the barrier and the symmetric quantum wells. In all the following arranges, the Rashba constant was fixed to $\alpha = 50$ meV.nm.

In these level structures we observe an alteration in the distribution of the anticrossings, starting with a large anticrossing (for the four levels) in figure 4.11 a) for a separation barrier of $B_w = 30$ nm, passing to an intermediate distribution for $B_w = 40$ nm in figure 4.11 b), where the second and third level begin to repel each other (as the two inferior and the two upper levels come closer); and finally changing to the anticrossing distribution of figure 4.12, for a separation barrier of $B_w = 70$ nm, where a higher repulsion between the levels and a shift from the former single anticrossing (in figure 4.11 a)) to four anticrossings involving different pairs of energy levels 1-2, 2-3 and 3-4 in figure 4.12.

In order to induce transitions between these energy levels, we apply an external oscillating electric field described by eq. (4.6), uniformly along the whole length of the system (square wells and barrier included). This oscillating field drives the temporal evolutions shown in the rest of this chapter.

4.3.1 Landau-Zener

From the three mentioned level structures the one more appropriate to compare the Rabi and Landau-Zener dynamics (in the present platform involving 4 levels), is the one with separation barrier $B_w = 70$ nm in figure 4.12, since its anticrossings involve only two levels separately. Allowing us to encode a qubit, study its temporal evolutions and then establish as much as possible a comparison with the dynamics of the ideal qubit studied in chapter 2. In figure 4.12 we illustrate the enegy levels and the physical configuration of their states. Also the physical configuration is depicted in such figure, where the occupation and spin of the electron in the DQD changes due to the tunneling and the spin-orbit interactions. Starting for a negative static electric field and a positive static magnetic field with a charge occupation (0, 1) for the ground $|1\rangle$ and first excited state $|2\rangle$ (with spin up and down respectively), and a charge occupation (1, 0) for the levels $|3\rangle$ and $|4\rangle$ (with spin up and down respectively). This physical configuration change for the levels $|2\rangle$ and $|3\rangle$, when the static electric field is still negative but beyond the first anticrossing. This change is due to the static electric field which swaps the occupation and the spin component in the energy level $|2\rangle$ to end up with the occupation (1, 0) and spin up; and swaps the components of the energy level $|3\rangle$ to the occupation (0, 1) and spin down. A second changes occurs when the static electric field becomes positive but before the third anticrossing. In this case the four energy levels undergo a swap in the occupation of the dots. The last change in the physical configuration happens when the static electric field is positive and beyond the third anticrossing, which introduces a swapping for the occupation and the spin component in the energy levels $|2\rangle$ and $|3\rangle$. Transforming the

configuration of the energy level $|2\rangle$ from a charge occupation (0, 1) with spin up to the configuration (1, 0) with spin down. In the case of the energy level $|3\rangle$ the change occurs from a charge occupation (1, 0) with spin down to the configuration (0, 1) with spin up.

Since the ground state is experimentally the simplest to prepare, our qubit will be encoded in the first and second energy levels, and to find temporal evolutions resembling the Landau-Zener dynamics, we will focus in the anticrossing involving this pair of levels; which is located at the center of figure 4.12.

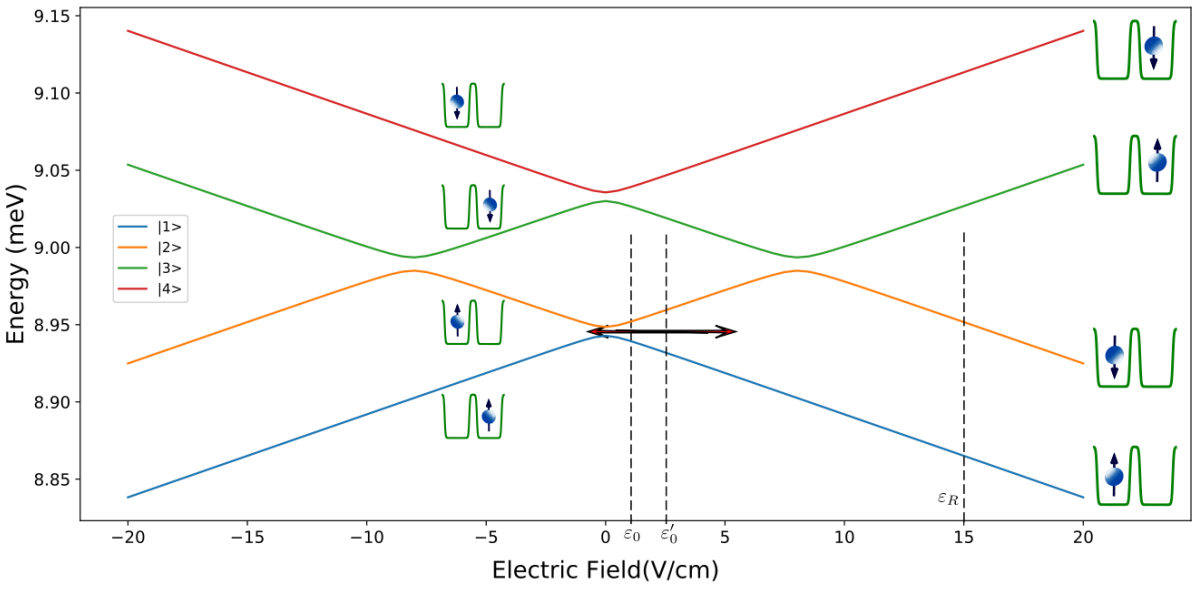

Figure 4.12: Level structure for a double quantum dot with a separation barrier of $B_w = 70$ nm, separating two quantum finite square wells of width $W_w = 40$ nm each. The lines shows the different system bias to simulate a flip operation between the first two levels, via different mechanisms; $\varepsilon_R = 15$ V/cm for Rabi, and $\varepsilon_0' = 2.5$ V/cm for Landau-Zener.

The best way to establish the presence of the Landau-Zener phenomenon would be by applying a large linear swept as proposed in the original references [51] and [50]. Unfortunately, the level structure in figure 4.12 has a major shortcoming, since the anticrossings are poorly isolated from the dynamical influence of each other, and for this reason it is impossible to apply a long swept without expecting leaks from the two state qubit population to the upper levels. Therefore, if we want to study the presence of such phenomenon as clearer as possible, we must restrict the parameters of the oscillating pulses in eq. (4.6) such that the state of the system remains under the influence of a single anticrossing (in our case the central one at the bottom in figure 4.12). Thus the farthest value of the pulse from the center (which depends of the addition of the system bias ε_0 and the amplitude A) must not pass the neighboring anticrossings. Mathematically, this is equivalent to satisfy the following condition $|\varepsilon_0| + |A| < 8$ V/cm (since the two neighboring anticrossings are located at -8 and 8 V/cm in this case).

Given the aforementioned restrictions that do not allow the driving field to go beyond

any of the two neighboring anticrossings, there is the possibility that it could compromise the observation of the Landau-Zener effect, since we could be out of the strong regime. However our results suggest differently, and we obtained Landau-Zener interferences despite the limited range in the pulse amplitude. Before presenting a possible way out to circumvent this obstacles, lets remember the conditions required to find the Landau-Zener dynamics. In chapter 2, we concluded that the two relevant factors necessary to observe the Landau-Zener phenomenon, are:

1. To have a set of parameters of the driving force in the strong regime of the system.

2. Measure the temporal evolution in an orthogonal basis different from the eigenstates of the time-independent Hamiltonian H_0.

In order to fulfill the second condition, we must alter the correspondance between the measurement basis states and the eigenstates of the independent Hamiltonian H_0 (which normally are the same set of states), this can be done in two ways.

First, by changing the measurement basis with respect to the eigenstates of H_0. For example, in chapter 2 this is exactly what was done in the temporal evolution shown in figure 2.9, where we used the time-independent part of the Hamiltonian in eq. 2.5 as the H_0 (which eigenstates are the same of σ_z), but as the measurement basis we used the eigenstates of σ_x. We observed the Landau-Zener dynamics despite using the Rabi Hamiltonian.

Second, by keeping the measurement basis as the eigenstates of H_0, but modifying somehow the time-independent part of the Hamiltonian. In chapter 2, we saw this is possible for a two-level system by applying a rotation of $R_y(\pi/2)$. But in the case of our platform, we can break the correspondence between the measurement basis states and the eigenstates of H_0 by introducing an additional bias (an static electric field) in the pulseε_p to eq. (4.6). Thus the pulse for this case is

$$\varepsilon(t) = \varepsilon_p + A\sin(\omega t).$$

To see how the addition of this pulse bias is equivalent to the second strategy, we can visualize the effect of theε_p in the following way.

Let us call H_0 the time independent part of the Hamiltonian without the pulse bias ε_p in eq. (4.7), and the time dependent part as $H_i = e\varepsilon_p x + exA\sin(\omega t)$. After solving the eigenvalue problem for H_0, we have the set of eigenstates $\{|n\rangle\}$ used as our measurement basis. As well as in chapter 2, the initial condition can be any state expanded in the $\{|n\rangle\}$ basis, by simplicity let us choose $|\psi(0)\rangle = |1\rangle$ (as done in most temporal evolutions shown in this section). Let us also call

$$H_0(\varepsilon_0 = 0) = -\frac{\hbar^2}{2m^*}\frac{d^2}{dx^2} + V_w(x) + \frac{1}{2}g\mu_B B_x\sigma_x + H_{SO},$$

corresponding to our H_0 with a zero system bias $\varepsilon_0 = 0$. Therefore

$$H_0 + H_i = H_0(\varepsilon_0 = 0) + e\varepsilon_0 x + e\varepsilon_p x + exA\sin(\omega t).$$

In terms of the effective system bias $\varepsilon_0' = \varepsilon_0 + \varepsilon_p$, we have

$$H_0 + H_i = H_0(\varepsilon_0 = 0) + e\varepsilon_0' x + exA\sin(\omega t),$$

which can be rewritten in terms of $H_0' = H_0(\varepsilon_0 = 0) + e\varepsilon_0' x$, and $H_i' = exA\sin(\omega t)$. In any evolution of the states (whether performed with $H_0 + H_i$ or with $H_0' + H_i'$) we keep the measurement basis in the eigenstates of H_0 (this fulfills the aforementioned second requirement to observe the Landau-Zener phenomenon).

Mathematically, the temporal evolutions with both sets of Hamiltonians is the same and it is true that $H_0 + H_i = H_0' + H_i'$, but the measurement basis for $H_0' + H_i'$ is no the basis constituted by the eigenstates of H_0'.

The aforementioned implies that to perform an evolution with the eigenstates of H_0 and a pulse with an additional bias, and then measure in their eigenstates, is equivalent to perform an evolution with a Hamiltonian H_0' with the effective bias ε_0' and a pulse with No additional bias, and then measure in the eigenstates of the original H_0.

With this second strategy it is possible to observe the usual Landau-Zener interferences, found with the grid search method applied on the amplitude and frequency of the harmonic electric pulse, in the same way as done in chapter 2. The constructive interference can be appreciated in figure 4.13 and the destructive interference is illustrated in figure 4.14.

The fact that we can obtain the population inversion with the constructive interference, despite being out of the resonance frequency (nor harmonics of such frequency) and with an additional bias in the pulse i.e. with $\varepsilon_p \neq 0$[2], rules out the possibility that such population invertion is achieved thanks to the Rabi dynamics. This fact suggest that we are in the strong regime (or at least in the intermediate) in the amplitude A of the driving field, where the Landau-Zener phenomenon leads the temporal evolutions.

[2]precisely the opposite of the two requirements for Rabi, as seen in the first section fo chapter 2, and in table 2.1.

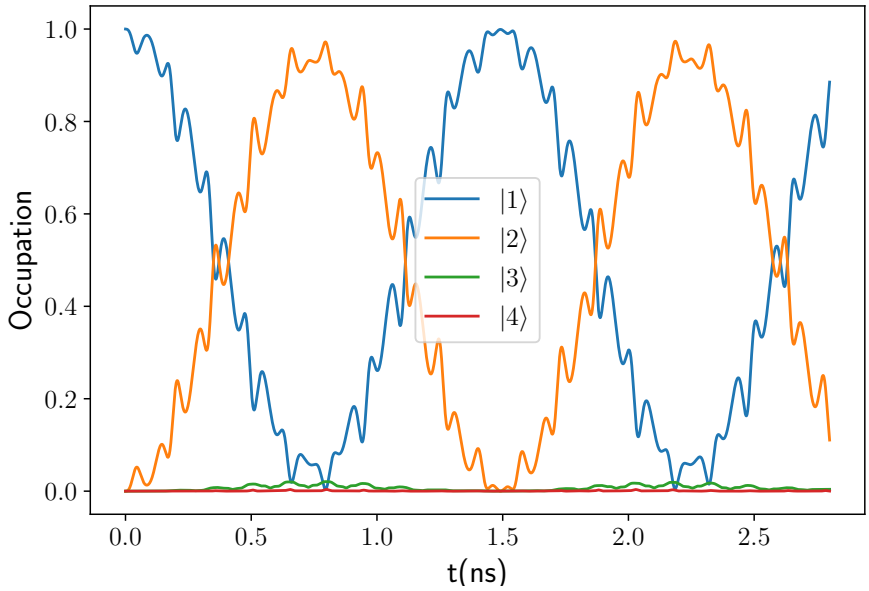

Figure 4.13: Constructive interference of the Landau-Zener transitions after multiple passage trough the central anticrossing region in figure 4.12 with a sinusoidal pulse defined as in eq. (4.6). With parameters: $A = 3.0$ V/cm and $\omega = 111.92$ GHz (out of the resonance). The basis correspond to a system bias of $\varepsilon_0 = 1.5$ V/cm, and the pulse bias is $\varepsilon_p = 1.0$ V/cm, therefore the effective bias is $\varepsilon_0' = 2.5$ V/cm, where the evolution happens.

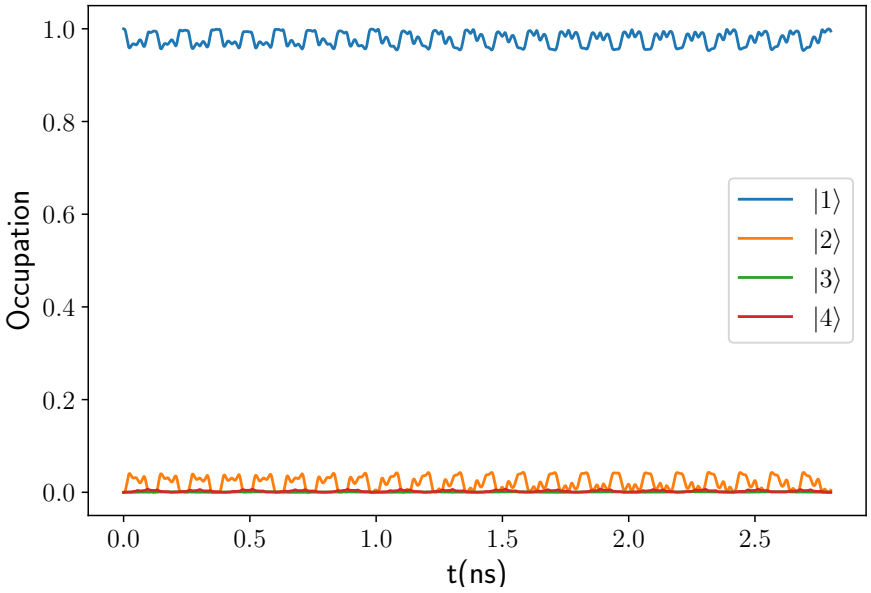

Figure 4.14: Destructive interference of the Landau-Zener transitions after multiple passage trough the central anticrossing region with a sinusoidal pulse defined as in eq. (4.6). With parameters: $A = 4.03$ V/cm and $\omega = 410.15$ GHz. The basis correspond to a system bias of $\varepsilon_0 = 1.5$ V/cm, and the pulse bias is $\varepsilon_p = 1.5$ V/cm, therefore the effective bias is $\varepsilon_0' = 3.0$ V/cm.

4.3.2 Rabi oscillations

In order to observe Rabi oscillations and avoid undesired Landau-Zener transitions, we choose an electric bias away from the anticrossings at $\varepsilon_R = 15$ V/cm, and apply an electric pulse with the same amplitude of the pulse applied in the constructive interference in figure 4.13, but this time the pulse frequency is set in the resonance of the two qubit states (the characteristic trait of Rabi). As we can see apart from the first two levels, there is practically no participation of the superior levels. This temporal evolution can be seen in figure 4.15, where the inversion of population of the qubit states takes a little more than 120 ns, a time notably longer than the $T \approx 0.7$ ns that takes in the constructive interference of Landau-Zener.

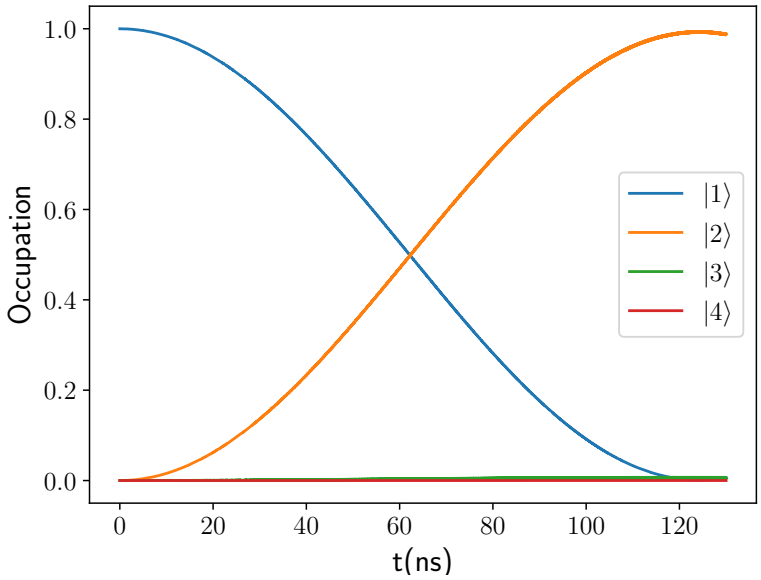

Figure 4.15: Rabi oscillation for the first two levels in a double quantum dot. For a sinusoidal pulse with $A = 2.5909$ V/cm, $\omega = 358.36$ GHz (in the resonance). The basis correspond to a Bias of $\varepsilon_0 = \varepsilon_R = 15$ V/cm, as depicted in figure 4.12.

4.4 Quantum gates in the double QD

With the assistance of quantum optimal control (in this case with the TBQCP method introduced in chapter 3) we can take a step further and perform more sophisticated operations than a mere population inversion as shown in the last section with the Rabi and Landau-Zener dynamics. Here, we tailor the pulse associated with three common one-qubit quantum gates introduced in chapter 2. We start with the universal quantum gate X, which transformation can be described by the matrix

$$X = \begin{bmatrix} 0 & 1 \\ 1 & 0 \end{bmatrix}. \tag{4.9}$$

For this gate we optimized an electric pulse, see figure 4.16, which can achieve a fidelity of 99% with respect to the ideal target. The temporal evolution induced by this pulse on our system is shown in figure 4.17 with a duration of $T = 0.5$ ns, which is slightly faster than the time of the constructive Landau-Zener in figure 4.13 with $T \approx 0.7$ ns. This can be caused by the fact that our X gate is universal (a more complex operation requiring the optimization of three state temporal evolutions), and it can transform any state as the transformation in eq. (4.9) (differently from the specific transformation of the state $|\psi(0)\rangle = |1\rangle$ realized with Rabi and Landau-Zener). Also the coupling element in the dipole matrix that connects the states $|1\rangle$ and $|2\rangle$ is relatively low compared with the one of other arrangements for different barrier widths.

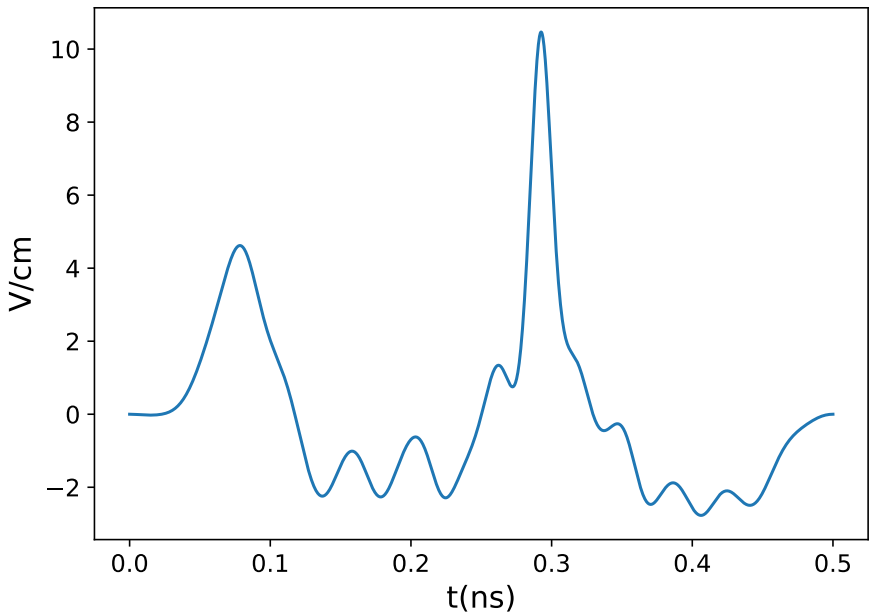

Figure 4.16: Optimized pulse for the universal X gate, with a system bias of $\varepsilon_0 = 1.5$ V/cm, in the arrangement with a barrier width of $B_W = 70$ nm. This pulse guarantees a fidelity of 99%, and required 257 iterations with the TBQCP method.

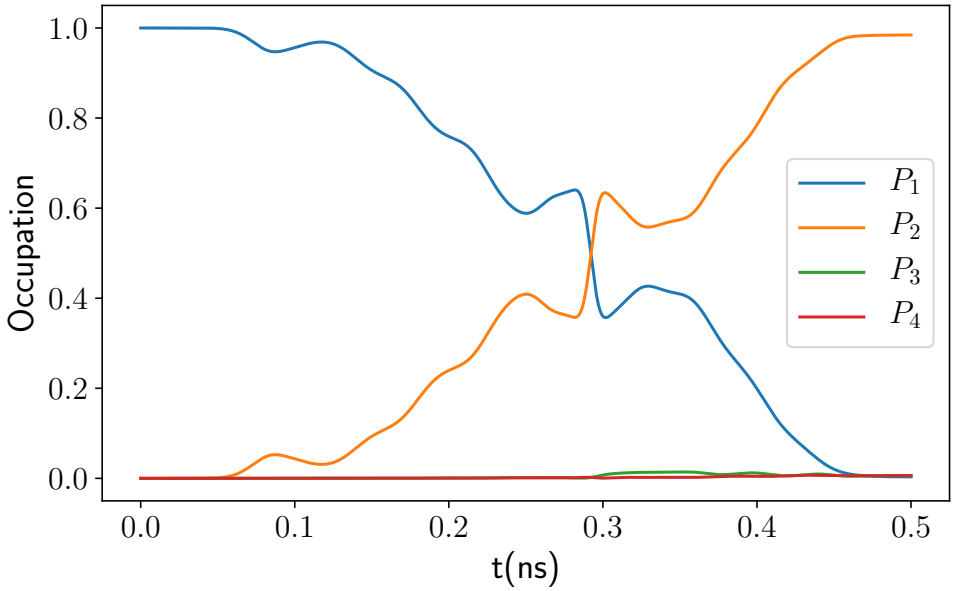

Figure 4.17: Temporal evolution of the occupation states for a system bias of $\varepsilon_0 = 1.5$ V/cm, in the arrangement with a barrier width of $B_W = 70$ nm, with the initial condition $|\psi(0)\rangle = |1\rangle$ and under the action of the optimized pulse in figure 4.16. Ideally this operation must transform our initial condition as $|1\rangle \longrightarrow |2\rangle$, (according to our notation of the levels).

The improvement in efficiency when we apply quantum optimal control on the arrangement with a barrier width of $B_w = 70$ nm, is not really that much if we compare the X gate with the constructive Landau-Zener in figure 4.13. However, there is a faster way if we take in account that as the width of the barrier decreases, the coupling increases significantly (as can be seen from the matrix elements of the dipole matrix), this is expected since a wider separation restricts the tunneling between the quantum wells. Therefore, a better arrangement in this platform corresponds to the system with higher couplings, for example in an arrangement with a separation of $B_w = 30$ nm (even though the level structure change to have a single anticrossing in the four levels, for the optimal quantum control, this is irrelevant).

For this arrangement, besides the X gate, we also implemented the following two quantum gates [44, 45]

$$H = \frac{1}{\sqrt{2}} \begin{bmatrix} 1 & 1 \\ 1 & -1 \end{bmatrix}, \tag{4.10}$$

$$R_{\pi/8} = \begin{bmatrix} 1 & 0 \\ 0 & e^{i\pi/8} \end{bmatrix}. \tag{4.11}$$

Representing eq. (4.10) is the Hadamard gate (which corresponds to a 180 degree rotation around the X axis, followed by a rotation of 90 degree rotation around the Y axis

of the Bloch sphere), and eq. (4.11) is the $\pi/8$ gate (it equates to a rotation around the Z-axis of the Bloch sphere by $\pi/8$ radians). These electric pulses and their respective power spectrum are illustrated in figures 4.18, 4.20, 4.22. As expected from optimized pulses via a quantum optimal control method, these pulse profiles are notably more complex than the sinusoidal pulse of eq. (4.6) (used in the Rabi and Landau-Zener mechanisms), as can be seen in the modulation of amplitude and the power spectrum that reveals a variety of frequencies involved in these pulses.

As explained in chapter 3, the quantum gates require the optimization of the TBQCP method on $k+1$-states, with $k=2$ for a qubit (e.g. the two states of the canonical basis $|0\rangle$ and $|1\rangle$), and the third state corresponds to an arbitrary superposed state. For the case of the X gate any initial state in the Bloch sphere

$$|\psi(0)\rangle = \cos\frac{\theta}{2}|0\rangle + e^{i\phi}\sin\frac{\theta}{2}|1\rangle, \tag{4.12}$$

is transformed respectively, to a final state given by

$$|\psi(T)\rangle = X|\psi(0)\rangle = e^{i\phi}\sin\frac{\theta}{2}|0\rangle + \cos\frac{\theta}{2}|1\rangle. \tag{4.13}$$

In order to certify that the optimized pulse of our X gate effectively connects any initial qubit with its respective final state given by eq. (4.13), then we simulated the temporal evolution of 1012 uniformly distributed initial states around the Bloch sphere, transformed with the optimized pulse of the X gate illustrated in figure 4.18 (the same verification can be applied for the pulses of the other gates). The results of such simulation can be appreciated in figure 4.19, where we calculated the fidelity between the ideal state of eq. (4.13) and the state at the final time $|\psi(T)\rangle$ that was evolved under the action of the pulse. In figure 4.19 we can observe that the fidelity for the different states is close to 1 (being 0.984 the worse result), with small variations for the fidelity of the evaluated states. Results that verifiy the correspondence between the optimized pulses and the unitary transformations associated to every gate.

In the three figures of 4.18, 4.20, and 4.22; the power spectrum shows that the relevant frequencies range from 0 to 400 GHz, but a notably difference is that the main contribution of frequencies for the $\pi/8$ gate lies in frequencies below 180 GHz, while the power spectrum of the X and Hadamard gates are broader and the main contributions occur for frequencies below 360 GHZ.

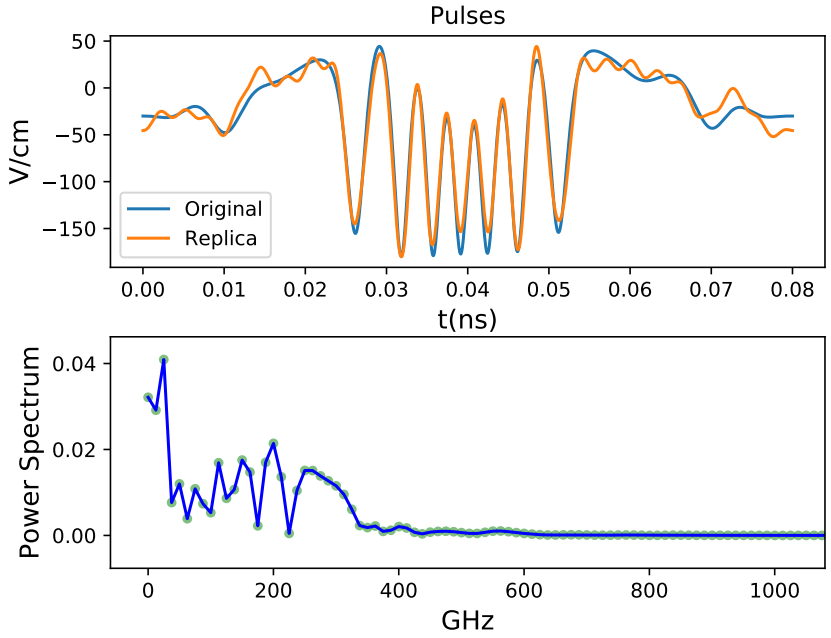

Figure 4.18: On the top plot, we have the original X universal gate optimized pulse (blue), and its reconstructed version (orange) retailored with 20 Fourier coefficients. The plot below is the power spectrum of the original pulse. The basis correspond to a system bias of $\varepsilon_0 = -30$ V/cm, in the arrangement with a barrier width of $B_W = 30$ nm. The original pulse guarantees a fidelity of 99%, and required 1658 iterations.

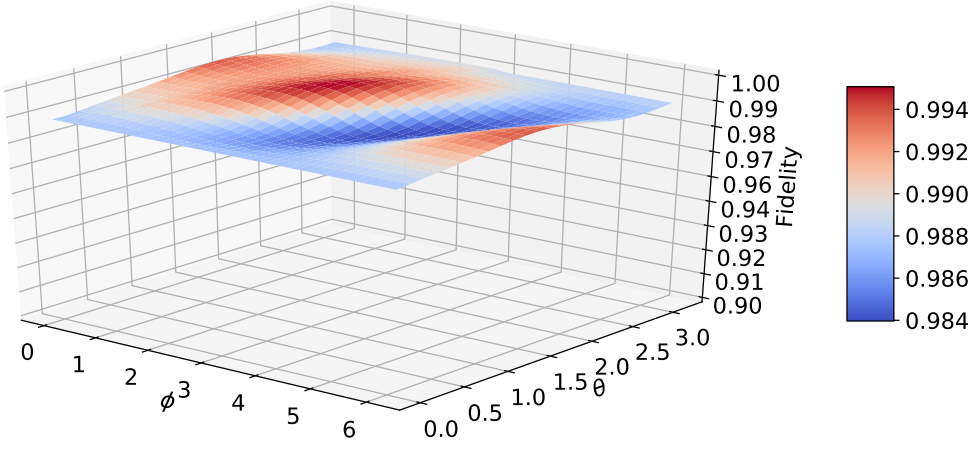

Figure 4.19: Fidelity of 1012 uniformly distributed initial states around the Bloch sphere, transformed with the optimized pulse of the X gate in figure 4.18.

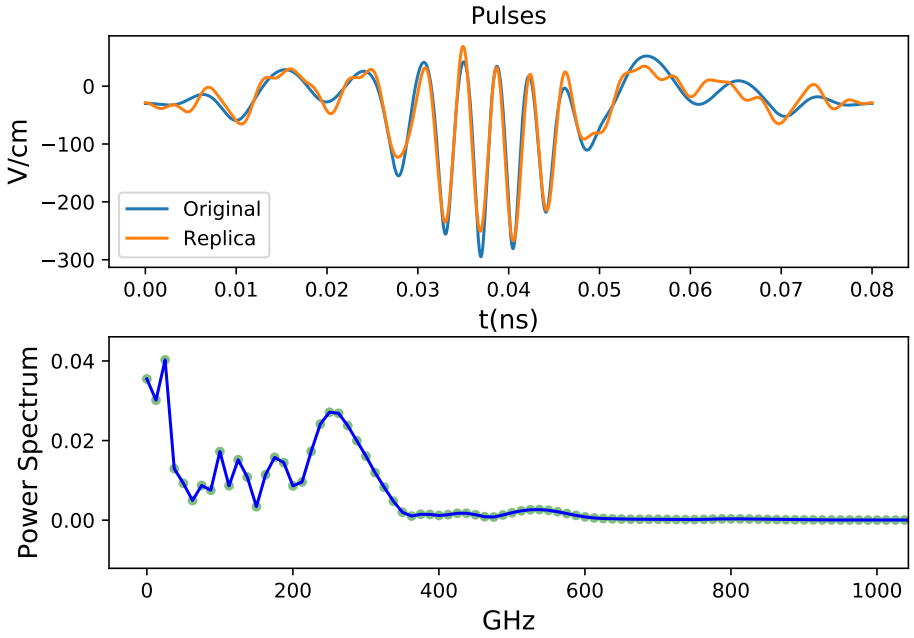

Figure 4.20: On the top plot, we have the original Hadamard universal gate optimized pulse (blue) and its reconstructed version (orange) retailored with 20 Fourier coefficients. The plot below is the power spectrum of the original pulse. The basis correspond to a system bias of $\varepsilon_0 = -30$ V/cm, in the arrangement with a barrier width of $B_W = 30$ nm. The original pulse guarantees a fidelity of 99%, and required 5447 iterations.

With the pulses of figures 4.18, 4.20, and 4.22 we can achieve a fidelity of 99% (or fields with higher fidelity could be tailored depending on the iteration number) in only 0.08 ns. This is an order of magnitude faster than the previous temporal evolutions; it is an important improvement if we take in account that the decoherence time for this platform is 0.16 μs, and that the relaxation time does not affect coherent evolution on timescales up to 1 μs, as reported in ref. [116]. It suggest that it is possible to perform various operations reliably before losing the quality of the information. To illustrate the transformation performed by one of this pulses in this arrangement, we choose one of the three temporal evolutions optimized for the Hadamard gate, starting with the initial condition $|\psi(0)\rangle = |2\rangle$ (the second state of our qubit). Ideally this operation must transform our initial condition as $|2\rangle \longrightarrow (|1\rangle - |2\rangle)/\sqrt{2}$, (according to our notation of the levels) which was reasonably approximated by our pulse, as can be seen in the temporal evolution of figure 4.21.

4.4.1 Fourier reconstructions of the optimized pulses vs the fidelity

The original pulses can achieve fidelities of 99%, but since they are tailored via optimization methods, there is not an analytic function that describe them but the numerical

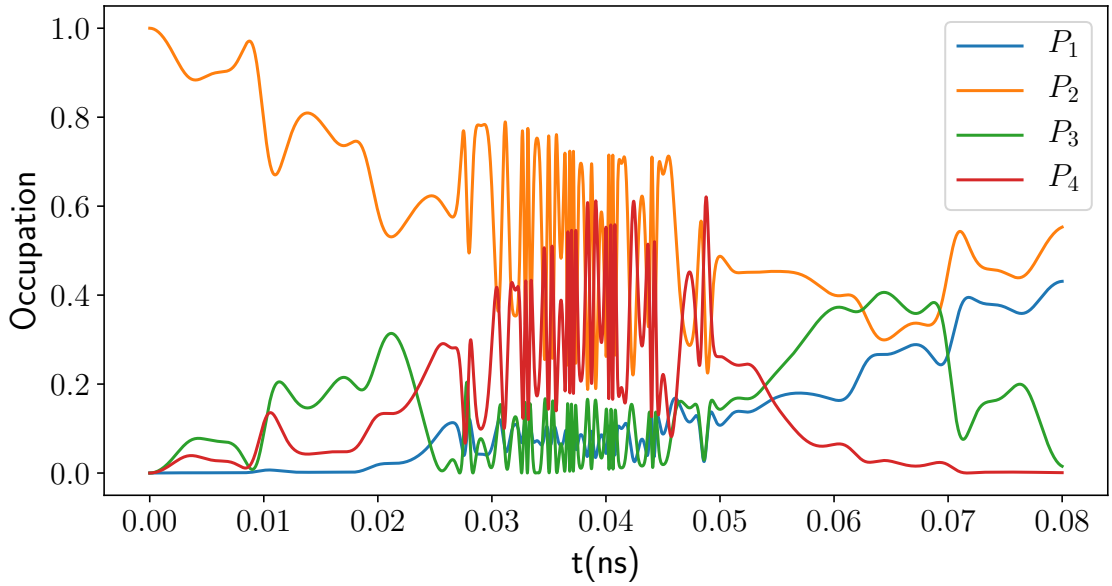

Figure 4.21: Temporal evolution of the occupation states for a system bias of $\varepsilon_0 = 1.5$ V/cm, in the arrangement with a barrier width of $B_W = 30$ nm, with the initial condition $|\psi(0)\rangle = |2\rangle$ (the second state of our qubit) and under the action of the optimized pulse of the Hadamard gate in figure 4.20. Ideally this operation must transform our initial condition as $|2\rangle \longrightarrow (|1\rangle - |2\rangle)/\sqrt{2}$, (according to our notation of the levels).

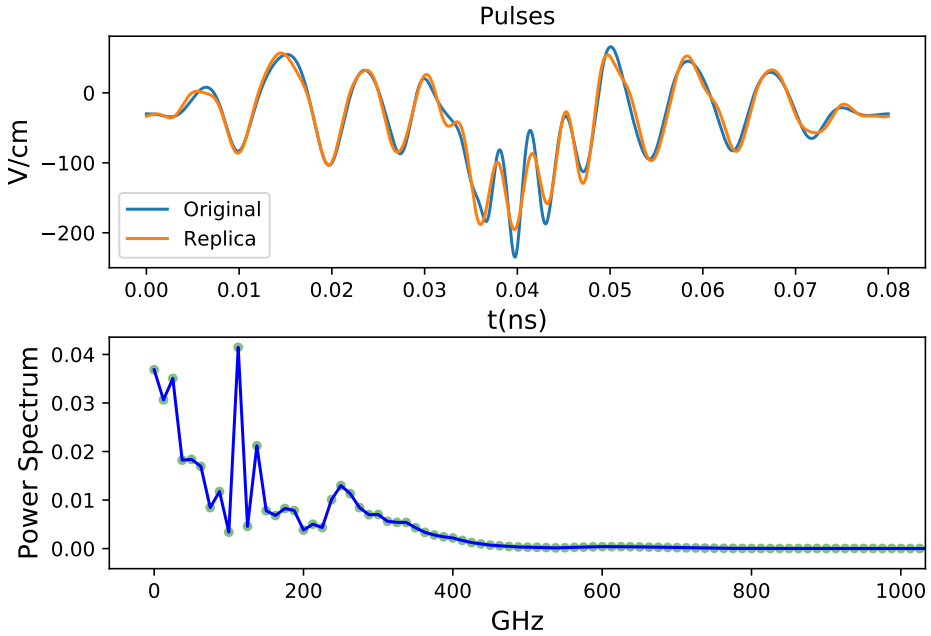

Figure 4.22: On the top plot, we have the original $\pi/8$ rotation universal gate optimized pulse (blue), and its reconstructed version (orange) retailored with 20 Fourier coefficients. The plot below is the power spectrum of the original pulse. The basis correspond to a system bias of $\varepsilon_0 = -30$ V/cm, in the arrangement with a barrier width of $B_W = 30$ nm. The original pulse guarantees a fidelity of 99%, and required 18260 iterations.

optimized field. Thus, in order to facilitate the experimental generation of these pulses, we compute the power spectrum from the data of the pulse profiles and then we reconstruct the pulse with Fourier series, which harmonic functions are simpler to generate. But what constitutes an acceptable reconstruction of these new pulses?

This is a relevant problem in the area of quantum metrology, where it is important to determine the highest precision possible, given a set of limited resources. In this case, what is relevant to be preserved is the quality of the transformation, which can be quantified with the fidelity of the gate. For this reason we reconstructed the pulses of our three quantum gates with different number of Fourier coefficients (considering those frequencies w_j with higher modulus in the discrete Fourier transform $\left|\tilde{f}_{w_j}\right|$). It is known that the greater the number of these Fourier coefficients, the better the reconstruction of the pulse. How many are good enough to reproduce a pulse that guarantees a minimum required fidelity?. This can be seen in figures 4.23, 4.24, 4.25, where we can see that for a number below 28 coefficients, the fidelity can fluctuate significantly from one number of coefficients to the next. This suggests that at least 28 coefficients, is desireble. Also, below such number, the fidelity falls below 90% (except for the $\pi/8$ gate which fidelity rise faster and even with 14 coefficients stays over 90%). For higher number of coefficients, this variation stops and the fidelity stabilizes in a plateau (where the fidelity does not fall below 98%).

For the X and Hadamard gates in figures 4.24, 4.25 the trend for a low number of Fourier coefficients (lower than 20) is an slower increase in the fidelity, compared to the fast rise in the fidelity for the same number of Fourier coefficients in the $\pi/8$ gate in figure 4.23. This disparity in the improvement of the fidelity is related to the difference in the peaks and valleys of the power spectrum, which it is more pronounced in the $\pi/8$ gate. Thus, even with a few coefficients, let us say, 15 or 16 Fourier coefficients in the $\pi/8$ gate, the most relevant frequencies are included and the fidelity is higher as 90%. While a bigger number of Fourier coefficients are required in the case of the X and Hadamard gates, to include the frequencies that contribute the most and yield a fidelity of 90%.

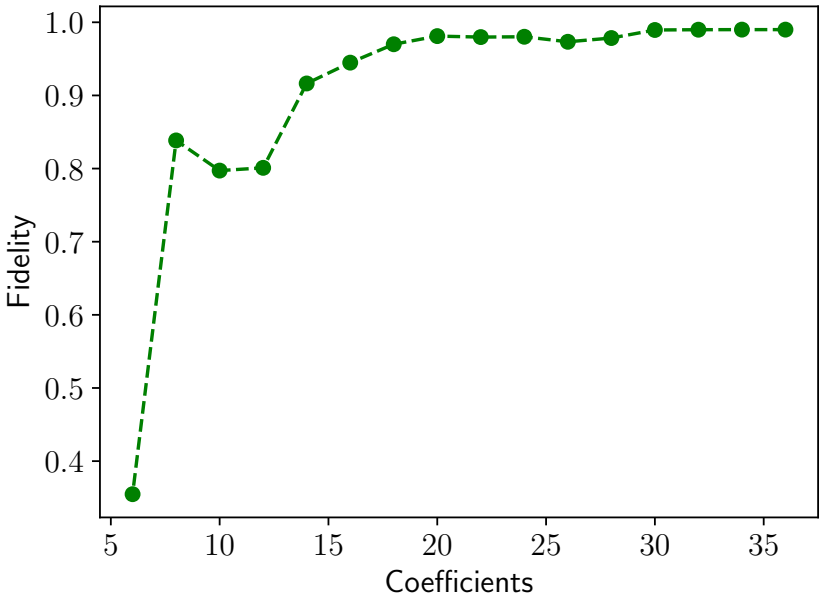

Figure 4.23: Fidelity vs number of coefficients, used to retailor the $\pi/8$ rotation universal gate optimized pulse in figure 4.13. A good performance in the reconstructed pulses of this gate can be guaranteed for a number of coefficients higher than 28. With a fidelity higher than 98%.

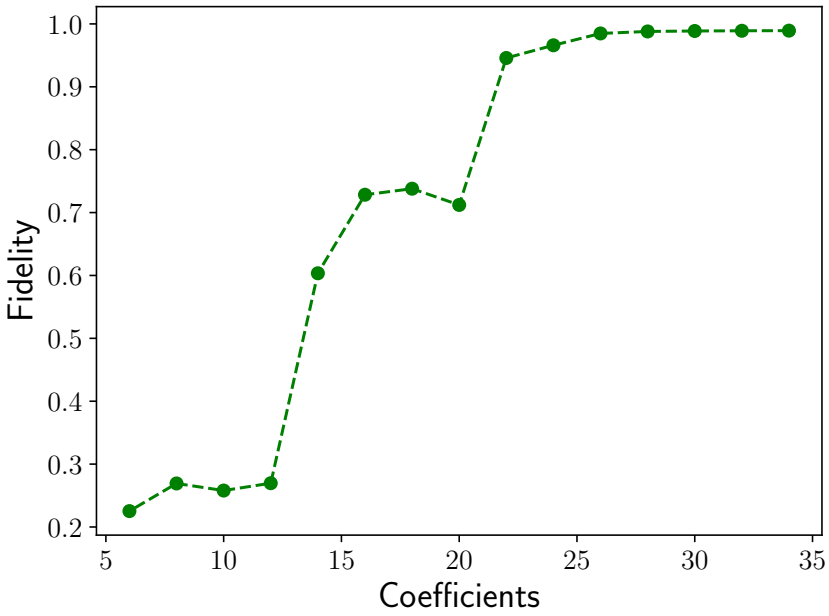

Figure 4.24: Fidelity vs number of coefficients, used to retailor the X universal gate optimized pulse in figure 4.13. A good performance in the reconstructed pulses of this gate can be guaranteed for a number of coefficients higher than 28. With a fidelity higher than 98%.

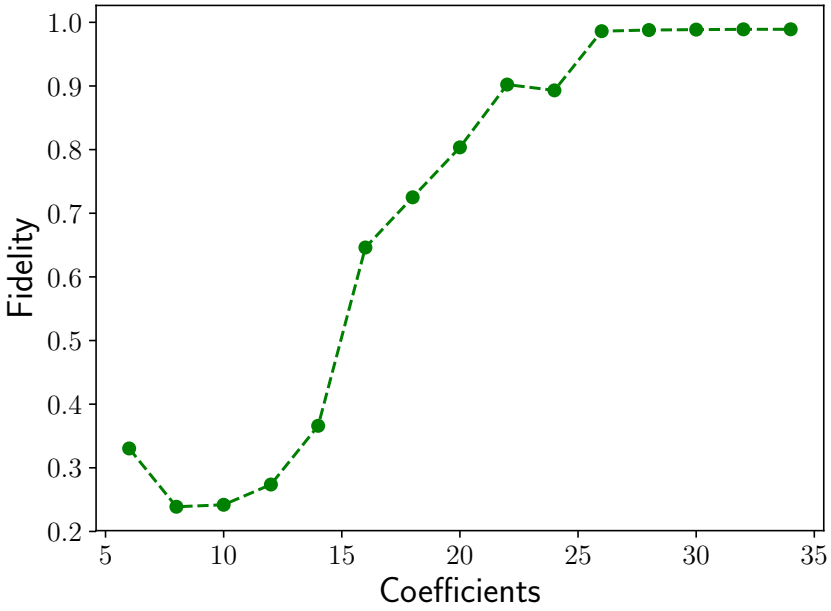

Figure 4.25: Fidelity vs number of coefficients, used to retailor the Hadamard universal gate optimized pulse in figure 4.13. A good performance in the reconstructed pulses of this gate can be guaranteed for a number of coefficients higher than 28. With a fidelity higher than 98%.

Chapter 5

Hybrid qubit

As a step further in our platform explorations, here we simulate the physical realization of a quantum algorithm of qutrits (a unit of quantum information consisting of three quantum states) in the platform of gated lithographic double quantum dots (DQDs). We begin this chapter describing the quantum permutation algorithm (QPA) [121] and the quantum gates involved in its execution. Although the algorithm requires the optimization of eight electrical pulses corresponding to the different one-qutrit quantum gates, the execution of the algorithm requires the application of three of these quantum gates in sequential order. We show the optimized electric pulses that were tailored with the aid of the TBQCP method in the quantum speed limit, i.e. the minimum time required to achieve the respective transformation of every gate, that assures a fidelity higher than 0.9997. Furthermore, we compare the total time required by an hypothetical execution of the quantum algorithm, with the decoherence and relaxation times of the physical platform. We also evaluate the performance of such execution under a noisy environment with a charge noise model. At the end of the chapter we discuss the results and conclusions corresponding to this numerical experiment.

5.1 Quantum Permutation Algorithm

Consider a set with three elements $\{1, 2, 3\}$. For this set there are six possible permutations, three with even parity $(1, 2, 3)$, $(3, 1, 2)$, $(2, 3, 1)$; and three with odd parity $(3, 2, 1)$, $(2, 1, 3)$, $(1, 3, 2)$. The objective of the QPA [121] is to determine the parity of the permutations, and its protocol can be illustrated by associating the permutation to a function $f(x)$ on the set $x \in \{1, 2, 3\}$. Classically, one must evaluate $f(x)$ for two different values of x, while the QPA can determine the parity with a single evaluation of $f(x)$ [121].

In order to show how the QPA works, we use the qutrit as unit of quantum information to encode the three elements of the set, which can be written as

$$|1\rangle = \begin{pmatrix} 1 \\ 0 \\ 0 \end{pmatrix}, \; |2\rangle = \begin{pmatrix} 0 \\ 1 \\ 0 \end{pmatrix}, \; |3\rangle = \begin{pmatrix} 0 \\ 0 \\ 1 \end{pmatrix}. \tag{5.1}$$

The determination of the parity of a permutation is equivalent to the determination of the parity of six permutation functions, which we represent with six unitary operators constructed with the base in eq. (5.1). Three of this operators are associated to the even permutations Π_1, Π_2 and Π_3 which map the set of states $(1, 2, 3)$ to the sets of states $(1, 2, 3)$, $(3, 1, 2)$, and $(2, 3, 1)$, respectively. The even permutations operators are cast as

$$\Pi_1 = \begin{pmatrix} 1 & 0 & 0 \\ 0 & 1 & 0 \\ 0 & 0 & 1 \end{pmatrix}, \; \Pi_2 = \begin{pmatrix} 0 & 1 & 0 \\ 0 & 0 & 1 \\ 1 & 0 & 0 \end{pmatrix}, \; \Pi_3 = \begin{pmatrix} 0 & 0 & 1 \\ 1 & 0 & 0 \\ 0 & 1 & 0 \end{pmatrix}. \tag{5.2}$$

The three operators associated to the odd permutations Π_4, Π_5 and Π_6 are those that respectively map from the set of states $(1, 2, 3)$ to the sets of states $(3, 2, 1)$, $(2, 1, 3)$, and $(1, 3, 2)$. They are

$$\Pi_4 = \begin{pmatrix} 0 & 0 & 1 \\ 0 & 1 & 0 \\ 1 & 0 & 0 \end{pmatrix}, \; \Pi_5 = \begin{pmatrix} 0 & 1 & 0 \\ 1 & 0 & 0 \\ 0 & 0 & 1 \end{pmatrix}, \; \Pi_6 = \begin{pmatrix} 1 & 0 & 0 \\ 0 & 0 & 1 \\ 0 & 1 & 0 \end{pmatrix}. \tag{5.3}$$

In order to implement the QPA, the system must be initialized in state $|2\rangle$, then the quantum Fourier transform (QFT) of a qutrit is applied to this initial state. This, is given by

$$U_{FT} = \frac{1}{\sqrt{3}} \begin{pmatrix} 1 & 1 & 1 \\ 1 & \exp(i2\pi/3) & \exp(-i2\pi/3) \\ 1 & \exp(-i2\pi/3) & \exp(i2\pi/3) \end{pmatrix}. \tag{5.4}$$

The obtained state is the following superposition of the three states

$$|\psi_1\rangle = U_{FT}|2\rangle = \frac{|1\rangle + \exp(i2\pi/3)|2\rangle + \exp(-i2\pi/3)|3\rangle}{\sqrt{3}}. \tag{5.5}$$

In Fig. 5.1 we show a quantum circuit that represents the QPA. The second gate in Fig. 5.1 encodes one of the six possible permutations operators Π_k, with $k = 1, 2, .., 6$. The resulting state is $|\psi_k\rangle = \Pi_k|\psi_1\rangle$. To determine the parity of the permutation, one must apply the gate $U_{FT}^{\dagger}$ and measure the system to check the six possible outcomes, which are described by the following states

Even	Odd
$U_{FT}^{\dagger}\|\psi_1\rangle = \|2\rangle$	$U_{FT}^{\dagger}\|\psi_4\rangle = e^{-2\pi i/3}\|3\rangle$
$U_{FT}^{\dagger}\|\psi_2\rangle = e^{2\pi i/3}\|2\rangle$	$U_{FT}^{\dagger}\|\psi_5\rangle = e^{2\pi i/3}\|3\rangle$
$U_{FT}^{\dagger}\|\psi_3\rangle = e^{-2\pi i/3}\|2\rangle$	$U_{FT}^{\dagger}\|\psi_6\rangle = \|3\rangle$

(5.6)

Discarding a gloval phase, if the measured state is $|2\rangle$ ($|3\rangle$), the parity of the applied permutation was even (odd). In such a way, only one evaluation of $f(x)$ is necessary in contrast with the classical algorithm, where two evaluations of $f(x)$ are required. An interesting feature of this algorithm is the fact that entanglement is not necessary and only a superposition with well-defined relative phases is needed.

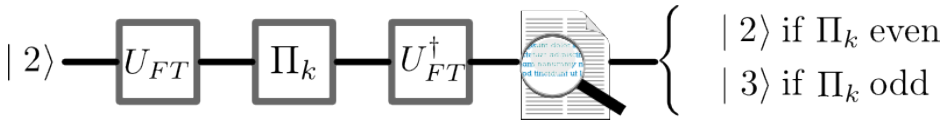

Figure 5.1: Schematic quantum circuit for the quantum permutation algorithm (QPA). The quantum Fourier transform U_{FT} is applied to the initial state $|2\rangle$. Afterward, a permutation Π_k acts on the resulting state $|\psi_1\rangle = U_{FT}|2\rangle$. Subsequently, the gate $U_{FT}^{\dagger}$ is applied to the state $\Pi_k|\psi_1\rangle$ and a measure is performed. If the system is found in the state $|2\rangle$ ($|3\rangle$), the parity Π_k is even (odd).

5.2 Results and Analysis

As a platform for implementing the QPA, we use the Hamiltonian of the hybrid qubit system extracted from Ref. [32], which is given by

$$H(\varepsilon) = \begin{bmatrix} \varepsilon/2 & 0 & \hbar\Delta_1 & -\hbar\Delta_2 \\ 0 & \varepsilon/2 + \hbar\delta E_L & -\hbar\Delta_3 & \hbar\Delta_4 \\ \hbar\Delta_1 & -\hbar\Delta_3 & -\varepsilon/2 & 0 \\ -\hbar\Delta_2 & \hbar\Delta_4 & 0 & -\varepsilon/2 + \hbar\delta E_R \end{bmatrix}, \tag{5.7}$$

where $\Delta_1/2\pi = 2.62$ GHz, $\Delta_2/2\pi = 3.5$ GHz, $\Delta_3/2\pi = 4.6$ GHz, $\Delta_4/2\pi = 1.65$ GHz, $\delta E_L/2\pi = 52.7$ GHz, $\delta E_R/2\pi = 9.2$ GHz, and ε is the detuning. The detuning ε is essentially the energy difference between DQDs that breaks the system symmetry and allows assessing the system states. It is used for state preparation and readout and is controlled by applied gate voltages. The various Δ's represent the tunneling couplings determined by the effective height and width of the potential barriers between the DQDs. In turn, the energy separation between single particle states, δ_E's, are defined by the effective

confinement. All the values used in our simulations were fitted from transconductance measurements as reported in Ref. [32] for gated lithographic DQDs.

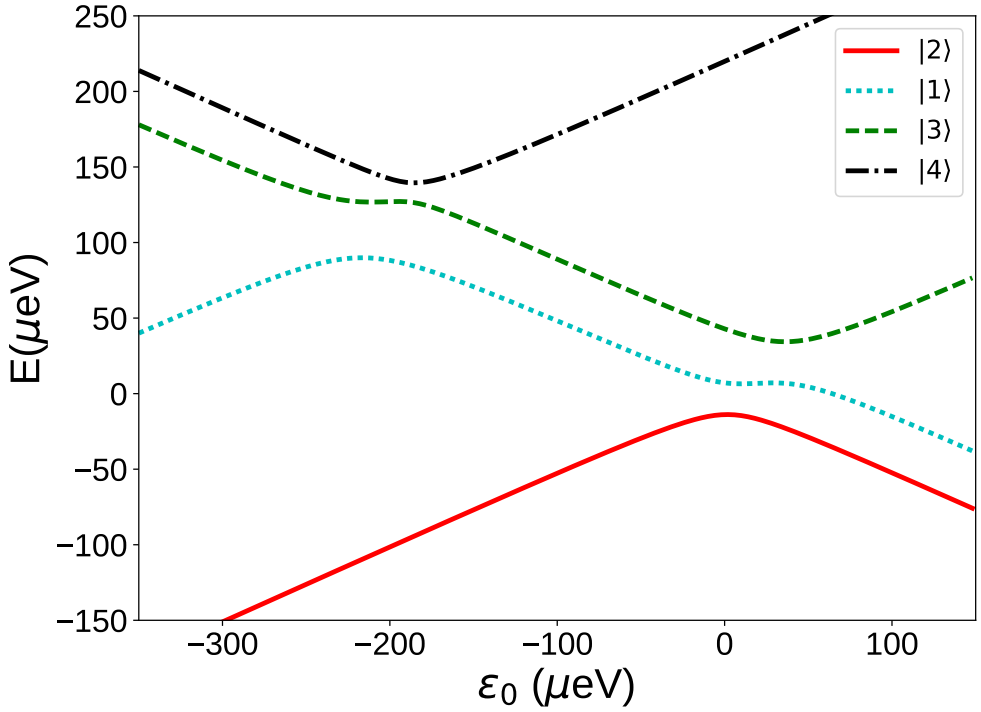

Figure 5.2: The ground $|2\rangle$ (solid curve), first $|1\rangle$ (dotted curve), second $|3\rangle$ (dashed curve), and third $|4\rangle$ (dash-dotted curve) excited states are shown as a function of the detuning.

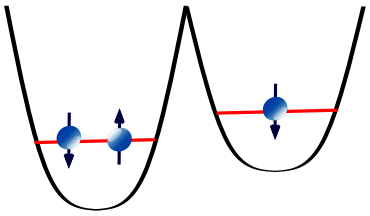

$$(2,1)\begin{cases}|2\rangle = |S\rangle|\downarrow\rangle \\ |1\rangle = \sqrt{\frac{1}{3}}|T_0\rangle|\downarrow\rangle - \sqrt{\frac{2}{3}}|T_-\rangle|\uparrow\rangle\end{cases}$$

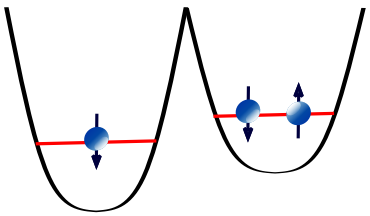

$$(1,2)\begin{cases}|3\rangle = |\downarrow\rangle|S\rangle \\ |4\rangle = \sqrt{\frac{1}{3}}|\downarrow\rangle|T_0\rangle - \sqrt{\frac{2}{3}}|\uparrow\rangle|T_-\rangle\end{cases}$$

Figure 5.3: Physical configuration of the evolution basis states in the DQD for $\varepsilon_0 = 50\mu$eV. The four states indicated with the occupation (in the right and left quantum dots (2,1) for the first two states and (1,2) for the other two states), correspond to three electron states consisting of the direct product of a single electron $|\downarrow\rangle$ and two-electron states (the singlet $|S\rangle$ and the triplets $|T_-\rangle$ and $|T_0\rangle$).

The Hamiltonian of Eq. (5.7) can be diagonalized for each value of detuning and the resulting energy levels are shown in Fig. 5.2. In the system for the reference detuning of

$\varepsilon_0 = 50\mu$eV, the four states of the evolution basis correspond to quantum states of three electrons in two quantum dots, the ground $|2\rangle$ and first excited state $|1\rangle$ of the dot in the (1,2) charge occupation, and the corresponding ground $|3\rangle$ and first excited state $|4\rangle$ of the dot in the (2,1) charge occupation. A qutrit requires only three quantum levels, but we take into account four states as our basis of states to probe leakage effects. The ground state is labeled as $|2\rangle$, while the first excited state is labeled as $|1\rangle$. Such a change is due to the QPA, which is initialized in the state $|2\rangle$ and we choose the initial state as the ground state of the system.

The physical configuration of the four states in the DQD is depicted in Fig. 5.3, where the four states of the system correspond to three electron states. The three electron states correspond to the direct product of a single electron $|\downarrow\rangle$ and two-electron states the singlet $|S\rangle$ and the triplets $|T_i\rangle$, with

$$\begin{aligned} |S\rangle &= (|\uparrow\downarrow\rangle - |\downarrow\uparrow\rangle)/\sqrt{2} \\ |T_+\rangle &= |\uparrow\uparrow\rangle, \\ |T_-\rangle &= |\downarrow\downarrow\rangle, \\ |T_0\rangle &= (|\downarrow\uparrow\rangle + |\uparrow\downarrow\rangle)/\sqrt{2}. \end{aligned} \tag{5.8}$$

The time evolution of the system is given by

$$\frac{\partial|\psi(t)\rangle}{\partial t} = \frac{1}{i\hbar}\left(H_0 - \mu E(t)\right)|\psi(t)\rangle, \tag{5.9}$$

where $H_0 = Z^{-1}H(\varepsilon_0)Z$ is the diagonalized Hamiltonian for a reference detuning ε_0 that provides a basis for the time evolution of the system. Each column of the Z matrix is given by the components of each eigenvector of $H(\varepsilon_0)$. The dipole type matrix is obtained by $\mu = Z^{-1}H_D Z$, where H_D is a matrix composed by only the diagonal elements of $H(\varepsilon = 1)$ that are proportional to ε and $E(t) = \varepsilon(t) - \varepsilon_0$. The optimized field can be obtained using the TBQCP method [126], described in chapter 3 .

The power spectrum of the optimized pulses (Fig. 5.4) are shown in Fig. 5.5. We note that all gates have a nontrivial power spectrum in the range of 0 and 20 GHz, which is in agreement with the eigenenergies scale of the hybrid qubit (see Fig. 5.2). Note that the main frequencies lie below 20 GHz and microwave sources exceeding the 20 GHz threshold have already been used for controlling the inter-dot coupling as reported in Ref. [129]. Also, the technology for producing arbitrary waveform low-noise synthesizers has been systematically evolving as described in Ref. [130].

In Fig. 5.6, we plot the evolution of the state occupation in the four-state basis, for the reference detuning $\varepsilon_0 = 50$ μeV, for the conversion of the initial state $|2\rangle$ by the U_{FT} gate into the target state $|\psi_1\rangle$. In such evolution, we note that there is a very small leakage

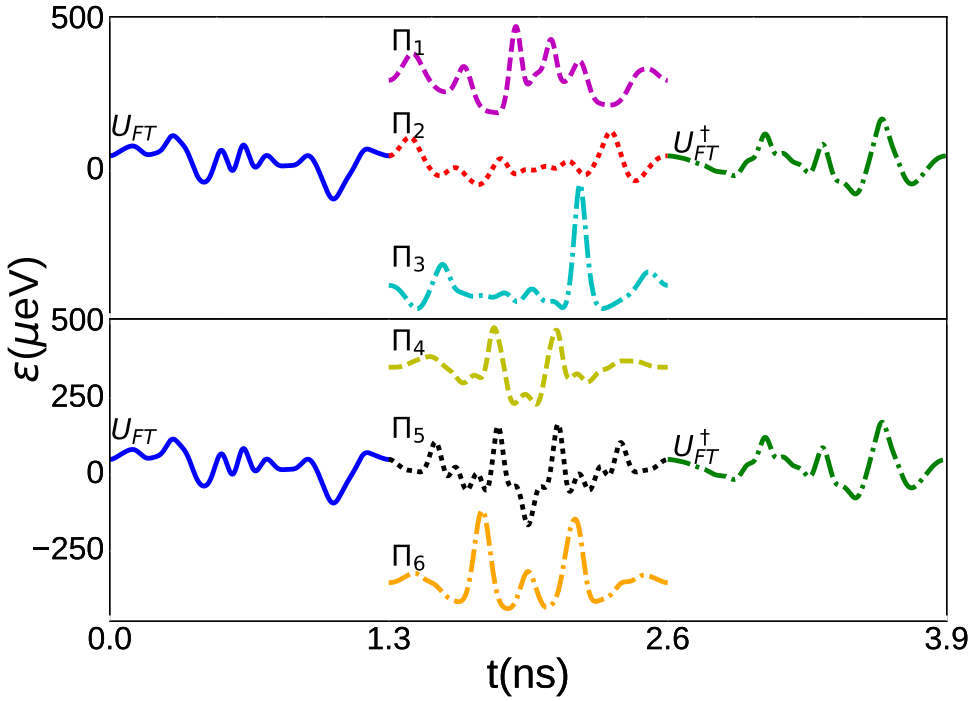

Figure 5.4: Optimized pulses as a function of time, considering the reference detuning $\varepsilon_0 = 50$ μeV. The initial pulse, in each panel, corresponds to the U_{FT} (dark solid curve) gate and the final pulse corresponds to the $U_{FT}^{\dagger}$ gate (dash-dotted curve). The six different pulses in the middle correspond to three even permutations (top panel) and to three odd permutations (bottom panel). The gates Π_1 (dashed curve), Π_3 (dash-dotted curve), Π_4 (dashed curve) and Π_6 (dash-dotted curve) are shown with an offset to better view, but their real reference detuning is $\varepsilon_0 = 50\mu$eV, such as for the other gates Π_2 (dotted curve) and Π_5 (dotted curve).

outside the first three states (the qutrit basis), and the optimal pulse drives the dynamics to yield the target with high fidelity at the final time (see inset of Fig. 5.6). In the inset of Fig. 5.6, we plot the fidelity for the U_{FT} gate as a function of the number of iterations of the TBQCP. For all gates, the leakage to the fourth level was not significant and the fidelity is bigger than 0.9997 for T=1.3 ns. The fidelity depends on the time duration of the pulse, which defines some restrictions for the maximum achieved fidelity. Such dependence is related to the quantum speed limit, which is connected to the minimum time to perform a

T (ns)	U_{FT}	Π_1	Π_2	Π_3	Π_4	Π_5	Π_6	$U_{FT}^{\dagger}$
1.0	261.5	1.6	90.2	916.5	65.9	1414.7	750.4	533.6
1.3	3.9	6.5	3.3	26.8	3.9	26.0	5.3	4.6

Table 5.1: Infidelity for all quantum gates necessary to implement the QPA considering different pulse durations (T=1.0, and 1.3 ns). The infidelity for each case must be multiplied by 10^{-5} to get its real value, *e.g.*, for the U_{FT} the infidelity is 3.9×10^{-5} at T=1.3 ns, which corresponds to a fidelity of 0.999961. The number of iterations for each quantum gate is different for each case, ranging from a minimum of 654 iterations for the U_{FT} gate with $T = 1.3$ ns and a maximum of 15425 iterations for the Π_2 gate with $T = 1.0$ ns.

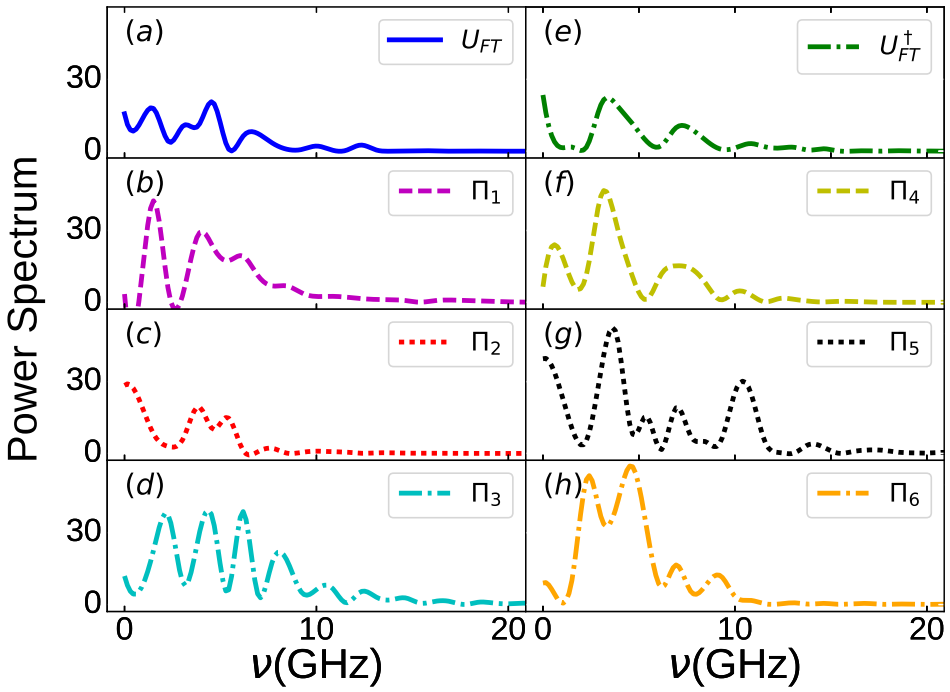

Figure 5.5: Power spectrum of the electric pulses corresponding to the gates (a) U_{FT} (dark solid curve), (b) Π_1 (dashed curve), (c) Π_2 (dotted curve), (d) Π_3 (dash-dotted curve), (e) $U_{FT}^{\dagger}$ gate (dash-dotted curve), (f) Π_4 (dashed curve), (g) Π_5 (dotted curve), and (h) Π_6 (dash-dotted curve).

transition between two states [62, 131]. Moreover, the connection between quantum speed limit and optimal quantum control has already been investigated [131, 64]. In Ref. [64], the quantum speed limit was related to the infidelity $\mathcal{I} = 1 - |\langle\psi(T)|\psi_{target}\rangle|^2$ considering the Krotov-algorithm [65]. In table I, we present results for the infidelity $\mathcal{I}$ for all quantum gates required by the QPA considering two different pulse durations (T=1.0 and 1.3 ns). The infidelity in table I must be multiplied by 10^{-5} to get its real value, *i.e.*, for the U_{FT} the infidelity is 3.9×10^{-5} at T=1.3 ns, which corresponds to a fidelity of 0.999961. The worst case shown in table I is for the Π_5 gate considering a pulse of $T = 1$ ns, which has the infidelity $\mathcal{I} = 1414.7 \times 10^{-5}$ ($\mathcal{F} = 0.985853$) and we attribute such a result to the approach of the quantum speed limit. In general, the infidelity in table I decreases with the increasing of the pulse duration. Only for Π_1 the infidelity is bigger for T=1.3 ns than for T=1.0 ns. Such a result is due to numerical calculations and the convergence criteria, which was set to stop the TBQCP iterations when the infidelity starts to fluctuate within 20 iterations, *i.e.*, achieves a larger value of infidelity when compared to the infidelity evaluated 20 iterations before.

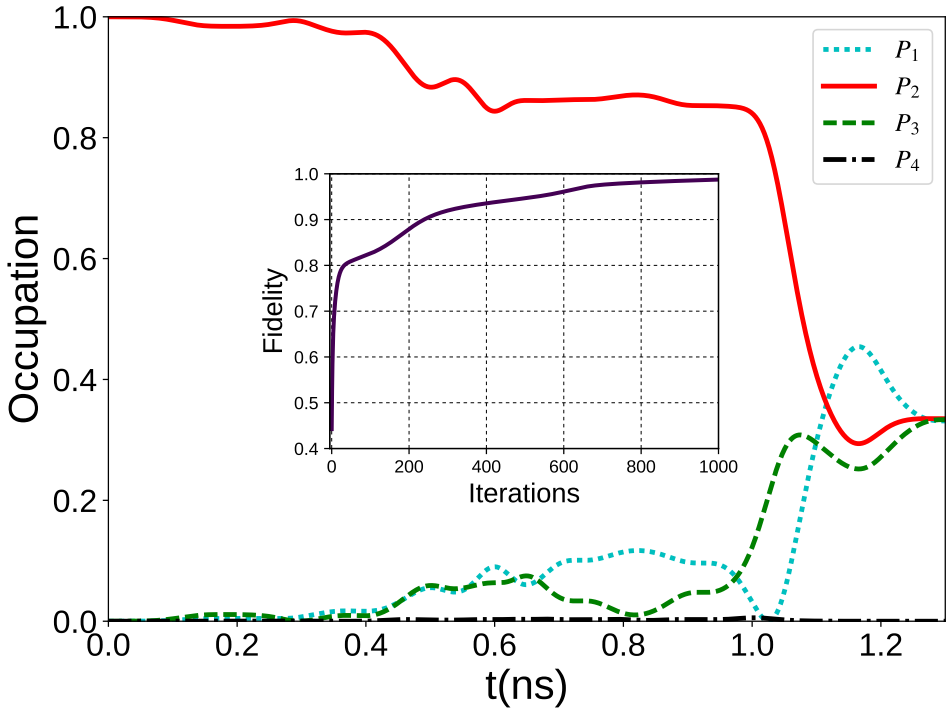

Figure 5.6: State occupations $P_i = |\langle\psi(t)|i\rangle|^2$ for i=1,2,3,4 as a function of time considering the action of the U_{FT} gate on the initial state $|2\rangle$ that converts it to the state $\frac{1}{\sqrt{3}}(|1\rangle + \exp(i2\pi/3)|2\rangle + \exp(-i2\pi/3)|3\rangle)$. The inset shows the fidelity, which increases with the number of iterations in the TBQCP method.

5.2.1 Performance under a noisy environment

Relaxation and decoherence sources are always present and are responsible for reducing coherence and fidelity of a quantum gate. To probe the influence of those effects on optimal fields, we model the charge noise as errors in the reference detuning over many cycles of measurements, which constitutes the final averaged measurement. We assume that these changes in the detuning follows a Gaussian distribution centered in $\varepsilon_0 = 50$ μeV. Thus, we consider an average over many cycles of the time evolution given by the non-optimal field $E(t) = \varepsilon_{opt}(t) - \varepsilon_0 - \varepsilon_R$, where $\varepsilon_{opt}(t)$ is the optimal pulse and ε_R is the error in the reference detuning. We plot the mean fidelity for the Π_3 gate as a function of the Gaussian width σ in Fig. (5.7), which shows that if there is a Gaussian spread of 50% on the detuning the mean fidelity decays 40%, but the fidelity is bigger than 0.95 if the spread is around 10%. Such results demonstrate that the optimal fields can achieve a good fidelity even though there is some intrinsic error in the experimental implementation of such fields. Our results are also very robust when dealing with changes in the values of Δ's in Eq. (5.7), for example, the fidelity decreases only 1% when there is an error of 10% in the value of Δ_1. The fidelity is even less affected by considering variations on other Δ's values.

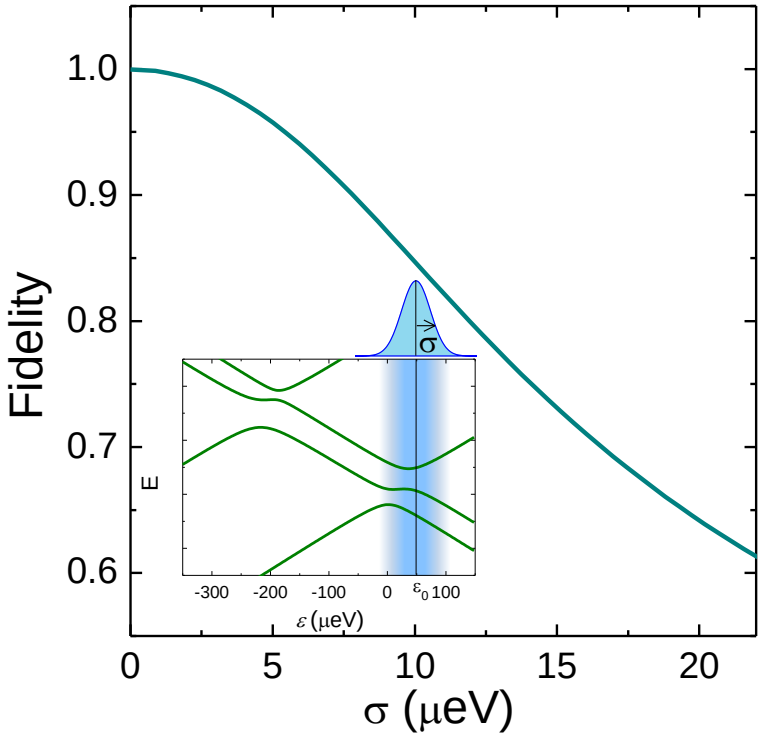

Figure 5.7: Mean fidelity of the Π_3 gate as a function of the Gaussian width. The inset shows schematically how the charge noise was considered, *i.e.*, as an average over a Gaussian distribution of the reference detuning ε_0.

5.3 Conclusions

In this chapter, we propose a physical realization of the quantum permutation algorithm (QPA) by using the platform of hybrid qubit in DQDs. We employ the TBQCP method to optimize electric pulses that drives the states of the system to the desired set of target states required by the QPA. These pulses perform the quantum gates of the QPA with a fidelity higher than 0.9997, when noise is not considered. Moreover, the short duration of our pulses (1.3 ns) compared to the decoherence time (20 ns) reported in ref. [37], support the idea that noise would not have significant effects on the performance of our implementation. We show that the high fidelity achieved in our simulation occurs when the pulse duration is above the quantum speed limit. Furthermore, the charge noise is modelled by considering an average over the optimal field centred at different values of the reference detuning, which follows a Gaussian distribution. The mean fidelity is still higher than 0.95 if the Gaussian spread is of the order of $5\mu eV$, which shows that the optimal field is robust if the error caused by the charge noise is small than such a value. The analysis and results of this chapter were published in the article [132].

Chapter 6

Conclusions and future perspectives

In this study, first we reviewed the one-qubit dynamics and offered a new unifying interpretation of the Landau-Zenner and the Rabi dynamics, by indicating the physical elements responsible for the manifestation of one phenomenon or the other, without the need to define them as separate phenomena.

Furthermore, we explore numerically the feasibility of quantum gates in two different platforms of quantum dots, with the assistance of the the two-point boundary-value quantum control paradigm (TBQCP) [126] (a numerical method of the optimal quantum control theory). In the first platform, consisting of a DQD embedded in a nanowire, we optimized single qubit pulses corresponding to three quantum gates assuring a fidelity for every gate higher than 0.99. We also compared the dynamical efficiency of the TBQCP respect to other dynamical mechanisms (Rabi and Landau-Zener); and we found that TBQCP can provide optimized pulses that can perform different tasks in a time as fast as possible. In the second platform of electrostatical DQD, we implemented a quantum algorithm the quantum permutation algorithm (QPA) [121], which requires quantum superposition of states with well-defined relative phases. Because of the necessity of using at least a three level system in this algorithm, we employed hybrid qubits instead of spin qubits. The implementation of the QPA required the optimization of eight electrical pulses corresponding to the different quantum gates, but the algorithm execution requires the application of three of these quantum gates in sequential order. In this case the fidelity of every gate is assured to be higher than 0.9997, at the quantum speed limit, and its performance was proven to be robust under reasonable noisy conditions as well. The duration of the optimized pulses for both platforms were significatively below the decoherence and relaxation times of the respective platforms.

Our results open the possibility of achieving all-electrical quantum gates in DQDs by means of optimal quantum control. Next we propose some future routes of our study.

Perspectives

Given that our numerical results confirm the feasibility of quantum gates in the platforms that we have studied, and the fact that the duration of the optimized pulses for both cases were below the decoherence and relaxation times; then an experimental implementation could be realized. Furthermore, it would be interesting to include the interaction with a system of many degrees of freedom to our models, in order to study the performance in the optimizations of the TBQCP method under the effects of decoherence.

It is known from ref. [137] that to the use of information units higher than the qubit simplifies the quantum circuits associated to the same quantum algorithm. Thus it would be interesting to rewrite the quantum circuits of known algorithms for qubits, to an equivalent in qutrits (or even qudit states), and then explore numerically its feasibility in any of the both platforms that we considered. This proposal is also relevant since the reduction in the number of operations, also reduce the adverse effects of computational errors or decoherence. A first step in this direction could be the simulation of a Toffoli gate for qutrits, since the combined action of the Toffoli and Hadamard gates allows the implementation of quantum universal computing.

Bibliography

[1] R. Feynman, "Simulating physics with computers" Int. J. Theor. Phys. **21** 467 (1982).

[2] L. K. Grover "A fast quantum mechanical algorithm for database search", in *Proc. 28th Annual ACM Symp. on the Theory of Computing* pp 212-9 (1996).

[3] P. W. Shor, "Polynomial-time algorithms for prime factorization and discrete logarithms on a quantum computer" SIAM J. Comput. **26** 1484 (1997).

[4] C. H. Bennett and G. Brassard, in *Proceedings of the IEEE International Conference on Computers, Systems and Signal Processing, Bangalore*, India IEEE, New York, 1984, pp. 175-179.

[5] Comercial services in quantum cryptography. Retrieved from http://www.idquantique.com/quantum-safe-crypto/

[6] J. A. Jones, M. Mosca, and R. H. Hansen, "Implementation of a quantum search algorithm on a quantum computer" Nature (London) **393**, 344 (1998).

[7] L. M. K. Vandersypen, *et. al.*, "Experimental realization of Shor's quantum factoring algorithm using nuclear magnetic resonance" Nature **414**, 883 (2001).

[8] S. Haroche, "Nobel lecture: controlling photons in a box and exploring the quantum to classical boundary", Rev. Mod. Phys. **85**, 1083 (2013).

[9] D. J. Wineland, "Nobel lecture: superposition, entanglement, and raising Schrödinger's cat", Rev. Mod. Phys. **85**, 1103 (2013).

[10] M. Saffman, T. G. Walker, and K. Mølmer, "Quantum information with Rydberg atoms" Rev. Mod. Phys. **82**, 2313 (2010).

[11] R. Hanson, O. Gywat, and D. D. Awschalom, "Room-temperature manipulation and decoherence of a single spin in diamond" Phys. Rev. B **74**, 161203(R) (2006).

[12] C. Monroe, D. M. Meekhof, B. E. King, W. M. Itano, and D. J. Wineland, Demonstration of a Fundamental Quantum Logic Gate, Phys. Rev. Lett. 75, 4714 (1995).

[13] A. Blais, R.-S. Huang, A. Wallraff, S. M. Girvin, and R. J. Schoelkopf, "Cavity quantum electrodynamics for superconducting electrical circuits: An architecture for quantum computation" Phys. Rev. A **69**, 062320 (2004).

[14] M. D. Lukin, "Colloquium: trapping and manipulating photon states in atomic ensembles", Rev. Mod. Phys. **75**, 457 (2003).

[15] T. Duty, D. Gunnarsson, K. Bladh, and P. Delsing, "Coherent dynamics of a Josephson charge qubit" Phys. Rev. B **69**, 140503 (2004).

[16] J. J. L. Morton, *et. al.*, "Solid-state quantum memory using the ^{31}P nuclear spin", Nature **455**, 1085 (2008).

[17] M. D. Barrett, *et. al.*, "Deterministic quantum teleportation of atomic qubits" Nature **429**, 737 (2004).

[18] D. P. DiVincenzo, "The Physical Implementation of Quantum Computation", Fortschr. Phys. **48**, 771 (2000).

[19] T. D. Ladd, F. Jelezko, R. Laflamme, Y. Nakamura, C. Monroe, and J. L. O'Brien, "Quantum computers", Nature **464** (7285), 45 (2010).

[20] A. D. Córcoles, *et. al.*, "Demonstration of a quantum error detection code using a square lattice of four superconducting qubits", Nat. Comm. **6**, 6979 (2015).

[21] E. Knill, "Quantum computing with realistically noisy devices", Nature **434**, 39 (2005).

[22] M. Mariantoni, *et. al.*, "Implementing the Quantum von Neumann Architecture with Superconducting Circuits", Science **334**, 6052 (2011).

[23] D. D. Awschalom, L. C. Bassett, A. S. Dzurak, E. L. Hu, J. R. Petta, "Quantum Spintronics: Engineering and Manipulating Atom-Like Spins in Semiconductors", Science **339**, 6124 (2013).

[24] B. M. Maune, *et. al.*, "Coherent singlet-triplet oscillations in a silicon-based double quantum dot", Nature **481**, 344 (2012).

[25] X. Li, *et. al.*, "An All-Optical Quantum Gate in a Semiconductor Quantum Dot", Science **301**, 5634 (2003).

[26] G. Burkard, D. Loss, and D. P. DiVincenzo, "Coupled quantum dots as quantum gates" Phys. Rev. B **59**, 2070 (1999).

[27] C. Kloeffel, D. Loss, "Prospects for spin-based quantum computing in quantum dots", Ann. Rev. Condens. Matter Phys. **4** (1), 51 (2013).

[28] A. V. Kuhlmann, *et. al.*, Nature Physics **9**, 570 (2013).

[29] J. H. Jefferson, M. Fearn, D. L. J. Tipton, and T. P. Spiller, Phys. Rev. A **66**, 042328 (2002).

[30] D. Loss and D. P. DiVincenzo, "Quantum computation with quantum dots" Phys. Rev. A **57**, 120 (1998).

[31] Kloeffel and D. Loss, Annu. Rev. condesed matter phys. 4, 51 (2013).

[32] Shi, Z. *et. al.*, Fast coherent manipulation of three-electron states in a double quantum dot. Nature Commun. **5**, 3020 (2014).

[33] Zhan Shi , C. B. Simmons, J. R. Prance, John King Gamble, Teck Seng Koh, Yun-Pil Shim, Xuedong Hu, D. E. Savage, M. G. Lagally, M. A. Eriksson, Mark Friesen, and S. N. Coppersmith, Phys. Rev. Lett. **108** , 140503 (2012).

[34] M. Veldhorst *et. al.*, Nature Nanotec. 9, 981 (2014)

[35] Teck Seng Koh, John King Gamble, Mark Friesen, M. A. Eriksson, and S. N. Coppersmith, "Pulse-Gated Quantum-Dot Hybrid Qubit", Phys. Rev. Lett. **109**, 250503 (2012).

[36] Cao *et. al.*, "Tunable Hybrid Qubit in a GaAs Double Quantum Dot", Phys. Rev. Lett. **116**, 086801 (2016).

[37] D. Kim, *et. al.*, "Microwave-driven coherent operation of a semiconductor quantum dot charge qubit", Nat. Nanotechnology **10**, 243 (2015).

[38] D. Kim, *et al.*, "Quantum control and process tomography of a semiconductor quantum dot hybrid qubit", Nature **511**, 70 (2014).

[39] Maximilian Russ and Guido Burkard, "Three-electron spin qubits", arXiv:1611.09106.

[40] Florian Dolde *et. al.*, Nature Commun. **5**, 3371 (2014).

[41] C. Lovecchio *et. al.*, "Quantum state reconstruction on atom-chips", Phys. Rev. A **93**, 010304(R) (2016).

[42] F. Motzoi, J. M. Gambetta, P. Rebentrost, and F. K. Wilhelm, Phys. Rev. Lett. **103**, 110501 (2009).

[43] E. Zahedinejad, J. Ghosh, and B. C. Sanders, "High-Fidelity Single-Shot Toffoli Gate via Quantum Control", Phys. Rev. Lett. **114**, 200502 (2015).

[44] C. H. Bennett, *et. al.*, "Teleporting an unknown quantum state via dual classical and Einstein-Podolsky-Rosen channels", Phys. Rev. Lett. **70**, 1895, (1993).

[45] C. H. Bennett, "Quantum cryptography using any two nonorthogonal states", Phys. Rev. Lett. **68**, 3121, (1992).

[46] , G. Grynberg, A. Aspect, and C. Fabre, *Introduction to Quantum Optics*, (Cambridge University Press, Cambridge, England, 2010).

[47] J. H. Shirley, "Solution of the Schrödinger Equation with a Hamiltonian Periodic in Time", Phys. Rev. **138**, B979 (1965).

[48] G. Benenti, G. Casati and G. Strini, *Principles of Quantum Computation and Information*, Vol. 1, (World Scientific Publishing, Singapore 2004).

[49] C. Cohen-Tannoudji, B. Diu, F. Laloe, *Quantum mechanics*, vol. 1, (1977).

[50] C. Zener, "Non-adiabatic crossing of energy levels", Proc. R. Soc. A **137**, 833, (1932).

[51] L. Landau, "Zur Theorie der Energieübertragung", Physics of the Soviet Union **2**, 46 (1932).

[52] E. Majorana, "Atomi orientati in campo magnetico variabile", Il Nuovo Cimento (1924-1942) **9**, 43 (1932).

[53] E. Stückelberg, Helvetica Physica Acta **5**, 370 (1932).

[54] F. D. Giacomo and E. E. Nikitin, "The Majorana formula and the Landau-Zener-Stuckelberg treatment of the avoided crossing problem", Physics-Uspekhi **48**, 515 (2005).

[55] S. Shevchenko, S. Ashhab, and F. Nori, "Landau-Zener-Stückelberg interferometry", Physics Reports **492**, 1 (2010).

[56] D. J. Griffiths, *Introduction to Quantum Mechanics (2nd Edition)*, (Pearson Prentice Hall, London, 2005).

[57] Milton Abramowitz and Irene A. Stegun, *Handbook of mathematical functions: with formulas, graphs, and mathematical tables*, (volume 55. Courier Corporation, 1964).

[58] S. Ashhab, J. R. Johansson, A. M. Zagoskin, and F. Nori, "Two-level systems driven by large-amplitude fields", Phys. Rev. A **75**, 063414, (2007).

[59] M. A. Nielsen and I. L. Chuang, *Quantum Computation and Quantum Information* (Cambridge University Press, Cambridge, England, 2000).

[60] T.-S. Ho and H. Rabitz, "Accelerated monotonic convergence of optimal control over quantum dynamics" Phys. Rev. E **82**, 026703 (2010).

[61] S. Deffner and S. Campbell, "Quantum speed limits: from Heisenberg's uncertainty principle to optimal quantum control", J. Phys. A: Math. Theor. **50**, 453001 (2017).

[62] L. Mandelstam and I. Tamm, J. Phys. (USSR) **9**, 249 (1945).

[63] P. Pfeifer and J. Fröhlich, Rev. Mod. Phys. **67**, 759 (1995).

[64] T. Caneva, M. Murphy, T. Calarco, R. Fazio, S. Montangero, V. Giovannetti, and G. E. Santoro, "Optimal Control at the Quantum Speed Limit", Phys. Rev. Lett. **103**, 240501 (2009).

[65] V. F. Krotov, Global Methods in Optimal Control Theory (Marcel Dekker, New York, 1996).

[66] A. del Campo, I. L. Egusquiza, M. B. Plenio, and S. F. Huelga, "Quantum Speed Limits in Open System Dynamics", Phys. Rev. Lett. **110**, 050403 (2013).

[67] F. C. Binder, *et al.*, "Quantacell: powerful charging of quantum batteries", New J. Phys. **17**, 075015 (2015).

[68] F. Campaioli, *et al.*, "Speeding Up Battery Charging with Quantum Physics", Phys. Rev. Lett. **118**, 150601 (2017).

[69] C. Brif, R. Chakrabarti and H. Rabitz, "Control of quantum phenomena: past, present and future", New Journal of Physics. **12**, 075008 (2010).

[70] M. Shapiro, J. W. Hepburn and P. Brumer, "Simplified laser control of unimolecular reactions: Simultaneous (ω_1, ω_3) excitation", Chemical Physics Letters. **149**, 451 (1988).

[71] A. Assion *et al.*, "Control of Chemical Reactions by Feedback-Optimized Phase-Shaped Femtosecond Laser Pulses", Chemical Physics Letters. **282**, 5390 (1998).

[72] K. Bergmann, H. Theuer, and B. W. Shore, "Coherent population transfer among quantum states of atoms and molecules", Rev. Mod. Phys. **70**, 1003 (1998).

[73] J. A. Cina, "Wave-Packet Interferometry and Molecular State Reconstruction: Spectroscopic Adventures on the Left-Hand Side of the Schrödinger Equation", Ann. Rev. Phys. Chem., **59**, 319 (2008).

[74] S. Kotochigova, "Prospects for Making Polar Molecules with Microwave Fields", Chem. Phys. Lett., **99**, 073003 (2007).

[75] C. P. Koch, and M. Shapiro, "Coherent Control of Ultracold Photoassociation", Chem. Rev. **112, 9** 4949 (2012).

[76] L. Levin, *et al.*, "Coherent Control of Bond Making", Phys. Rev. A, **114**, 233003 (2015).

[77] E. F. de Lima, "Coherent control of the formation of cold heteronuclear molecules by photoassociation", Phys. Rev. A, **95**, 013411 (2017).

[78] S. M. Rochester, *et al.*, "Efficient polarization of high-angular-momentum systems", Phys. Rev. A, **94**, 043416 (2016).

[79] C. G. Yale, "Optical manipulation of the Berry phase in a solid-state spin qubit", nat. photonics, **10**, 184-189 (2016).

[80] A. M. D. Thomasen and T. Byrnes, "STIRAP schemes for atomic Bose-Einstein condensates", J. Phys.: Conf. Ser. **752**, 012004 (2016).

[81] A. P. Hope, *et al.*, "Adiabatic two-photon quantum gate operations using a long-range photonic bus", J. Phys. B: At. Mol. Opt. Phys. **48**, 055503 (2015).

[82] B. Rousseaux, S. Guérin, and N. V. Vitanov, "Arbitrary qudit gates by adiabatic passage", Phys. Rev. A, **87**, 032328 (2013).

[83] S. Shi, A. Woody, and H. Rabitz, "Optimal control of selective vibrational excitation in harmonic linear chain molecules", J. Chem. Phys., **88**, 6870 (1988).

[84] A. P. Peirce, M. A. Dahleh and H. Rabitz, "Optimal control of quantum-mechanical systems: Existence, numerical approximation, and applications", Phys. Rev. A, **37**, 12 (1988).

[85] R. Kosloff, S. A. Rice, P. Gaspard, S. Tersigni and D. J. Tannor, "Wavepacket dancing: Achieving chemical selectivity by shaping light pulses", Chem. Phys., **139**, (1989).

[86] S. Shi and H. Rabitz, "Selective excitation in harmonic molecular systems by optimally designed fields", **13**, 1 (1989).

[87] W. Jakubetz , J. Manz and H. J. Schreier, "Theory of optimal laser pulses for selective transitions between molecular eigenstates", Chem. Phys. Lett., **139**, 1 (1990).

[88] R. J. Gordon and S. A. Rice, "Active control of the dynamics of atoms and molecules", **48**, 601 - 641 (1997).

[89] M. D. Grace, J. Dominy, R. L. Kosut, C. Brif and H. Rabitz, "Environment-invariant measure of distance between evolutions of an open quantum system", New J. Phys., **12**, 015001 (2010).

[90] T. Schulte-Herbrüggen, A. Spörl, N. Khaneja and S. J. Glaser, "Optimal control for generating quantum gates in open dissipative systems", J. Phys. B., **44**, 15 (2011).

[91] L. K. Castelano, E. F. de Lima, J. R. Madureira, M. H. Degani, and M. Z. Maialle, "Optimal control of universal quantum gates in a double quantum dot", Phys. Rev. B **97**, 235301 (2018).

[92] M. Melz, J. Wätzel, L. Chotorlishvili, and J. Berakdar, "Electrically tunable entanglement of an interacting electron pair in a spin-active double quantum dot", Phys. Rev. B **98**, 104407 (2018).

[93] A. Putaja and E. Räsänen, Ultrafast sequential charge transfer in a double quantum dot, Phys. Rev. B **82**, 165336 (2010).

[94] E. Torrontegui, *et al.*, "Fast transport of Bose-Einstein condensates", New Journal of Physics. **14**, 013031 (2012).

[95] Q. Zhang, *et al.*, "Optimal shortcuts for atomic transport in anharmonic traps", J. Phys. B: At. Mol. Opt. Phys. **49**, 125503 (2016).

[96] X. Chen, *et al.*, "Optimal trajectories for efficient atomic transport without final excitation", Phys. Rev. A **84**, 043415 (2011).

[97] A. M. Weiner, "Femtosecond pulse shaping using spatial light modulators", Rev. Sci. Instrum. **71**, 1929 (2000).

[98] N. Khaneja, *et al.*, "Optimal control of coupled spin dynamics: design of NMR pulse sequences by gradient ascent algorithms", J. Magn. Reson. **172**, 2 (2005).

[99] C. A. Ryan, C. Negrevergne, M. Laforest, E. Knill, and R. Laflamme, "Liquid-state nuclear magnetic resonance as a testbed for developing quantum control methods", Phys. Rev. A **78**, 012328 (2008).

[100] B. A. Rodin, *et al.*, "Using optimal control methods with constraints to generate singlet states in NMR", J. Magn. Reson. **291**, 14-22 (2018).

[101] J. A. Jones, "Quantum computing with NMR", Prog. NMR Spectrosc. **59**, 91 (2011).

[102] G. Passante, O. Moussa and R. Laflamme, "Measuring geometric quantum discord using one bit of quantum information", Phys. Rev. A **85**, 032325 (2012).

[103] J. Guo, *et al.*, "High-performance Raman quantum memory with optimal control in room temperature atoms", Nature Communications **10**, 148 (2019).

[104] S. van Frank, *et al.*, "Optimal control of complex atomic quantum systems", Scientific Reports **6**, 34187 (2016).

[105] S. Amri, *et al.*, "Optimal control of the transport of Bose-Einstein condensates with atom chips", Scientific Reports **9**, 5346 (2019).

[106] L. R. Schreiber and H. Bluhm, "Silicon comes back", Nat. Nanotechnology **9**, 966-968 (2014).

[107] E. Kawakami, *et al.*, "Electrical control of a long-lived spin qubit in a Si/SiGe quantum dot", Nat. Nanotechnology **9**, 666-670 (2014).

[108] J. T. Muhonen, *et al.*, "Storing quantum information for 30 seconds in a nanoelectronic device", Nat. Nanotechnology **9**, 986-991 (2014).

[109] Y. He, *et al.*, "A two-qubit gate between phosphorus donor electrons in silicon", Nature **571**, 371-375 (2019).

[110] J. Yoneda, *et al.*, "A quantum-dot spin qubit with coherence limited by charge noise and fidelity higher than 99.9%", Nat. Nano., **13**, 102-106 (2018).

[111] S.-L. Liao, T.-S. Ho, S.-I Chu and H. Rabitz, "Fast-kick-off monotonically convergent algorithm for searching optimal control fields", **84**, 031401 (2011).

[112] V. N. Golovach, M. Borhani, and D. Loss, "Electric-dipole-induced spin resonance in quantum dots", Phys. Rev. B **74**, 165319 (2006).

[113] M. P. Nowak, B. Szafran, and F. M. Peeters, "Resonant harmonic generation and collective spin rotations in electrically driven quantum dots", Phys. Rev. B **86**, 125428 (2012).

[114] K. C. Nowack, F. H. L. Koppens, Y. V. Nazarov, and L. M. K. Vandersypen, "Coherent Control of a Single Electron Spin with Electric Fields", Science **318**, 1430 (2007).

[115] J. C. Mason and D. C. Handscomb, *Chebyshev Polynomials* (Chapman and Hall/CRC, England, 2002).

[116] S. Nadj-Perge, S. M. Frolov, E. P. A. M. Bakkers, and L. P. Kouwenhoven, "Spin-orbit qubit in a semiconductor nanowire", Nature **468**, 1084 (2010).

[117] Florian Dolde *et. al.*, Nature Commun. **5**, 3371 (2014).

[118] C. Lovecchio, *et. al.*, "Optimal preparation of quantum states on an atom-chip device", Phys. Rev. A **93**, 010304(R) (2016).

[119] F. Motzoi, J. M. Gambetta, P. Rebentrost, and F. K. Wilhelm, Phys. Rev. Lett. **103**, 110501 (2009).

[120] E. Zahedinejad, J. Ghosh, and B. C. Sanders, Phys. Rev. Lett. **114**, 200502 (2015).

[121] Z. Gedik, I. A. Silva, B. Çakmak, G. Karpat, E. L. G. Vidoto, D. O. Soares-Pinto, E. R. deAzevedo & F. F. Fanchini, "Computational speed-up with a single qudit", Scientific reports **5**, 14671, (2015).

[122] C. M. Tesch and de R. Vivie-Riedle, J. Chem. Phys. **121**, 24 (2004).

[123] S. Nadj-Perge *et al.*, Nature 468, 1084 (2010).

[124] M. D. Schroer, K.D. Petersson, M. Jung, J.R. Petta, PRL 107, 176811 (2011).

[125] J. Stehlik, M. D. Schroer, M. Z. Maialle, M. H. Degani, J. R. Petta, Phys. Rev. Lett. **112**, 227601 (2014).

[126] T.-S. Ho and H. Rabitz, "Accelerated monotonic convergence of optimal control over quantum dynamics", Phys. Rev. E **82**, 026703 (2010).

[127] C. M. Tesch and de R. Vivie-Riedle, J. Chem. Phys. **121**, 24 (2004).

[128] J. P. Palao and R. Kosloff, Phys. Rev. A **68**, 062308 (2003).

[129] J. R. Petta, A. C. Johnson, C. M. Marcus, M. P. Hanson, and A. C. Gossard, PRL 93, 186802 (2004).

[130] Samuel P. Benz and Steven B. Waltman, "Pulse-bias electronics and techniques for a Josephson arbitrary waveform synthesizer", IEEE Transactions on Applied Superconductivity **24**, (2014).

[131] Gerhard C. Hegerfeldt Phys. Rev. Lett. **111**, 260501 (2013).

[132] C. M. Rivera-Ruiz, E. F. de Lima, F. F. Fanchini, V. Lopez-Richard, and L. K. Castelano, "Optimal control of hybrid qubits: Implementing the quantum permutation algorithm", Phys. Rev. A **97**, 032332 (2018).

[133] J. J. Sakurai and J. J. Napolitano, *Modern Quantum Mechanics (2nd Edition)*, (Addison Wesley Longman, New York, 2010).

[134] S. Barnett, *Quantum Information (Oxford Master Series in Physics: Atomic, Optical, and Laser Physics)*, (Oxford University Press, New York, 2009).

[135] J. A. Bergou, "Discrimination of quantum states", J. Mod. Opt. **57**, 160, (2010).

[136] H. M. Wiseman and G. J. Milburn, *Quantum Measurement and Control*, (Cambridge University Press, Cambridge, England, 2009).

[137] B. P. Lanyon, M. Barbieri, M. P. Almeida, *et. al.*, "Simplifying quantum logic using higher dimensional Hilbert spaces", Nat. Phys. **5**, 134 (2009).

Appendix A

Rotating Wave Approximation

In this appendix we specify the mathematical steps behind the rotating wave approximation (RWA), applied in chapter 2.

The hamiltonian of a two-level system under a driving field can be described as (we take $\hbar = 1$ for this example)

$$H = \frac{\Delta}{2}\sigma_Z + \frac{\epsilon(t)}{2}\sigma_X, \tag{A.1}$$

with a time-dependent field described by $\epsilon(t) = A\sin(\omega_0 t)$, and system energies $E_1 = -\Delta/2$ and $E_2 = \Delta/2$ associated to the $|0\rangle$ and $|1\rangle$ states, respectively. With these states we can expand the time-dependent state $|\psi(t)\rangle$ at any time.

$$|\psi(t)\rangle = c_1(t)|0\rangle + c_2(t)|1\rangle. \tag{A.2}$$

With such state in the time-dependent Schrödinger equation we have,

$$i\frac{\partial}{\partial t}c_1(t) = E_1 c_1(t) + \frac{A}{2}\sin(\omega_0 t)c_2(t), \tag{A.3}$$

$$i\frac{\partial}{\partial t}c_2(t) = E_2 c_2(t) + \frac{A}{2}\sin(\omega_0 t)c_1(t). \tag{A.4}$$

This differential equation system has no analytical solution, but an aproximate solution can be found by implementing two mathematical substitutions,

$$\begin{aligned} b_1 &= c_1, \\ b_2 &= c_2 \exp(i\omega_0 t). \end{aligned} \tag{A.5}$$

Also, remembering that

$$\sin(\omega_0 t) = \frac{\exp(i\omega_0 t) - \exp(-i\omega_0 t)}{2i} = \frac{\exp(2i\omega_0 t) - 1}{2i\exp(i\omega_0 t)},$$

and appliying this identity in eq. A.3, we obtain,

$$
\begin{aligned}
i\frac{\partial}{\partial t}b_1(t) &= E_1 b_1(t) + \frac{A}{2}\sin(\omega_0 t) b_2(t)\exp(-i\omega_0 t),\\
i\frac{\partial}{\partial t}b_1(t) &= E_1 b_1(t) + \frac{A}{2}\frac{\exp(2i\omega_0 t)-1}{2i\exp(i\omega_0 t)} b_2(t)\exp(-i\omega_0 t) = E_1 b_1(t) + \frac{A}{4i}\frac{\exp(2i\omega_0 t)-1}{\exp(2i\omega_0 t)} b_2(t),\\
i\frac{\partial}{\partial t}b_1(t) &= E_1 b_1(t) - \frac{iA}{4}\left(1-\exp(-2i\omega_0 t)\right) b_2(t).
\end{aligned}
$$

Neglecting $2\omega_0$ terms, and with $\omega_u = E_1$ the frequency of the $|0\rangle$ state.

$$
i\frac{\partial}{\partial t}b_1(t) = \omega_u b_1(t) - \frac{iA}{4} b_2(t). \tag{A.6}
$$

For eq. A.4 and keeping in mind that $\dot{c}_2(t) = \dot{b}_2(t)\exp(-i\omega_0 t) - i\omega_0 b_2(t)\exp(-i\omega_0 t)$, we have:

$$
\begin{aligned}
i\hbar\left(\frac{\partial}{\partial t}b_2(t) - i\omega_0 b_2(t)\right)\exp(-i\omega_0 t) &= E_2 b_2(t)\exp(-i\omega_0 t) + \frac{A}{2}\frac{\exp(2i\omega_0 t)-1}{2i\exp(i\omega_0 t)} b_1(t),\\
\hbar\left(i\frac{\partial}{\partial t}b_2(t) + \omega_0 b_2(t)\right) &= E_2 b_2(t) + \frac{A}{4i}\left(\exp(2i\omega_0 t)-1\right) b_1(t),
\end{aligned}
$$

with $\omega_d = E_2$ as the frequency of the $|1\rangle$ state $\omega_d = \Delta/2$,

$$
i\frac{\partial}{\partial t}b_2(t) = \left(\omega_d - \omega_0\right) b_2(t) + \frac{iA}{4}\left(1-\exp(-2i\omega_0 t)\right) b_1(t).
$$

Neglecting $2\omega_0$ terms,

$$
i\frac{\partial}{\partial t}b_2(t) = \left(\omega_d - \omega_0\right) b_2(t) + \frac{iA}{4\hbar} b_1(t). \tag{A.7}
$$

Equations A.6, and A.7 constitute the RWA for our system.

The differential equation system (equations A.6 and A.7) has time-independent coefficients, therefore we can rewrite the equation system as the following eigenvalue problem:

$$
i\frac{\partial}{\partial t}|\tilde{\psi}(t)\rangle = \tilde{H}|\tilde{\psi}(t)\rangle, \tag{A.8}
$$

where

$$
\tilde{H} = \begin{pmatrix} \Delta/2 & -\frac{iA}{4} \\ \frac{iA}{4} & (\Delta/2 - \omega_0) \end{pmatrix},
$$

describes the interaction of the spin with a field, that is static in the time-dependent frame adapted when we applied the transformation in equations A.5.

After solving the eigenvalue problem, we get the eigenvalues of $\tilde{H}$

$$\tilde{E}_1 = \frac{1}{4}\left(-2\omega_0 - \sqrt{A^2 + 4(\omega_0 - \Delta)^2}\right),$$
$$\tilde{E}_2 = \frac{1}{4}\left(-2\omega_0 + \sqrt{A^2 + 4(\omega_0 - \Delta)^2}\right),$$

and the eigenvectors

$$|\tilde{\phi}_1\rangle = \begin{pmatrix} -\frac{i\left(2\omega_0 + 2\Delta - \sqrt{A^2+4(\omega_0-\Delta)^2}\right)}{A} \\ 1 \end{pmatrix},$$
$$|\tilde{\phi}_2\rangle = \begin{pmatrix} -\frac{i\left(2\omega_0 + 2\Delta + \sqrt{A^2+4(\omega_0-\Delta)^2}\right)}{A} \\ 1 \end{pmatrix}.$$

If we solve the time-dependent Schrödinger equation for a Hamiltonian $\tilde{H}$, that does not depent explicitly on time, then we can expand the state of the system at any time $|\psi(t)\rangle$, in terms of these eigenvectors and eigenvalues, such that

$$|\tilde{\psi}(t)\rangle = \alpha_1 \exp\left(-i\tilde{E}_1 t\right)|\tilde{\phi}_1\rangle + \alpha_2 \exp\left(-i\tilde{E}_2 t\right)|\tilde{\phi}_2\rangle, \tag{A.9}$$

with α_1 and α_2, to be determined using the initial condition $|\tilde{\psi}(0)\rangle$ for A.9.

For example, if our initial condition is $|\psi(0)\rangle = |0\rangle$, represented in the basis of S_z, then the transformation in A.5 gives the components in the new frame:

$$|\tilde{\psi}(0)\rangle = \begin{pmatrix} 1 \\ 0 \end{pmatrix},$$

and replacing it in A.9,

$$|\tilde{\psi}(0)\rangle = \alpha_1|\tilde{\phi}_1\rangle + \alpha_2|\tilde{\phi}_2\rangle,$$

$$\begin{pmatrix} 1 \\ 0 \end{pmatrix} = \alpha_1|\tilde{\phi}_1\rangle + \alpha_2|\tilde{\phi}_2\rangle,$$

which correspond to a two equation system of α_1 and α_2. By solving it and replacing α_1 and α_2 back in A.9, we obtain the state in any time $|\tilde{\psi}(t)\rangle$. Finally, we can find the probability $P_1(t)$ of finding the state $|1\rangle$

$$P_1(t) = \left|\langle 1|\tilde{\psi}(t)\rangle\right|^2 = \frac{A^2}{A^2 + 4(\omega_0 - \Delta)^2}\sin^2\left[\sqrt{A^2 + 4(\omega_0 - \Delta)^2}\frac{t}{4}\right].$$

From this expression, we can infer the Rabi frequency of our system, which correspond to

$$\Omega_R = \frac{1}{4}\sqrt{A^2 + 4(\omega_0 - \Delta)^2}.$$

Appendix B

Two-point Boundary-value Quantum Control Paradigm

A relevant problem in the theory of optimal control involves the identification of time-dependent control fields by iterative optimization methods. In quantum mechanics, one of this methods is the TBQCP (two-point boundary-value quantum control paradigm), see Ref. [126]. The purpose of this method is to tailor an optimal field in a quantum system to induce a temporal evolution from an initial (prepared) state $|\psi(0)\rangle$ to a final state $|\psi(T)\rangle$, which expected value coincides (with a required precision) with a predetermined value of the expected value of an observable of our interest $\langle O(T)\rangle$. In other words, the final state $|\psi(T)\rangle$, after the action of the optimized field, satisfies

$$\langle O(T)\rangle \approx \langle \psi(T) | O(T) | \psi(T)\rangle .$$

In this appendix, we show how this can be achieved with the TBQCP method, introduced briefly in chapter 3, and applied to optimize the electric fields in the physical platforms of chapters 4 and 5.

B.1 Formulation of the method

The temporal evolution of a quantum system represented by a wave function $|\psi_f(t)\rangle$ is described by the time-dependent Schrödinger equation

$$\frac{\partial}{\partial t}|\psi_f(t)\rangle = \frac{1}{i\hbar}\{H_0 - \mu E(t)\}|\psi(t)\rangle. \tag{B.1}$$

In our study, where interactions are mediated by the dipole operator, we can regard H_0 as the time-independent Hamiltonian free of time variable electric field; and μ as the dipole momentum operator.

The evolution operator U is

$$|\psi_f(t)\rangle = U(t,0)|\psi_f(0)\rangle. \tag{B.2}$$

Equation (B.1) can be rewritten as the Schrödinger equation for the evolution operator as [133]

$$\frac{\partial}{\partial t}U(t,0) = \frac{1}{i\hbar}\left\{H_0 - \mu E(t)\right\}U(t,0), \quad U(0,0) = \boldsymbol{I}. \tag{B.3}$$

The expectation value is defined as

$$\langle \mathcal{O}(t)\rangle \equiv \langle \psi(t)\,|\mathcal{O}(t)|\,\psi(t)\rangle\,, \tag{B.4}$$

with $\mathcal{O}(t)$ a positive semi-definite explicitly time-dependent invariant, which implies that $\langle \mathcal{O}(t)\rangle \geq 0$, $d\mathcal{O}(t)/dt = 0$ and $\mathcal{O}^{\dagger}(t) = \mathcal{O}(t)\ \forall t \in [0,T]$.

If we start from the initial state $|\psi_f(0)\rangle$, the evolution under a given field $E(t)$ ends at a given final state $|\psi_f(T)\rangle$.

Now if we define an invariant with the desired value of an observable, and since it does not change in time, then

$$\frac{d\mathcal{O}(t)}{dt} \equiv \frac{\partial}{\partial t}\mathcal{O}(t) + \frac{1}{i\hbar}\left[\mathcal{O}(t),\, H_0 - \mu E^{(0)}(t)\right] = 0, \text{ and } \mathcal{O}(T) = O_T, \tag{B.5}$$

with $E^{(0)}$ a reference field, and $O_T \equiv |\psi_t\rangle\langle\psi_t|$ a projector on a target state $|\psi_t\rangle$ of our interest, such that in eq. (B.5) the last condition $\mathcal{O}(T) = O_T$, requires that the operator $\mathcal{O}(T)$ coincides at the final time $t = T$, with the projector O_T of the target state. In order to satisfy such invariance in the observable we suppose the existence of a reference field $E^{(0)}(t)$ that guarantees such condition.

From eq. (B.5), the dynamical evolution of the observable and invariant $\mathcal{O}(t)$ can be described as

$$\mathcal{O}(t) = U_0(t,T)O_T U_0^{\dagger}(t,T), \tag{B.6}$$

with $U_0(t,T)$ corresponding to a backward propagator in time (which propagates the state $|\psi_b(T)\rangle$ from the final time T to a time before it t), i.e.,

$$|\psi^{(0)}(t)\rangle = U_0(t,T)|\psi_b(T)\rangle. \tag{B.7}$$

Its respective time evolution Schrödinger equation is

$$\frac{\partial}{\partial t}U_0(t,T) = \frac{1}{i\hbar}\left\{H_0 - \mu E^{(0)}(t)\right\}U_0(t,T), \quad U_0(T,T) = \boldsymbol{I}. \tag{B.8}$$

Since these evolution operators are unitary, they satisfy $U_0^{\dagger}(t,T)U_0(t,T) = \boldsymbol{I}$, and it is also true that

$$U_0(T,T) = U_0(T,t)U_0(t,T) = \boldsymbol{I},$$

therefore $U_0^\dagger(t,T) = U_0(T,t)$. From the definition in eq. (B.7) $U_0^\dagger(t,T)|\psi^{(0)}(t)\rangle = U_0(T,t)|\psi_b^{(0)}(t)\rangle$.

Now from the definition of expected value in eq. (B.4), the fact that $|\psi_b^{(0)}(t)\rangle = U_0(t,0)|\psi_b(0)\rangle$, and applying the respective equivalents for the complex conjugate operators, we have that

$$\begin{aligned}\left\langle \psi_b^{(0)}(t)|\mathcal{O}(t)|\psi_b^{(0)}(t)\right\rangle =&\langle\psi_b^{(0)}(t)|U_0(t,T)O_T U_O(T,t)|\psi_b^{(0)}(t)\rangle,\\ =&\langle\psi_b(0)|U_0^\dagger(t,0)U_0(t,T)\mathcal{O}(T)U_0^\dagger(t,T)U_0(t,0)|\psi_b(0)\rangle,\\ =&\langle\psi_b(0)|U_0(0,t)U_0(t,T)\mathcal{O}(T)U_0(T,t)U_0(t,0)|\psi_b(0)\rangle,\\ =&\langle\psi_b(0)|U_0(0,T)\mathcal{O}(T)U_0(T,0)|\psi_b(0)\rangle,\end{aligned}$$

and from eq. (B.6) with $t = 0$

$$\begin{aligned}=&\langle\psi_b(0)|U_0(0,T)\mathcal{O}(T)U_O^\dagger(0,T)|\psi_b(0)\rangle,\\ \left\langle \psi_b^{(0)}(t)|\mathcal{O}(t)|\psi_b^{(0)}(t)\right\rangle =&\langle\psi_b(0)|\mathcal{O}(0))|\psi_b(0)\rangle.\end{aligned} \tag{B.9}$$

This means it is time independent, i.e.,

$$\frac{d}{dt}\left\langle \psi_b^{(0)}(t)\left|\mathcal{O}(t)\right|\psi_b^{(0)}(t)\right\rangle = 0.$$

Derivating equation eq. (B.4) (for the forward evoluted states), we obtain the Heisenberg equation of motion

$$\frac{d}{dt}\langle\mathcal{O}(t)\rangle = \frac{d}{dt}\left(\langle\psi_f(t)\left|\mathcal{O}(t)\right|\psi_f(t)\rangle\right), \tag{B.10}$$

by the chain rule of derivation, this yield three terms

$$\frac{d}{dt}\langle\mathcal{O}(t)\rangle = \left(\frac{d}{dt}\langle\psi_f(t)|\right)\mathcal{O}(T)|\psi_f(t)\rangle + \langle\psi_f(t)|\left(\frac{d}{dt}\mathcal{O}(T)\right)|\psi_f(t)\rangle + \langle\psi_f(t)|\mathcal{O}(T)\left(\frac{d}{dt}|\psi_f(t)\rangle\right),$$

where the derivate in the last term is the eq. (B.1), and the derivate in the first corresponds to the complex conjugate of the same eq. (B.1). Considering the complete expressions, the first and third term cancel each other. On the other hand, the derivative of the second term is similar to eq. (B.4), but with the control field $E(t)$

$$\frac{d\mathcal{O}(t)}{dt} = \frac{\partial}{\partial t}\mathcal{O}(t) + \frac{1}{i\hbar}\left\{\mathcal{O}(t)H_0(t) - \mathcal{O}(t)\mu E(t) + \mu E(t)\mathcal{O}(t) - H_0(t)\mathcal{O}(t)\right\},$$

which can be expressed as the sum of two factored commutators. Then the derivate of the expected value is

$$\frac{d\langle\mathcal{O}(t)\rangle}{dt} = \left\langle \psi_f(t) \left| -\frac{1}{i\hbar}\left[H_0,\, \mathcal{O}(t)\right] + \frac{\partial\mathcal{O}(t)}{\partial t} \right| \psi_f(t) \right\rangle + \left\langle \psi_f(t) \left| \frac{1}{i\hbar}\left[\mu,\, \mathcal{O}(t)\right] \right| \psi_f(t) \right\rangle E(t). \tag{B.11}$$

If we calculate the expected value in the eq. (B.5), with $|\psi_b^{(0)}(t)\rangle$, as it is zero from the invariant in eq. (B.10), then we can subtract it from eq. (B.11), to obtain the following expression

$$\frac{d\langle\mathcal{O}(t)\rangle}{dt} = f_\mu(t)\left\{E(t) - E^{(0)}(t)\right\}, \tag{B.12}$$

with

$$f_\mu(t) = \left\langle \psi_f(t) \left| \frac{1}{i\hbar}\left[\mu,\, \mathcal{O}(t)\right] \right| \psi_f(t) \right\rangle = -\frac{2}{\hbar}\mathrm{Im}\left\{\langle\psi_f(t)\left|\mathcal{O}(t)\mu\right|\psi_f(t)\rangle\right\}, \tag{B.13}$$

which corresponds to a functional of the control field $E(t)$ and the reference field $E^{(0)}(t)$.

Now the integration of eq. (B.11), yields

$$\langle\mathcal{O}(T)\rangle - \langle\mathcal{O}(0)\rangle = \int_0^T f_\mu(t)\left\{E(t) - E^{(0)}(t)\right\}dt, \tag{B.14}$$

where $\langle\mathcal{O}(T)\rangle = \langle\psi_f(T)\left|\mathcal{O}(T)\right|\psi_f(T)\rangle = \langle\psi_f(0)\left|U(0,T)\mathcal{O}(T)U(T,0)\right|\psi_f(0)\rangle$ is a functional of the control field $E(t)$ and $\langle\mathcal{O}(0)\rangle = \langle\psi_f(0)\left|\mathcal{O}(0)\right|\psi_f(0)\rangle$

$= \langle\psi_f(0)\left|U_0(0,T)\mathcal{O}(T)U_0(T,0)\right|\psi_f(0)\rangle$ a functional of the reference field $E^{(0)}(t)$.

B.1.1 Iterative equations of the TBQCP method

Equations (B.1), (B.5) and (B.14) constitute the essence of the TBQCP method. In order to compute the optimal field $E(t)$, we use those three equations, an arbitrary initial reference field $E^{(0)}(t)$, and two boundary conditions: $|\psi_f(0)\rangle$ representing an initial chosen state at $t = 0$ which is propagated forward with eq. (B.1). The second initial condition at the final time $t = T$ corresponds to the target state $|\psi_b(T)\rangle = |\psi_t\rangle$, and allow us to construct the projector $O_T \equiv |\psi_t\rangle\langle\psi_t|$, which was stated in eq. (B.5), to coincide at the final time with our observable $\mathcal{O}(T) = O_T$, and it is propagated backwards with eq. (B.5)[1] With those propagated equations and the dipole matrix, it is possible to calculate the term in eq. (B.13), at every time of the system evolution. At this point, the only undetermined term in the integral equation (B.14) is the control field $E(t)$. It can be

[1] O_T corresponds to an initial condition in the Heisenberg picture.

found by the following self-consistent solution for eq. (B.14)

$$E^{(n+1)}(t) = E^{(n)}(t) + \eta s(t) f_\mu^{(n+1)}(t), \tag{B.15}$$

with η, a positive constant (to be calibrated depending on the performance of the code) and $s(t)$, a positive function (usually an enveloping function of the field like a Gaussian function)[2]. The eq. (B.15) starts at $n = 0$ with our initial reference field $E^{(0)}(t)$. The differential equations (B.1), (B.5) and (B.13) can also be rewritten as iterative expressions

$$i\hbar \frac{\partial \mathcal{O}^{(n)}(t)}{\partial t} = \left[\mathcal{O}^{(n)}(t),\, H_0 - \mu E^{(n)}(t)\right],\ \mathcal{O}(T) \to \mathcal{O}(0),$$

for the observable, and

$$i\hbar \frac{\partial |\psi_f^{(n+1)}(t)\rangle}{\partial t} = \left(H_0 - \mu E^{(n+1)}(t)\right) |\psi_f^{(n+1)}(t)\rangle,$$

for the state, where $E^{(n+1)}(t)$ is the (n+1)th iteration field, that can be found with eq. (B.15). These equations are propagated at every iteration with the respective reference field, in order to calculate the correction of the following (n+1)st iteration field f_μ

$$f_\mu^{(n+1)}(t) = -\frac{2}{\hbar} \mathrm{Im}\left\{\langle \psi^{(n+1)}(t)|\mathcal{O}^{(n)}(t)\mu|\psi^{(n+1)}(t)\rangle\right\}.$$

The stop criteria for the iterations is set by a required precision in the expected value of our observable $\langle \mathcal{O}(T)\rangle = \langle O_T\rangle$ the final state evolved in the (n)th iteration $|\psi_f^{(n)}(T)\rangle$, compared to the target state, $\left\langle \psi_f^{(n)}(T)|\psi_t\rangle\langle\psi_t^{(n)}|\psi_f(T)\right\rangle = |\langle\psi^{(n)}(T)|\psi_t\rangle|^2$. This quantity coincides with the definition of fidelity

$$\mathcal{F}^{(n)} = |\langle \psi_f^{(n)}(T)|\psi_t\rangle|^2.$$

The closer this quantity is to 1, the more similar is the final state with the target state. The TBQCP is monotonic, then with every iteration, the final state gets closer to the target state. Therefore, a tolerance value $\delta \lesssim 1$ is set for the fidelity in the (n)th iteration and compared with a fidelity some iterations before (e.g. 20 iterations in our codes). Then, if it is satisfied that $\mathcal{F}^{(n)} - \mathcal{F}^{(n-20)} > \delta$, the code stops and we declare the (n)th iteration field $E^{(n)}(t)$ as our control field $E(t)$.

B.1.2 Fast-kick-off numerical acelerator

The number of iterations necessary to satisfy the stop criteria of the TBQCP method is undetermined and can vary notably (even for the same system) from one target state to the other, taking hundreds of iterations or thousands of iterations in some cases. This

[2] As long as these two factors are positive, and since $\mathcal{O}(t)$ is a positive semi-definite invariant, then the integral in eq. (B.14) is guaranteed to be always positive as demonstrated in [126].

is expected since depending of the target state, the choosing of a poor (or a good) initial reference field $E^{(0)}(t)$ (a chose that is arbitrary in most of the cases), sets different conditions for the optimizer, requiring more or less iterations to be optimized. Also, the complexity of the task can make the whole optimization high demanding in time (requiring even more than a week of computation). For these cases, it is interesting to reduce the required number of iterations necessary to satisfy the stop criteria. This can be done by implementing a numerical accelerator that modules the correction term expressed in eq. (B.13). A possible way to do this was published in Ref. [111], where they proposed a small modification of the anzats as

$$E^{(n+1)}(t) = E^{(n)}(t) + \eta s(t)\varepsilon_{\alpha}^{(n+1)}(t), \tag{B.16}$$

where the correction term of eq. (B.13), $f_{\mu}^{(n+1)}(t)$ was replaced by

$$\varepsilon_{\alpha}^{(n+1)}(t) = -\frac{2}{\hbar}\mathrm{Im}\left\{ \frac{\langle\psi_f^{(n+1)}(t)|\psi_b^{(n)}(t)\rangle}{\left|\langle\psi_f^{(n+1)}(t)|\psi_b^{(n)}(t)\rangle\right|^{\alpha}} \langle\psi_b^{(n)}(t)|\mu|\psi_f^{(n+1)}(t)\rangle \right\},$$

with $0 \leq \alpha \leq 1$.

Appendix C

TBQCP algorithm

In this appendix we show a brief guide of the algorithm of the TBQCP method applied to closed systems under an unitary evolution. The evolution of states are implemented via exponential propagator (but any other variation of this propagator can fit as well). Comments of the pseudocode are marked by the # symbol.

C.1 Algorithm of the TBQCP method

1) Set the global variables and operators corresponding to:
T: the duration of the pulse.
n: number of time steps to discretize the pulse duration.
Δt: the time step, given by $\Delta t = T/n$.
$E^{(0)}(t)$: Define the initial reference field.
η: positive constant that modulates the correction.
$s(t)$: positive enveloping function as specified in chapter 3.
$|\psi_0\rangle$, $|\psi_t\rangle$: Define the initial conditions for the initial and final states.
F_{tol}: Tolerance value for the fidelity, a number $\lesssim 1$.
$H = H_0 - \mu E^{(0)}(t)$: The complete Hamiltonian of the system.
Fid: Fidelity of a certain iteration.

2)Implementaion of the optimization method.

#Set an initial value for Fid

$Fid = 0$

#loop for the optimizer

loop While $Fid < F_{tol}${

#Set the the initial conditions for the initial and final states for the backward and forward evolutions

$|\psi_b(T)\rangle = |\psi_t\rangle$ and $|\psi_f(0)\rangle = |\psi_0\rangle$.

#loop for the backward propagation

loop For $k = 0$ to $k = n$\{

#instant in this loop

$t_k = T - k * \Delta t$

#backward exponential propagator

$|\psi_b(t_k - \Delta t)\rangle = \exp\left[iH\Delta t/\hbar\right]|\psi_b(t_k)\rangle$

}

#end of the backward propagation loop

#loop for the forward propagation + field correction

loop For $j = 0$ to $j = n$\{

#instant in this loop

$t_j = j * \Delta t$

#forward exponential propagator

$|\psi_f(t_j + \Delta t)\rangle = \exp\left[-iH\Delta t/\hbar\right]|\psi_f(t_j)\rangle$

#Calculate the correction term $f_\mu(t)$ from eq. (B.13)

$f_\mu(t_j) = -\frac{2}{\hbar}\mathrm{Im}\left\{\langle\psi_f(t_j)|\psi_b(t_{j-1})\rangle\langle\psi_b(t_{j-1})|\mu|\psi_f(t_j)\rangle\right\}$

#correction of the field for the next step[1]

$E^{(0)}(t_{j+1}) = E^{(0)}(t_{j+1}) + \eta s(t) f_\mu(t_j)$

}

#end of the forward propagation loop

#Calculate the fidelity of the target state and the final state after the forward propagation

$Fid = |\langle\psi_f(T)|\psi_t\rangle|^2$

#When the following condition is satisfied, the code stops

$Fid \geq F_{tol}$

}

#end of the optimizater loop

[1] This formula overwrites the reference field, to be used in the following time step of the the forward evolution loop. At the end of the optimization it will end up with the profile of the optimal control field.